THE MINISTRY OF SCIENCE AND HIGHER EDUCATION OF THE RUSSIAN FEDERATION

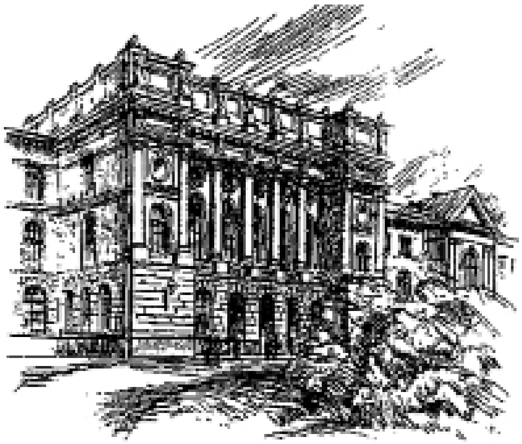

ISSN 2687-0517

Computing, Telecommunications and Control

Vol. 16, No. 3
2023

Peter the Great St. Petersburg
Polytechnic University
2023

COMPUTING, TELECOMMUNICATIONS AND CONTROL

The journal is included in the List of Leading PeerReviewed Scientific Journals and other editions to publish major findings of PhD theses for the research degrees of Doctor of Sciences and Candidate of Sciences.

Open access journal is to publish articles of a high scientific level covering advanced experience, research results, theoretical and practical problems of informatics, electronics, telecommunications, and control.

The journal is indexed by Ulrich's Periodicals Directory, Google Scholar, EBSCO, ProQuest, Index Copernicus, VINITI RAS Abstract Journal (Referativnyi Zhurnal), VINITI RAS Scientific and Technical Literature Collection, Russian Science Citation Index (RSCI) database Scientific Electronic Library and Math-Net.ru databases.

The journal is registered with the Federal Service for Supervision in the Sphere of Telecom, Information Technologies and Mass Communications (ROSKOMNADZOR). Certificate ЭЛ No. ФС77-77378 issued 25.12.2019.

Editorial office

Dr. Sc., Professor A.S. Korotkov – Editor-in-Chief;

E.A. Kalinina – literary editor, proofreader; G.A. Pyshkina – editorial manager; A.A. Kononova – computer layout; D.Yu. Alekseeva – English translation.

Address: 195251 Polytekhnicheskaya Str. 29, St. Petersburg, Russia.

+7 (812) 552-6216, e-mail: infocom@spbstu.ru

Release date: 11.10.2023

МИНИСТЕРСТВО НАУКИ И ВЫСШЕГО ОБРАЗОВАНИЯ РОССИЙСКОЙ ФЕДЕРАЦИИ

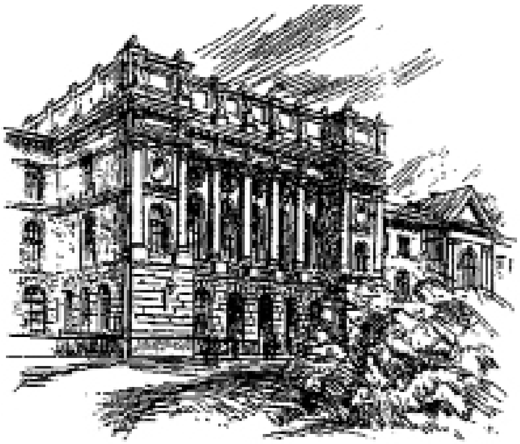

ISSN 2687-0517

Информатика, телекоммуникации и управление

Том 16, № 3
2023

Санкт-Петербургский политехнический
университет Петра Великого
2023

ИНФОРМАТИКА, ТЕЛЕКОММУНИКАЦИИ И УПРАВЛЕНИЕ

Журнал с 2002 года входит в Перечень ведущих рецензируемых научных журналов и изданий, в которых должны быть опубликованы основные результаты диссертаций на соискание ученой степени доктора и кандидата наук.

Сетевое издание открытого доступа публикует статьи высокого научного уровня, освещающие передовой опыт, результаты НИР, теоретические и практические проблемы информатики, электроники, телекоммуникаций, управления.

Сведения о публикациях представлены в Реферативном журнале ВИНИТИ РАН, в международной справочной системе «Ulrich`s Periodical Directory», в Российской государственной библиотеке. В базах данных: Российский индекс научного цитирования (РИНЦ), Google Scholar, EBSCO, Math-Net.Ru, ProQuest, Index Copernicus.

Журнал зарегистрирован Федеральной службой по надзору в сфере информационных технологий и массовых коммуникаций (Роскомнадзор). Свидетельство о регистрации ЭЛ № ФС77-77378 от 25.12.2019.

Учредитель и издатель: Санкт-Петербургский политехнический университет Петра Великого, Санкт-Петербург, Российская Федерация.

Редакция журнала

д-р техн. наук, профессор А.С. Коротков – главный редактор;

Е.А. Калинина – литературный редактор, корректор; Г.А. Пышкина – ответственный секретарь, выпускающий редактор;

А.А. Кононова – компьютерная вёрстка; Д.Ю. Алексеева – перевод на английский язык.

Адрес редакции: Россия, 195251, Санкт-Петербург, ул. Политехническая, д. 29.

Тел. редакции +7(812) 552-62-16, e-mail: infocom@spbstu.ru

Дата выхода: 11.10.2023

Contents

Содержание

Устройства и системы передачи, приема и обработки сигналов

Информационные, управляющие и измерительные системы

Интеллектуальные системы и технологии

Computing, Telecommunication and Control, 2023, Vol. 16, No. 3, Pp. 7–17.
Информатика, телекоммуникации и управление. 2023. Том 16, № 3. С. 7–17.

Circuits and Systems for Receiving, Transmitting and Signal Processing

Устройства и системы передачи, приема и обработки сигналов

Research article
DOI: https://doi.org/10.18721/JCSTCS.16301
UDC 621.372.543

FEATURES OF CENTIMETER-BAND FILTER-BANK DESIGN BASED ON GaAs pHEMT-TECHNOLOGY

D.V. Klimenko[1], *A.B. Nikitin*[2] ✉, *A.A. Stroganov*[2], *I.A. Tsikin*[2]

[1] Special Technological Center Ltd, St. Petersburg, Russian Federation;
[2] Peter the Great St. Petersburg Polytechnic University, St. Petersburg, Russian Federation

✉ nikitin@mail.spbstu.ru

Abstract. This article presents the results of the filter-bank design in the centimeter range. The filters are made in the form of microwave monolithic integrated circuits based on domestic GaAs pHEMT technology. The filter-bank includes bandpass filters operating in four subbands of the total frequency band 5.8 ... 18.2 GHz. The developed filters have VSWR of no more than 1.5 in the passband. Stopband suppression at 30% offset or more from the passband center frequency is more than 45 dB. When constructing filters of different subranges, different implementation options were used: lumped filters and microstrip filters based on interdigital and hairpin structures. Using the example of the microstrip bandpass filters design, the article discusses the features of modeling microwave monolithic integrated circuits in the AWR Design Environment.

Keywords: microwave, bandpass filter, GaAs pHEMT, interdigital, hairpin, electromagnetic simulation

Citation: Klimenko D.V., Nikitin A.B., Stroganov A.A., Tsikin I.A. Features of centimeter-band filter-bank design based on GaAs pHEMT-technology. Computing, Telecommunications and Control, 2023, Vol. 16, No. 3, Pp. 7–17. DOI: 10.18721/JCSTCS.16301

Научная статья
DOI: https://doi.org/10.18721/JCSTCS.16301
УДК 621.372.543

ОСОБЕННОСТИ РАЗРАБОТКИ БАНКА ФИЛЬТРОВ САНТИМЕТРОВОГО ДИАПАЗОНА НА ОСНОВЕ GaAs pHEMT-ТЕХНОЛОГИИ

Д.В. Клименко[1], *А.Б. Никитин*[2] ✉ ,
А.А. Строганов[2], *И.А. Цикин*[2]

[1] ООО «Специальный технологический центр»,
Санкт-Петербург, Российская Федерация;

[2] Санкт-Петербургский политехнический университет Петра Великого,
Санкт-Петербург, Российская Федерация

✉ nikitin@mail.spbstu.ru

Аннотация. В данной статье представлены результаты разработки банка фильтров сантиметрового диапазона, выполненных в виде СВЧ монолитных интегральных схем на основе отечественной GaAs pHEMT-технологии. Банк включает в себя полосовые фильтры, работающие в четырех поддиапазонах общей полосы частот 5,8 ... 18,2 ГГц. Разработанные фильтры банка имеют в полосе пропускания КСВН не более 1,5, при подавлении в полосе заграждения не хуже 45 дБ на отстройках от центральной частоты, превосходящих ±30%. Вносимые потери в полосе пропускания не превосходят 6 дБ в низкочастотной и 3 дБ в высокочастотной части исследуемого диапазона. При построении фильтров разных поддиапазонов были использованы различные варианты реализации: фильтры на сосредоточенных элементах и микрополосковые фильтры на встречно-штыревых и шпилечных структурах. На примере разработки микрополосковых полосовых фильтров в статье рассмотрены особенности моделирования СВЧ монолитных интегральных схем в среде AWR Design Environment.

Ключевые слова: СВЧ, полосовой фильтр, GaAs pHEMT, встречно-стержневой, шпилечный, электромагнитное моделирование

Для цитирования: Klimenko D.V., Nikitin A.B., Stroganov A.A., Tsikin I.A. Features of centimeter-band filter-bank design based on GaAs pHEMT-technology // Computing, Telecommunications and Control. 2023. Т. 16, № 3. С. 7–17. DOI: 10.18721/JCSTCS.16301

Introduction

One of the main elements of a preselector in modern radio-receiving microwave devices is a filter-bank, which includes a set of bandpass filters (BPF). The characteristics of such partial BPFs – the main components of the filter-bank – determine several important parameters of the entire radio-receiving device. When developing bandpass microwave filters in the form of monolithic microwave integrated circuits (MMIC), they can be designed as lumped or distributed element circuits and implemented in various transmission line structures [1–3].

Bandpass filters based on microstrip structures are often used in the microwaves due to their compact size and high yield. Several examples of simplified microstrip BPF's circuits that are widely used in practice are shown in Fig. 1: *a*) interdigital, *b*) hairpin, *c*) open-loop [1, 4].

Despite the large number of works devoted to the microwave filters studies (e.g. [1–9]), the choice of the basic structure and the development of the final circuit in each case is a separate, rather labor-intensive task. An example of such a task is the development of a microwave bandpass filter-bank that covers a large frequency band (an octave or more). In this case, it is necessary, based on a single MMIC technology, to

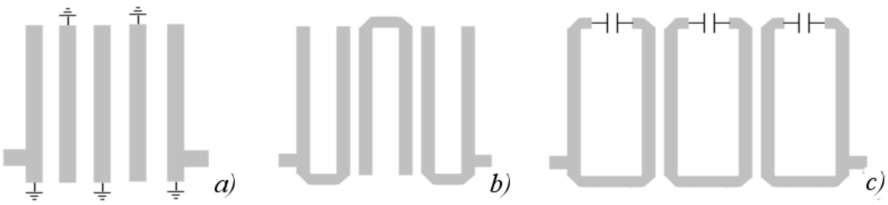

Fig. 1. Simplified schemes of microwave microstrip bandpass filters

build several circuits that provide the required characteristics in several frequency sub-ranges of preselectors of broadband radio receiving devices [10, 11].

Introduction of monolithic microwave integrated circuits in the creation of filters allows drastic reduction of the mass, size, labor intensity of manufacturing, while increasing reliability and improving the repeatability of characteristics. In conditions of mass serial production, it also reduces costs per unit of production [2]. At the same time, it is important to note that due to permanent restrictions on the supply of electronic devices and dual-use systems to Russia it is becoming increasingly difficult to obtain the required products from abroad [12]. In this regard, the expansion of the microelectronic microwave devices nomenclature, produced on the basis of domestic technology and optimization of the process of their modeling are of particular relevance [12, 13].

This paper describes the design of the bandpass filter-bank on the example of studies of various MMIC BPF's circuits covering the frequency range, including most of the C-, X-, and Ku-bands in four sub-ranges: No. 1 – 5.8 ... 8.2 GHz, No. 2 – 7.8 ... 11.2 GHz, No. 3 –10.8 ... 15.2 GHz, No. 4 – 14.8 ... 18.2 GHz.

The following frequency responses were used as required performance for the developing bandpass filters: insertion loss in sub-range No. 1 – 6 dB, No. 2 – 5 dB, No. 3 – 5 dB, No. 4 – 4 dB, VSWR in passband is not more than 1.6, stopband suppression is no less than 45 dB at 30% offset and more from the passband center frequency.

The filters under study are designed based on the domestic GaAs pHEMT technology using complex design tools for solid-state microwave devices for the 0.25 μm technological process (PDK_pHEMT025D) [14–16].

LC-bandpass filters on lumped elements

At the comparative study of various bandpass filters operating in the low-frequency part of the investigated frequency range (sub-ranges No. 1: 5.8 ... 8.2 GHz and No. 2: 7.8 ... 11.2 GHz), it was found that it is reasonable to use LC-filter circuits on lumped elements as basic schemes. The simulation showed that the use of microstrip structures (Fig. 1) as basic circuits of bandpass filters at these frequency leads to excessively large dimensions of the MMIC chip (more than 5000×5000 μm)

The conducted studies of the idealized filter prototype have shown that to obtain the required characteristics it is necessary to choose filters with frequency responses having transmission zeros in the stopband. In addition, the simulation of an idealized filter prototype showed that the filter order should be quite large. Therefore, in this paper a quasi-elliptic filter on lumped elements of the 9th order was chosen as a basis for the BPF construction of the 1st and 2nd sub-ranges. An equivalent circuit of such an idealized bandpass LC-filter with transmission zeros near the passband edges is shown in Fig. 2, *a* [1].

When selecting the scheme and order of the idealized prototype filter, the initial parameters should be used with a certain margin both in terms of insertion loss in the passband (a few dB) and rejection in the stopband (up to 50 dB).

Besides, the results of the research have shown that it is expedient to increase values of the central operating frequency and a bandwidth (in comparison with initial data). Further design of the filter generally leads to narrowing of the initial bandwidth and some shift to the low frequency area. For example,

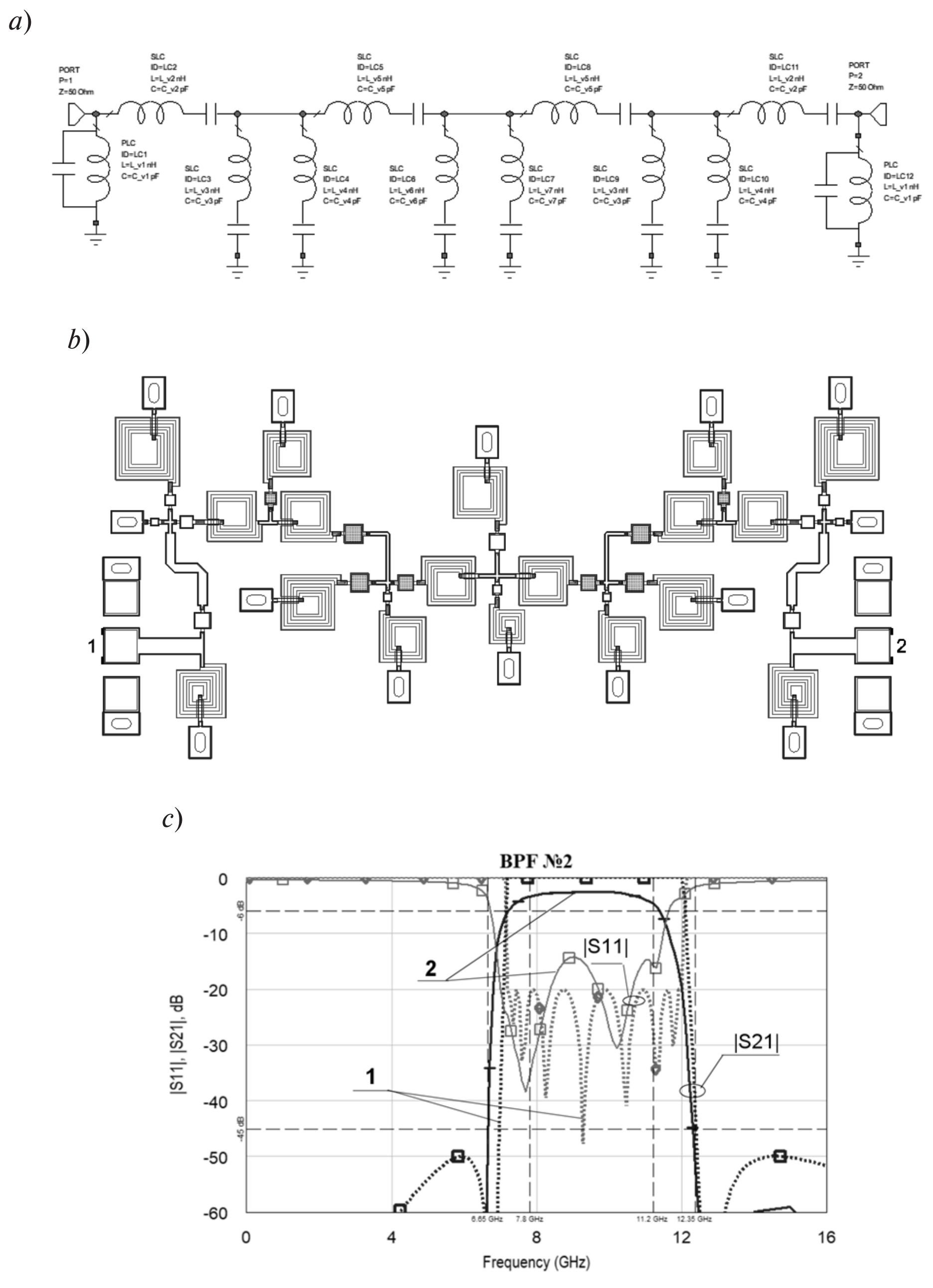

Fig. 2. Schematic of idealized BPF No. 2 (*a*), MMIC layout (*b*) and frequency responses (*c*): 1 – idealized BPF, 2 – MMIC

when designing 1st sub-range BPF (BPF No. 1) at the given values of the center frequency f_0 = 7 GHz and 6.8 ... 8.2 GHz bandwidth it is reasonable to set a significantly larger bandwidth of the initial prototype to 5.45 ... 8.65 GHz with the center frequency f_0 = 7.1 GHz.

When designing the BPF of the 2nd sub-range (BPF No. 2) these corrections, as simulation has shown, make the following values: at given values of the center frequency f_0 = 9.5 GHz and 7.8 ... 11.2 GHz bandwidth it is necessary to set the bandwidth of the initial prototype to 7.2 ... 12 GHz with f_0 = 9.6 GHz.

As an example, Fig. 2 shows: the circuit of the initial idealized BPF No. 2 (Fig. 2, *a*), MMIC topology designed on its basis (Fig. 2, *b*) and BPF frequency responses |S11|, |S21| – insertion loss and input return loss. In the Fig. 2, *c*, the dashed lines show the responses of the idealized circuit (curves 1), and the solid

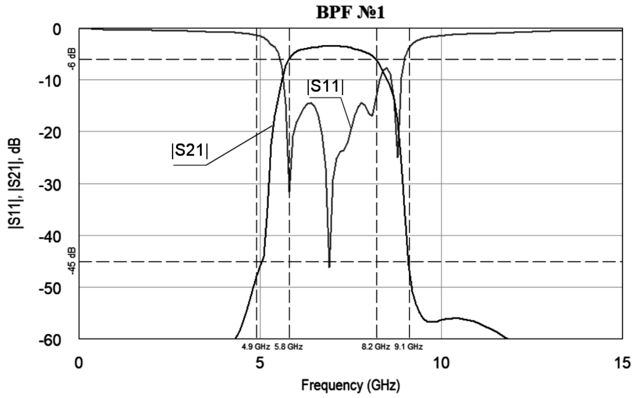

Fig. 3. S-parameters of BPF No. 1

lines show the simulation result of the final MMIC (curves 2). It should be noted that MMIC design included two stages: basic circuit design using process design kit (PDK) and MMIC topology design using electromagnetic (EM) simulation.

The frequency responses of the MMIC BPF No. 1 is shown in Fig. 3.

The designed BPFs No. 1 and No. 2 have the following characteristics: insertion loss is no more than 6 dB for sub-range No. 1 and 4.6 dB for sub-range No. 2 (3.5 dB and 2.5 dB at center frequency f0 for No. 1 and No. 2, respectively), return loss is not worse than 14.5 dB (input and output VSWR for both filters no more than 1.5). Stopband suppression at 30% offset or more from the passband center frequency is not worse than 45.5 dB for sub-range No. 1 and 49 dB for sub-range No. 2. MMIC chip of BPF No. 1, 2 have dimensions less than 2000×2600 μm.

Bandpass filters on microstrip structures

According to the results of the studies about filters operating on higher frequency ranges (BPF No. 3 – 10.8 ... 15.2 GHz and BPF No. 4 – 14.8 ... 18.2 GHz), filters on microstrip structures are preferred when selecting initial schemes (Fig. 1). It is easier to provide the required level of insertion loss using microstrip structures in comparison to LC-filters on lumped elements. Comparative modeling of microstrip bandpass filters showed that the best choice in this frequency range would be the schemes of the hairpin (Fig. 1, *a*) and interdigital (Fig. 1, *b*) filters. In this case, four microstrip structures were considered. Along with the two mentioned above, open-loop filters (Fig. 1, *c*) and filters on stepped microstrip resonators were also studied. Filters based on open-loop resonators and stepped microstrip resonators showed generally worse performance. In particular, the dimensions of open-loop microstrip structures are significantly larger in comparison with hairpin and interdigital structures (in this case up to 9000 μm or more).

To determine filter orders needed to achieve the required parameters, studies of corresponding idealized prototype filter circuits were conducted. Studies showed, that when designing interdigital and hairpin filters, it is advisable to use prototypes of the 15th and 7th orders, respectively.

The standard topology of microstrip elements in the PDK_pHEMT025D library consists of two metallization layers. The first layer with a thickness of 1 μm is formed by sputtering, while the second layer is formed by chemical deposition, with a thickness about 5 μm. As a result of deposition, the microstrip does not have a strictly rectangular profile, and its thickness can vary in length. To increase the yields of the MMIC, it was decided to use only the first layer of metallization during design. Fig. 4 shows the resulting designed MMIC topologies: the interdigital filter – BPF No. 3 (Fig. 4, *a*) and the hairpin filter – BPF No. 4 (Fig. 4, *b*).

The simulation showed that the filter circuits require input and output matching circuits to achieve the required frequency responses. Some of the matching circuits include both microstrip line segments and lumped LC-elements, for example, a MIM-capacitor for the hairpin filter circuit (Fig. 4, *b*).

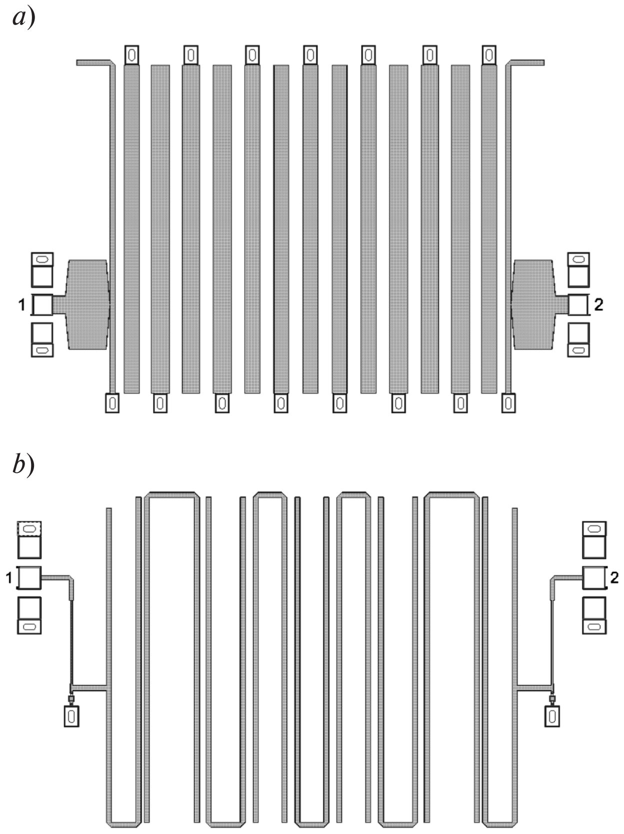

Fig. 4. MMIC topologies of bandpass filters No. 3 (*a*) and No. 4 (*b*)

When selecting the basic circuits, simulation of the two above mentioned filters was carried out in both sub-ranges No. 3 and No. 4. In the considered sub-ranges interdigitated and hairpin filters have similar performance and satisfy the required characteristics.

Detailed comparison of these two filters performances (insertion loss, return loss, selectivity and chip size) allows us to make a choice in sub-range No. 3 in favor of an interdigital BPF (Fig. 4, *a*), and in sub-range No. 4 in favor of a hairpin BPF (Fig. 4 *b*).

Fig. 5 shows the characteristics of the interdigital (sub-range No. 3) and hairpin filter (sub-range No. 4) in the form of frequency responses |S11| and |S21|. In Fig. 5 the dashed lines show the responses of the BPF No. 3 (curves 3), and the solid lines – BPF No. 4 (curves 4).

The designed MMIC of the BPF No. 3 has the following frequency responses: the minimum value |S21| = –4.2 dB at the frequency f = 15.2 GHz in the passband. Stopband suppression at 30% offset or more from the passband center frequency is more than 49 dB. Return loss is not worse 14 dB (input and output VSWR is not more than 1.5).

The designed MMIC of the BPF No. 4 has following performance: maximum value of insertion loss in the passband is 3.1 dB at the frequency f = 18.2 GHz and 2.4 dB at the center frequency f_0 = 16.5 GHz of the passband. Stopband suppression at 30% offset or more from the passband center frequency is more than 48.5 dB. Return loss is not worse than 25 dB in passband (input and output VSWR is not more than 1.1). MMIC sizes of both BPF No. 3 and No. 4 do not exceed 2100×3100 μm.

The MMIC filter simulation features

A distinctive feature of microwave circuits topology development, as noted above, is the need for electromagnetic (EM) modeling at the final stage of design. The results of EM simulation often differ significantly from the results of circuit simulation based on library elements [17–21]. This difference turns out

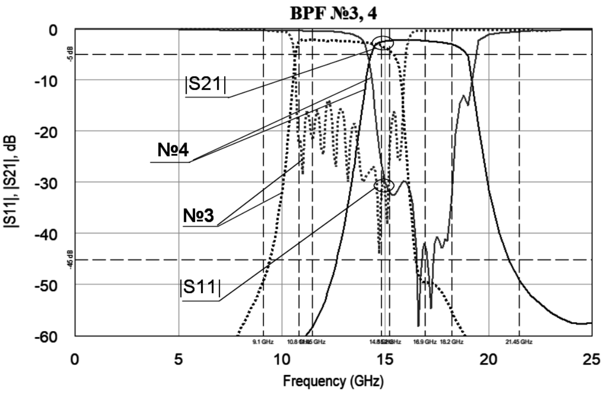

Fig. 5. S-parameters of BPF No. 3 and No. 4.

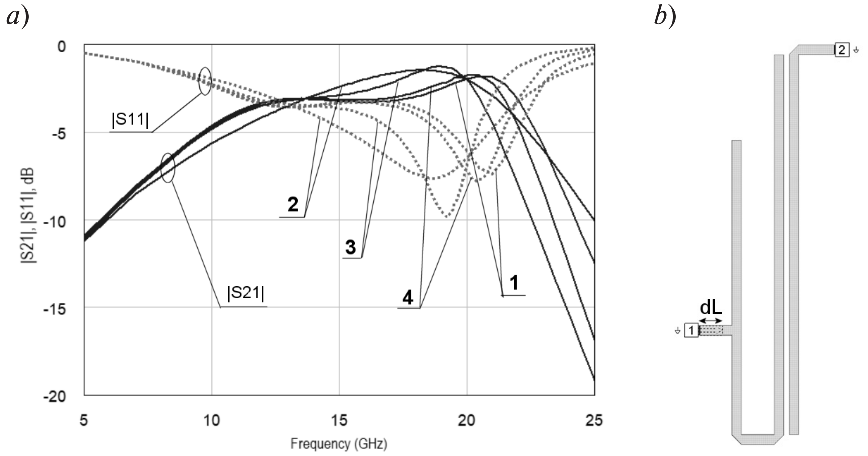

Fig. 6. Frequency responses of the test circuit (*a*) and a part of the test structure topology (*b*)

to be more essential on the higher frequency range as well as with more complex chip design. At the same time, to achieve the required parameters and define the final chip topology, it is often necessary to conduct many EM simulation cycles. Therefore, methods to optimize the chip design process were considered during filter development. A study of the effect of different MMIC design ways on the resulting characteristics was carried out. For this purpose, a fragment of the hairpin BPF circuit was considered as a test sample (Fig. 4, *b*). This test circuit was divided into two subcircuits and on their basis the following variants of forming topology and simulating characteristics were implemented:

1. EM simulation of a complete test structure. This simulation variant was used as a reference.
2. Circuit simulation of the test structure based on library elements.
3. EM simulation of two subcircuits of the test structure separately. Simulation of a two-stage circuit, where EM models act as composite stages.

Fig. 6, *a* shows the frequency response simulation of the considered test circuit obtained by three different methods. Numbers 1, 2 and 3 in the graph indicate three different simulation ways described above.

As follows from the graphs in Fig. 6, *a*, the results of circuit simulation (Fig. 6, *a*, curves 2) and EM simulation (Fig. 6, *a*, curves 1) are significantly different. EM simulation of the divided the test structure (Fig. 6, curves 3), allows to slightly approximate the responses to the reference ones. However, the discrepancy is still quite significant. This may be a consequence of the unaccounted electromagnetic interaction between the individual stages of the whole circuit. This situation occurs in the modeling for option 3.

The studies have shown that the use of de-embedding procedure with reference plane shifting can help to reduce the differences between the full EM model of the whole circuit (Fig. 6, *a*, curves 1) and the composite one (Fig. 6, *a*, curves 3) consisting of EM models of subcircuits [18, 21]. Fig. 6 *b* shows the topology of one of the test structures subcircuits, indicating the value dL of the input port reference plane shift. The result of modeling a two-stage circuit, where EM models of individual subcircuits with a shift value of the reference plane dL = 30 μm act as composite stages, is marked with number 4 in Fig. 6, *a*.

As shown in Fig. 6, the use of reference plane shift makes it possible to significantly reduce the difference between the frequency responses of a complete EM model of a single circuit (Fig. 6, a, curves 1) and the frequency responses of a two-stage circuit, where EM models act as composite stages (Fig. 6, *a*, curves 4). Design and simulation of such composite circuit are much faster. The results of modeling have shown that it is reasonable to choose the value of such shift in the range of 20 ... 50 μm for the considered structures.

Comparison with State-of-the-Art Filters

The characteristics of the filters studied in this work and their foreign analogues, based on monolithic GaAs MMICs, are provided in Table 1.

Table 1

Characteristics of filters based on monolithic GaAs MMICs

Ref.	f_0, GHz	$f_1 - f_2$, GHz (FBW %)	$IL(f_0)$, dB	Ripple, dB	$RLmin$, dB	Reject., dB	Size, mm²
BWBF-8/12 [22]	10	8-12 (40%)	1.7	2	15	>25	1.42
BWBF-12/16-7C3 [22]	14	12-16 (28%)	2.5	1	12	<20	1.28
PDBF-15R7/17R7-D2 [22]	16.7	15.7-17.7 (12%)	2	1*	11	40	5.12
XBF-163-D+ [23]	16	15.5-16.5 (6.3%)	4	N/A	17	>50	3.44
MFBP-0002CH [24]	6.65	5.9-7.4 (22%)	1.5	1*	18	45	5.76
MFBA-0003CH [24]	12	10.1-14.1 (33%)	2.1	1*	15	44	9.6
MFBA-00001CH [24]	16	14.1-17.9 (22%)	2.4	1.2*	17	45	9.6
This work BPF#1	7	5.8-8.2 (34%)	3.5	2.5	14.5	46	4.04
This work BPF#2	9.5	7.8-11.2 (36%)	2.5	2.2	14.2	48	3.46
This work BPF#3	13	10.8-15.2 (34%)	2.3	1.9	14	49	6.41
This work BPF#4	16.5	14.8-18.2 (21%)	2.4	0.8	25	48.5	5.36

* – approximate

The table shows the following parameters: f_0 – central frequency of the passband; $f_1 - f_2$ (FBW) – minimum and maximum frequencies of the passband (relative bandwidth); IL – insertion loss at the central frequency; Ripple – ripple in the passband; $RLmin$ – minimal return loss in the passband; Reject. – stopband suppression (at offset from the center frequency $f_0 \pm 0.3f_0$ and more), Size – MMIC size. A comparison of the given data shows that filters BPF No. 1–3 are somewhat inferior to some samples in terms of the chip size [22], as well as the ripple in the passband [22, 24]. At the same time, the developed BPFs are highly selective. According to this characteristic, the filters under study are superior to most of the presented samples. In addition, for example, BPF No. 4 turns out to be better than filters of a similar range in other parameters [22, 24]. As shown, using the domestic GaAs pHEMT technology, the overall performance of the designed BPFs is very competitive.

Conclusion

The paper presented a comparative study of various implementations of bandpass filters on monolithic integrated circuits, covering the most part of C-, X- and Ku-bands. The results show that in the lower part of the considered frequency range it is expedient to build filters on the basis of lumped elements, while in the high-frequency part bandpass filters on microstrip structures have the advantage over LC-filters, among which hairpin and interdigital filters have demonstrated the best characteristics.

To reduce the number of required EM simulation cycles and decrease the total design time of a MMIC, it is advisable to divide the designed circuit into several subcircuits with step-by-step EM simulation of individual stages.

As a result of this research, a filter-bank was designed, including four MMIC bandpass filters overlapping the total operating bandwidth of 5.8 ... 18.2 GHz. The partial BPFs of filter-bank are designed on the basis of domestic GaAs pHEMT-technology using comprehensive tools for designing solid-state microwave devices (PDK_pHEMT025D) and have a bandwidth of 20–35%. All four designed filters have VSWR of no more than 1.5 in the passband. Stopband suppression at 30% offset or more from the passband center frequency is more than 45 dB.

REFERENCES

1. **Hong J.-S.** Microstrip Filters for RF/Microwave Applications. John Wiley & Sons, Inc. 2011. 635 p.

2. **Jorgesen D., Marki C.** MMIC Filters' Time Has Come. Microwave Journal, 2022, Vol. 65, no. 10, Pp. 48–60.

3. **Psychogiou D., Gomez-Garcia R., Peroulis D.** Recent Advances in Reconfigurable Filter Design. Invited paper. 2016 IEEE 17th Annual Wireless and Microwave Technology Conference (WAMICON). Pp. 1–6.

4. **Athukorala L., Budimir D.** Design of Open-Loop Dual-Mode Microstrip Filters. Progress in Electromagnetics Research Letters, 2010, Vol. 19. Pp.179–185.

5. **Al-Yasir I.A., Parchin N.O., Abd-Alhameed R.A., Abdulkhaleq A.M., Noras J.M.** Recent Progress in the Design of 4G/5G Reconfigurable Filters. Electronics, 2019, Vol. 8 (1), no. 114, Pp. 1–17.

6. **Ashley A., Psychogiou D.** X-Band Quasi-Elliptic Non-Reciprocal Bandpass Filters (NBPFs). IEEE Transactions on Microwave Theory and Techniques, 2021, Vol. 69. no. 7, Pp. 3255–3263.

7. **Simpson D., Psychogiou D.** X-Band Quasi-Reflectionless MMIC Bandpass Filters with Minimum Number of Components. IEEE Transactions on Electron Devices, 2021, Vol. 68, no. 9, Pp. 4329–4334.

8. **Shen G., Che W., Feng W., Shi Y., Shen Y.** Low Insertion-Loss MMIC Bandpass Filter Using Lumped-Distributed Parameters for 5G Millimeter-Wave Application. IEEE Transactions on Components, Packaging and Manufacturing Technology, 2021, Vol. 11, no. 1, Pp. 98–108.

9. **Shen G., Che W., Feng W., Shi Y., Shen Y., Xu F.** A Miniaturized Ka-Band Bandpass Filter Using Folded Hybrid Resonators Based on Monolithic Microwave Integrated Circuit Technology. IEEE Transactions on Circuits and Systems II: Express Briefs, 2021,Vol. 68, no. 6, Pp. 1778–1782.

10. **Burakov A.I., Drychik P.I., Uspenskaya A.V.** Preselektory diapazona 30–1000 MGts dlya SDR i COGNITIVE RADIO [A 30–1000 MHz Band Preselectors for SDR and Cognitive Radio]. Teoriya i tekhnika radiosvyazi. 2019. No. 2. Pp. 37–46. (rus)

11. **Kaplun D.I., Klionskiy D.M., Oleynik A.L., Voznesenskiy A.S., Zhukova N.A., Gulvanskiy V.V.** Primeneniye polifaznykh bankov filtrov v zadachakh monitoringa shirokogo chastotnogo diapazona [Application of polyphase filter-banks to tasks of wideband monitoring] // Izvestiya vysshikh uchebnykh zavedeniy Rossii. Radioelektronika. 2013. No. 3. Pp. 38–43. (rus)

12. **Kochemasov V., Stroganova Ye.** Elektronnyye komponenty inostrannogo proizvodstva. Ogranicheniye eksporta v Rossiyu [Foreign-Made Electronic Components. Russian Exports Restriction]. Elektronika NTB. 2013. No. 1. Pp. 125–129. (rus)

13. **Sukhanov D.** Modernizatsiya proizvodstva SVCh MIS [Modernizing Microwave MIC Production]. SVCh elektronika. 2019. No. 4, Pp. 32–35. (rus)

14. **Krasovitsky D.M., Dudin A.L., Katsavets N.I., Kokin S.V., Filaretov A.G., Chaly V.P., Viuginov V.N.** Challenges and prospects of A3B5 microvawe foundry. 22nd International Crimean Conference "Microwave & Telecommunication Technology", 2012, Pp. 615–616.

15. **Filaretov A.G., Chalyy V.P., Shukov I.V., Dudin A.L., Fazylkhanov O.R., Krasovitskiy D.M.** Organizatsiya proizvodstva vysokonadezhnykh izdeliy tverdotelnoy SVCh EKB: protsedury i pervyy opyt [Setting up a Highly Reliable Solid State Microwave Components Production – Routines and First Experience]. Nanoindustriya. Spetsvypusk, 2021, Vol. 14 (107), no. 7s, Pp. 408–410. (rus)

16. **Krasovitskiy D.M., Filaretov A.G., Chalyy V.P.** Fiziko-tekhnologicheskiye aspekty postroyeniya foundry proizvodstva SVCh EKB: opyt AO "Svetlana-Rost" [Physics and technological aspects of microwave foundry devel]. In the collection "Mockery readings", 10th Anniversary International Scientific and Practical Conference on Physics and Technology of Nanoheterostructural Microwave Electronics, 2019. Pp. 29–32. (rus)

17. **Sun W.** Accurate EM Simulation of SMT Components in RF Designs. 2017 IEEE Radio Frequency Integrated Circuits Symposium (RFIC). Pp. 140–143.

18. **Delgado I., Skidmore S., Dunleavy L.** NI AWR Design Environment/AXIEM EM Co-Simulation with Modelithics Models. 2015 IEEE 16th Annual Wireless and Microwave Technology Conference (WAMICON), April 2015. Pp. 1–4.

19. **Dunn J.M.** Where did EM simulation tools Go? IEEE Microwave Magazine. 2014, Vol. 15, no. 1, Pp. 65–69.

20. **Nikitin A.B., Khabitueva E.I.** Design for microwave wideband VCO based on electromagnetic simulation. St. Petersburg State Polytechnical University Journal. Computer Science. Telecommunications and Control Systems, 2019, Vol. 12, No. 1, Pp. 34–43. DOI: 10.18721/JCSTCS.12104

21. **Khabitueva E.I., Nikitin A.B., Okulov D.A.** Comparison of Various EM Simulators in the Design of a Wideband Microwave VCO. Proceedings of the IEEE International Conference on Electrical Engineering and Photonics EExPolytech-2020. Pp. 26–29.

22. Saintly-Tech Communications Limited. Product Data Sheet. MMIC Filters. Available: https:// http://www.sainty-tech.com/en/Filter/194.html (Accessed: 02.08.2023).

23. Mini-Circuits. Product Data Sheet. Band Pass Filter Die. Available: https:// www.minicircuits.com/WebStore/RF-Filters.html (Accessed: 02.08.2023)

24. Marki Microwave, Inc. Product Data Sheet. Passive GaAs MMIC Bandpass Filter. Available at: https:// markimicrowave.com/products/bare-die/filters/ (accessed: 02.08.2023)

INFORMATION ABOUT AUTHORS / СВЕДЕНИЯ ОБ АВТОРАХ

Klimenko Denis V.
Клименко Денис Валерьевич
E-mail: d.klimenk0@yandex.ru

Nikitin Aleksandr B.
Никитин Александр Борисович
E-mail: nikitin@mail.spbstu.ru

Stroganov Alexander A.
Строганов Александр Александрович
E-mail: lemyr103@gmail.com

Tsikin Igor A.
Цикин Игорь Анатольевич
E-mail: tsikin@mail.spbstu.ru

Submitted: 09.08.2023; Approved: 05.10.2023; Accepted: 11.10.2023.
Поступила: 09.08.2023; Одобрена: 05.10.2023; Принята: 11.10.2023.

Research article
DOI: https://doi.org/10.18721/JCSTCS.16302
UDC 537

SOI PHOTONIC CIRCUITS FOR OPTICAL COMMUNICATION SYSTEMS

R. Mansoor ✉

Electronics and Communication Engineering,
AL Muthanna University, Samawa, Iraq

✉ riyadhdmu@mu.edu.iq

Abstract. This work considers the possibility of using ring resonators as optical modulators in communication systems. Ring resonators are the major component in all-optical integrated photonic circuits due to their small size, which contributes to increasing the integration density. Controlling the light intensity through the eclectic/optic effect is the main aim of this study. Electron/optic modulation through the use of the plasma dispersion effect is studied. The plasma dispersion effect is a mechanism by which a controlled change in the effective refractive index of Silicon on Insulator (SOI) can be achieved by changing the concentration of free carriers in the silicon waveguides. In the SOI ring resonator based optical modulator, the intensity of the light passing through the resonator is controlled by changing the refractive index of the ring waveguide material, which in turn changes the resonance conditions of the resonant modes. This change in the resonance conditions can be achieved by applying an electrical field to the modulating electrodes, which are placed in the rib waveguide. In this work, the theoretical analysis and the response of the modulator are first presented, then the performance is validated using 3D simulation software. Although the work concentrates more on the intensity modulation of On-Off keying, it also opens the door for using such compact modulators for different modulation techniques such as Orthogonal Frequency Division Multiplexing (OFDM); which means high data rate modulators using small-size devices.

Keywords: optical waveguides, optical modulator, photonic circuits, ring resonator, silicon on insulator

Citation: Mansoor R. SOI photonic circuits for optical communication systems. Computing, Telecommunications and Control, 2023, Vol. 16, No. 3, Pp. 18–28. DOI: 10.18721/JCSTCS.16302

Научная статья
DOI: https://doi.org/10.18721/JCSTCS.16302
УДК 537

ФОТОННЫЕ СХЕМЫ «КРЕМНИЙ НА ИЗОЛЯТОРЕ» ДЛЯ ОПТИЧЕСКИХ СИСТЕМ СВЯЗИ

Р. Мансур ✉

Университет Аль-Мутанна, Самава, Ирак

✉ riyadhdmu@mu.edu.iq

Аннотация. В работе рассматривается возможность использования кольцевых резонаторов в качестве оптических модуляторов в системах связи. Кольцевые резонаторы являются основным компонентом полностью оптических интегральных фотонных схем из-за их небольшого размера, который способствует увеличению плотности интеграции. Управление интенсивностью света с помощью эклектического/оптического эффекта является основной целью данного исследования. Изучена электронно-оптическая модуляция с использованием эффекта плазменной дисперсии. Эффект плазменной дисперсии – это механизм, с помощью которого контролируемое изменение эффективного показателя преломления кремния на изоляторе SOI может быть достигнуто путем изменения концентрации свободных носителей в кремниевых волноводах. В оптическом модуляторе на основе кольцевого резонатора SOI интенсивность света, проходящего через резонатор, регулируется путем изменения показателя преломления материала кольцевого волновода, что, в свою очередь, изменяет условия резонанса резонансных мод. Это изменение условий резонанса может быть достигнуто путем приложения электрического поля к модулирующим электродам, которые размещены в ребристом волноводе. В этой работе представлен теоретический анализ и сначала представлен отклик модулятора, затем производительность проверяется с помощью программного обеспечения для 3D-моделирования. Хотя работа в большей степени сосредоточена на модуляции интенсивности включения-выключения, она также открывает возможности для использования таких компактных модуляторов для различных методов модуляции, таких как мультиплексирование OFDM с ортогональным частотным разделением; это означает, что модуляторы с высокой скоростью передачи данных используют малогабаритные устройства.

Ключевые слова: оптические волноводы, оптический модулятор, фотонные схемы, кольцевой резонатор, кремний на изоляторе

Для цитирования: Mansoor R. SOI photonic circuits for optical communication systems // Computing, Telecommunications and Control. 2023. Т. 16, № 3. С. 18–28. DOI: 10.18721/JCSTCS.16302

Introduction

Silicon-on-insulator (SOI) waveguides are the “Occam’s Razor” of edge connectivity for integrated photonic circuits [1]. It is a simple solution to transporting light that minimizes size, weight, and cost [2]. Adding the possibility of using these waveguides to perform modulation functions to the propagated light will contribute more to the miniaturization of optical components and increase the integration density. SOI waveguide consists of a silicon layer of a high refractive index built on silicon dioxide of a lower refractive index to ensure the confinement of light in the high refractive index core region [3]. The mode confinement is highly dependent on the effective refractive index (n_{eff}) of the SOI. Manipulating the carrier concentration of the silicon material will lead to forming a p–n junction. Therefore, using a DC volt bias can cause a concentration change of the free electrons and holes and finally change the n_{eff} of the waveguide [4]. Hence, a controlled change in the effective refractive index via an external DC voltage can lead to a phase change in the propagated light. However, using a micro ring resonator will provide the possibility to control the resonance wavelength through the controlled change of the n_{eff}, and, hence, the ring resonator optical modulator can be designed.

The ring resonator is a basic building block in all-optical integrated circuits [5]. It consists of a straight bus waveguide coupled to a bent waveguide to form a circuit that resonates in specific wavelengths. The resonance wavelength depends mainly on the ring radius and the effective refractive index of materials. The separation between bus and ring waveguides determines the coupling efficiency and as a result, the amount of light that couples from the bus waveguide and resonates in the ring [6]. If a number of wavelengths are launched in the input port of the bus waveguide, only the wavelengths that satisfy the resonance condition will couple the ring and leave the bus waveguide. The wavelength separation between two successive wavelengths is called the free spectral range FSR which depends on the ring radius [7]. Owing to their small size, ring resonators have been used widely in all-optical integrated circuits in different applications such as add-drop multiplexers, and sensors [8, 9].

In the ring resonator-based optical modulator, the intensity of the light passing through the resonator is controlled by changing the refractive index of the waveguide material, which in turn changes the resonance conditions of the resonant modes. This change in the resonance conditions can be achieved by applying an electrical field to a modulating electrode that is placed near the waveguide. Ring resonator-based optical modulators have several advantages over other types of optical modulators, including high modulation efficiency, low power consumption, low insertion loss, and compact size [4]. In recent years, there has been significant research and development in ring resonator-based optical modulators, particularly in the areas of silicon photonics and integrated photonics [10, 11]. These advances have led to the development of new and more advanced modulators, including high-speed modulators, low-loss modulators, and modulators with improved bandwidth and modulation depth. The possibility of controlling the resonance wavelength through the electro-optic change of the effective refractive index can be used to control the intensity of output light [12]. A linear change of the Δn through the applied DC volt provides an optical modulator with a high speed of response for the conventional non-return to zero NRZ and also for advanced modulation techniques such as OFDM transmission [13]. In this work, an optical modulator based on a ring resonator is presented. The mathematical analysis for the electro-optic effect is discussed and numerical modelling of the proposed design is performed using 3D simulation software [14]. The results show the output frequency response of the design that can be used as a modulator in optical communication systems.

Theoretical Modelling of the Proposed Design

Mathematical analysis

Starting from the first Maxwell's equation, the Laplacian of the electrical field is expressed as [15]

$$\nabla^2 E = \omega^2 \mu \varepsilon E - j\omega\mu J. \tag{1}$$

But $J = \dfrac{\partial P}{\partial t}$, where P is the polarization

$$\nabla^2 E - \frac{\omega^2}{c^2} = \mu \frac{\partial^2 P}{\partial t^2}; \tag{2}$$

$$P = \varepsilon_0 \left(\chi^1 \cdot E + \chi^2 \cdot E^2 + \chi^3 \cdot E^3 \right), \tag{3}$$

where χ^1 is the electrical linear susceptibility.

Given that

$$\varepsilon = 1 + \chi^1;$$

$$\varepsilon = \left(n + j\alpha\frac{c}{2\omega}\right)2n + j\alpha\frac{\lambda}{2\pi} = 1 + \chi^1 = 1 + \mathrm{Re}\left(\chi^1\right) + j\,\mathrm{Im}\left(\chi^1\right).$$

So that,

$$n = 1 + \mathrm{Re}\left(\chi^1\right); \tag{4}$$

$$\alpha = j\frac{2\pi}{\lambda}\mathrm{Im}\left(\chi^1\right). \tag{5}$$

The above analysis is valid for low electric fields where only linear susceptibility is used. For high-intensity optical fields, high-level susceptibility (χ^2 and χ^3) needs to be taken into account. However, χ^2 is not included in the calculations because the silicon is a center-symmetrical material [14]. Therefore, only χ^3 will be introduced. χ^3 is the main source of nonlinearity that is excited by the intensity [16]. It can be understood through two effects, i.e. Kerr effect and the Two-Photon Absorption TPA [17]. Generally, Kerr effect can manifest as an intensity-induced phase change while the TPA phenomena is responsible of the material refractive index change due to the generation of free carriers in the waveguide. The effect of χ^3 (both the Kerr effect and TPA) can be modelled mathematically through γ (the complex nonlinear parameter):

$$\gamma A_{eff} = \frac{2\pi}{\lambda}n_2 + j\frac{\beta_{TPA}}{2};$$

$$\gamma A_{eff} = \frac{\omega}{c}\cdot\frac{3\chi^3}{4\varepsilon_0 n^2} + j\frac{3\omega\chi^3}{4\varepsilon_0 c n^2};$$

$$\gamma A_{eff}\left(\frac{4\varepsilon_0 c n^2}{3\omega}\right) = \mathrm{Re}\left(\chi^3\right) + j\,\mathrm{Im}\left(\chi^3\right);$$

$$\left(\gamma_{\mathrm{Re}} + j\gamma_{\mathrm{Im}}\right)A_{eff}\left(\frac{4\varepsilon_0 c n^2}{3\omega}\right) = \mathrm{Re}\left(\chi^3\right) + j\,\mathrm{Im}\left(\chi^3\right).$$

So that

$$\chi^3 = \frac{4}{3}\varepsilon_0 c n^2 n_2 + j\frac{2}{3}\frac{c}{\omega}n^2\beta_{TPA};$$

$$\mathrm{Re}\left(\chi^3\right) + j\,\mathrm{Im}\left(\chi^3\right) = \frac{4}{3}\varepsilon_0 c n^2 n_2 + j\frac{2}{3}\frac{c}{\omega}n^2\beta_{TPA}.$$

Therefore, the intensity-induced phase change coefficient is:

$$n_2 = \frac{2\,\mathrm{Re}\left(\chi^3\right)}{4\varepsilon_0 c n^2}.$$

While the TPA loss coefficient is:

$$\beta_{TPA} = \frac{3\omega\,\mathrm{Im}\left(\chi^3\right)}{2\varepsilon_0 c n^2}.$$

However, there is another nonlinear induced phenomenon is called the free carrier effects (FC) which are the main effects of interest in the waveguide modulators, i.e. FCA (free carrier absorption α_f) and FCD (free carrier dispersion n_f).

Finally, the nonlinear Schrödinger equation can be written as:

$$\frac{\partial A}{\partial z}=\left(-\frac{1}{2}\alpha_0-\frac{1}{2}\alpha_f\frac{n_0}{n}-\frac{1}{2}\frac{\beta_{TPA}}{A_{eff}}|A|^2\right)A-j\left[\beta_2\frac{\partial^2 A}{\partial t^2}+\frac{\omega_0 n_0}{cn}n_f A-\frac{\omega n_2}{cA_{eff}}|A|^2 A\right]. \tag{6}$$

For silicon waveguide modulators, more consideration is given for n_f and α_f [18]:

$$n_f\left(\omega, N_e, N_h\right)=-\frac{q^2}{2\in_0 n_0\omega^2}\left(\frac{N_c}{m_e^*}+\frac{N_h}{m_h^*}\right), \tag{7}$$

where N_h and N_e are the free holes and electrons concentration, respectively; μ_h and μ_e are the mobility of holes and electrons, respectively, while m_e^* and m_h^* are the electrons and holes effective mass, respectively. Based on the Drude model [19], the expressions derived above provide a useful description of the free carriers' dynamics in silicon waveguides. This analysis shows the possibility of controlling the effective refractive index n_f by the presence of the intensity-induced free carriers.

Electro-Optic Effect

In the equations (7) and (8), the two parameters n_f and α_f are proven to be a function of the free carrier concentration. Therefore, any manipulation with this concentration definitely leads to a phase change as well as loss change of propagated light. This fact revealed a way to exploit the ongoing light propagation to be modulated while travelling through the silicon waveguide. Changing the N_e and N_h can be achieved through applying the electric field which leads to an electro-optic effect.

To achieve a controlled change of the effective refractive index in SOI waveguide for the communication window (1.55 and 1.3 nm), either the thermo optic effect or the plasma dispersion effect is used. While, the thermo optic coefficient provides sufficient value of modulation depth, the speed of change is not sufficient for high data modulators, therefore, it is used to switch configuration [20]. Hence, for fast conversion modulation, plasma dispersion-based modulators are the good choice.

Based on Soref and Bennett [21], the change in Δn owing to the change in the free carrier concentration in the silicon material is called the plasma dispersion effect. Mathematically,

$$\Delta n=\Delta n_e+\Delta n_h, \tag{8}$$

where Δn_e and Δn_h represent the change in free electrons and holes, respectively. Therefore, manipulating free carriers concentration in silicon waveguide using electric field results in a modulator that relies on the plasma effect.

Silicon Waveguides

In general, there are two major types of silicon waveguides, namely the rib and slab waveguide structures, as shown in Fig. 1. For electro-optic modulators, rib waveguides are preferable because of their geometry that allows adding the DC bias terminals on the sides. Biased *p-n* junction-based rib waveguides are found in different configurations depending on the doped regions as shown in Fig. 2.

Plasma dispersion effect is commonly used in the electro optic modulators where the electro-refractive nature of this effect allows the doped silicon waveguides to function as phase modulators. In fact, most of the optical transmitters are intensity modulators, therefore, a special photonic design is required to exploit this effect to control the output intensity of light. The Mach–Zehnder interferometer was used to achieve intensity modulation of light through the controlled refractive index of the waveguide

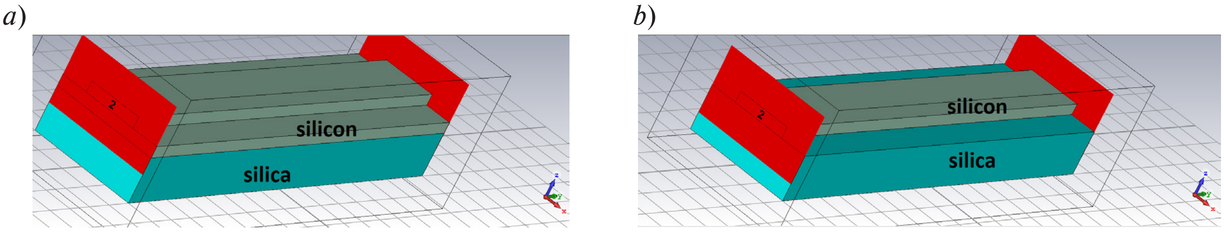

Fig. 1. Silicon on Insulator waveguide structures. Rib type waveguide (*a*) and Slab type waveguide (*b*)

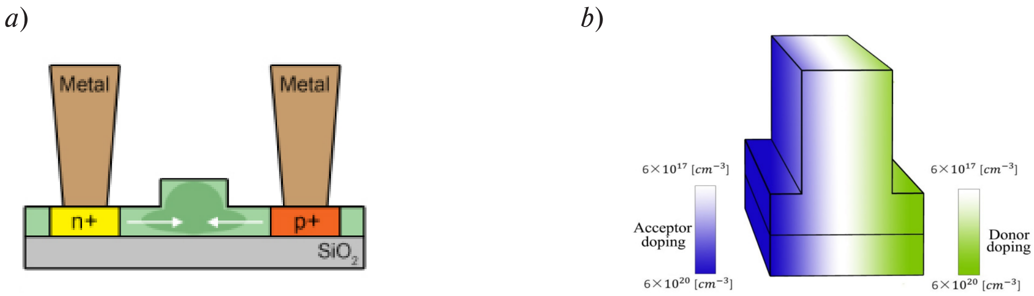

Fig. 2. Cross section of a doped rib waveguide (*a*) showing the metal vias and (*b*) showing the doping level

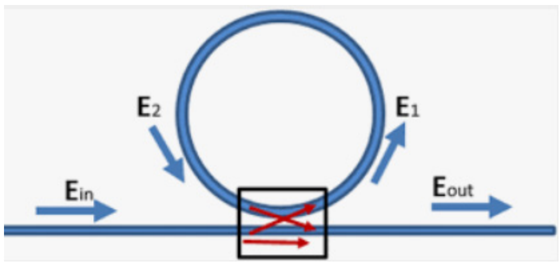

Fig. 3. Layout of a single ring resonator

section [22]. An intensity modulation of light passing through the waveguide is achieved without the need for optical-electrical optical conversion. Ring resonator is proposed to be used to perform the intensity modulation of light through the use of electro-optic effect as will be discussed in the next section.

Ring resonator based optical modulator

Ring resonator is a basic building block in the integrated photonic circuits. It consists of a straight bus waveguide coupled to a ring waveguide to produce a resonant device that is used to select a specific wavelength based on the resonance condition.

The resonance condition depends mainly on the effective refractive index and the ring radius. Ring resonators have been used in different applications ranging from add/drop multiplexing, sensors, and recently as optical modulators. Since the main aim in this study is to manipulate the resonance condition of the ring through the change of the free carrier concentration, it is useful to study the ring resonator response shown in Fig. 3, and explain the resonance condition.

Based on Fig. 3, the electric fields E_{in}, E_{out}, E_1 and E_2 are used to extract the transfer function of this configuration. The transfer function of this device depends mainly on the coupling region (that is the region where the bus and ring waveguide are close to each other). This region is defined by the cross-coupling and through coupling coefficients k and t, respectively. Where $k^2 + t^2 = 1$. Therefore, the relation between electric fields in each point is defined by the following matrix:

$$\begin{bmatrix} E_{\text{out}} \\ E_1 \end{bmatrix} = \begin{bmatrix} t & k \\ -k^* & t^* \end{bmatrix} \begin{bmatrix} E_{\text{in}} \\ E_2 \end{bmatrix}. \tag{9}$$

Also, the relation between the electric fields inside the ring which describes the round-trip propagation of the light is given by:

$$E_2 = \alpha e^{-j\phi} E_1.$$

Here, α represents the attenuation inside the ring waveguide, while ϕ is the phase shift accumulated along the round trip. ϕ is related to the wavelength of the light λ, the length of ring l as well as the mode effective refractive index n_{eff}, and can be expressed mathematically through the following equation:

$$\phi = \frac{2\pi}{\lambda} \ln_{eff}.$$

Therefore, the output field can be expressed as:

$$E_{\text{out},1} = \frac{t - \alpha e^{-j\phi}}{1 - \alpha t e^{-j\phi}} E_{\text{in},1}. \tag{10}$$

The behavior of such device is obtained by calculating the transfer function that relates the output filed E_{out} to the input field E_{in} where the intensity and phase information are defined by relation $\left| \frac{E_{\text{out}}}{E_{\text{in}}} \right|$. Also, the optical intensity transfer function is obtained as [4]:

$$I_{\text{out}} = \frac{|t|^2 + \alpha^2 - 2\alpha |t| \cos(\phi + \theta)}{1 + \alpha^2 |t|^2 - 2\alpha |t| \cos(\phi + \theta)} I_{\text{in}}. \tag{11}$$

Plotting this function with respect to the wavelength shows a periodic change at specific wavelengths that are coupled from the straight waveguide to the ring and resonate inside the resonator as shown in Fig. 4. There, $S_{2,1}$ represents the power intensity I_{out} at port 2, and $S_{1,1}$ is the power reflection coefficient at port 1. The separation between two successive wavelengths is called the Free Spectral Range (FSR, Fig. 4, *b*), and defined as:

$$FSR = \frac{\lambda^2}{n_g L}. \tag{12}$$

Here, n_g is the group refractive index of the device.

The most important consideration in the design of the resonator ring based optical modulator is the incorporation of the DC bias terminals in the bent waveguide to manipulate n_{eff}. Application of voltage on the bent waveguide will induce a change in the effective refractive index, which will lead to a shift in the resonance wavelength as shown in Fig. 5. Therefore, this effect can be used to design a ring resonator based optical modulator that performs all optical intensity modulation of light with a small size ring resonator providing high density integration of devices with high data rates of transmission. The results shown in Fig. 5 are calculated based on a MATLAB code. However, in the next section, a numerical simulation of the small size optical modulator is presented using a 3D simulation software to validate the design.

a)

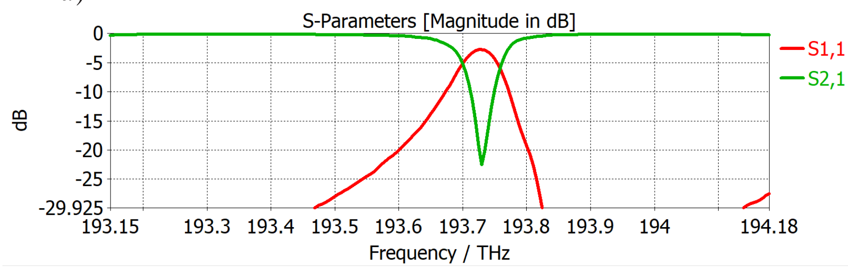

b)

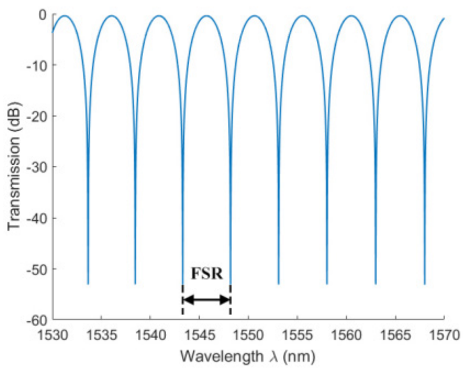

Fig. 4. Transmission of a single ring resonator CST representation (*a*), the representation of the FSR of a single ring (*b*) calculated using MATLAB

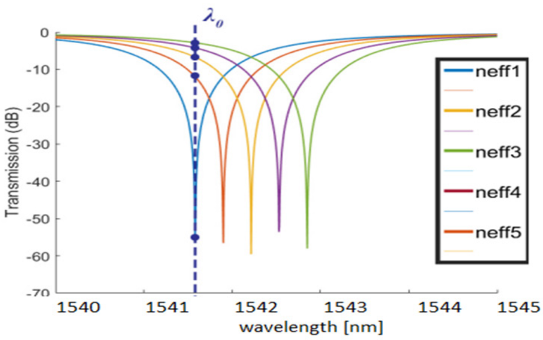

Fig. 5. A MATLab calculated response of a single ring resonator for different values of the effective refractive index. $n_{eff1} = 0$, $n_{eff2} = 1\times10^{-4}$, $n_{eff3} = 2\times10^{-4}$, $n_{eff4} = 4\times10^{-4}$, $n_{eff5} = 5\times10^{-4}$

CST simulation results and discussion

In this section, the silicon on insulator based ring resonator is modeled using a 3D simulation software as shown in Fig. 6. The CST studio suite is used to model a ring resonator with a radius of 16 μ*m* coupled to a straight bus with dimensions of 0.48 μ*m* width ×0.25 μ*m* height, to ensure a single mode propagation. The material of the ring and bus waveguide is made of silicon (Si) with refractive index 3.45 which is built on silicon dioxide layer (SiO_2) of a 1.45 refractive index to achieve a high refractive index contrast. This ensures the guidance of light, the high refractive index region with the high confinement, Fig. 7. The upper clad was set to be air with $n = 1$.

The time domain solver result of the CST simulation is shown in Fig. 8. Different values of the effective refractive index are calculated numerically by using the doped silicon-based rib waveguide as shown in

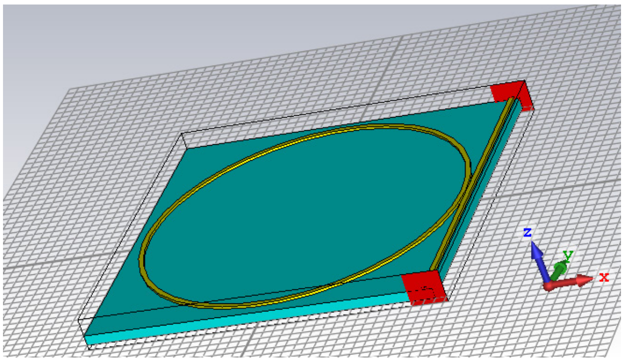

Fig. 6. CST representation of a ring resonator

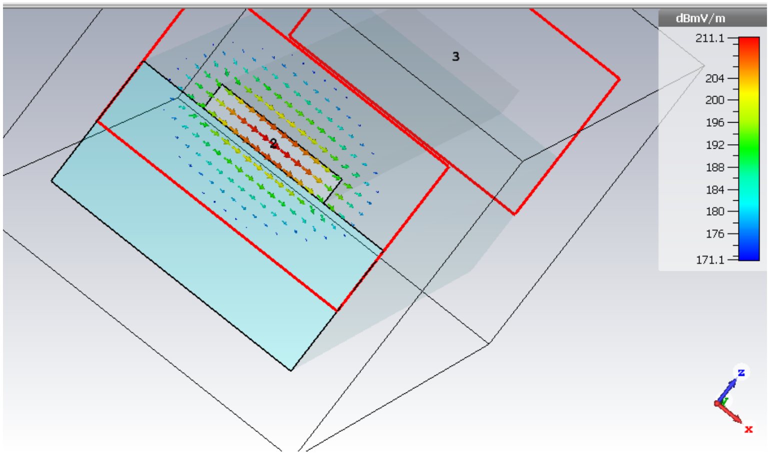

Fig. 7. CST mode profile representation in the rib waveguide

Fig. 2. The ring resonator response shown in Fig. 8 shows a good agreement with that calculated in Fig. 5, which supports the concept of using the effective refractive change to obtain intensity modulation.

The idea in Fig. 8 is that the resonance wavelength is changing every time the effective refractive index changes. Therefore, for no change in n_{eff1} the resonance wavelength (1542.7 nm) will face an attenuation of almost –40 dB. Changing n_{eff} (caused by the applied filed) will lead to a shift in resonance frequency to a longer wavelength and expose the reference wavelength (1542.7 nm) to another attenuation level as shown in Fig. 8 (see the linear dotted line).

A linear relation between the electric-filed change (information signal) and the resonance change is crucial in considering the efficiency of the proposed modulator. This relation needs to be as linear as possible in order to have a real intensity modulation at the output of the ring resonator. Fig. 9 shows almost linear relationship between the output intensity of the modulator with the change of the effective refractive index induced by the electric field. Achieving a linear change means light can be easily modulated with the required information signal that is used as the drive voltage for the metal vias.

Conclusion

In a ring resonator-based optical modulator, the intensity of the light passing through the resonator is controlled by changing the refractive index of the waveguide material, which in turn changes the resonance conditions of the resonant modes. This change in the resonance conditions can be achieved by applying an electrical field to modulating electrodes which are placed near the waveguide. This work

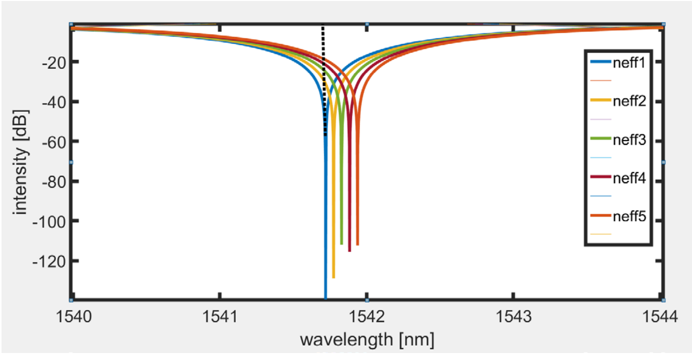

Fig. 8. CST calculated transmission of a single ring resonator for the same values of the effective refractive index in Fig. 5

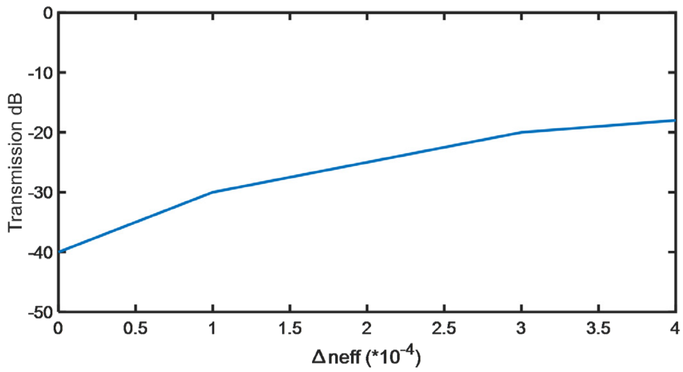

Fig. 9. The relation between the output intensity of the modulator with the effective refractive change

examined, theoretically and numerically, the possibility of achieving a modulator like behavior using a small size ring resonator to support the search for the high integration density in all optical photonic circuits. The frequency response of the single ring resonator is presented first with a stronger emphasis on the effect of changing the effective refractive index on the resonance wavelength. Using doped silicon-based rib waveguide provides the possibility of adding copper vias around the circumference of the ring. Via these vias, a voltage change produced by the information signal can be used to alter the free carrier's concentration in the waveguide. This, in turn, will change the propagation constant through the change in the effective refractive index and finally produce a controlled intensity for the pumped CW light at the input of the ring. A theoretical calculation is presented and the response of the proposed modulator is first presented using MATLab, then the performance was validated using 3D simulation software. Ring resonator-based optical modulators have several advantages over other types, including high modulation efficiency, low power consumption, low insertion loss, and compact size.

Future work

This work is part of an ongoing project that aims to design an integrated photonic circuit of a transceiver (Comb generator and modulator) based on SOI ring resonators. Multiple carrier wavelengths transceiver that can achieve >100 Gb/s capacity is drawing researchers' attention. A significant interest is devoted to the concept of using a single laser input fed to an optical wavelength comb generator instead of using distributed feedback lasers. Comb generators find implementations in WDM transceiver environments. Appropriate shaping of the spectrum around the optical carrier by means of electro-optic modulation of a Continuous Wave (CW) source is the basis of a modulator-based comb generator. The comb shape is determined mainly by two factors: the applied electrical signal waveform and achieved modulation depth. In the ring resonators, the modulation depth is determined by the coupling coefficient and the *p-n* junction operating condition (modulation regime).

REFERENCES

1. **Xiao S., Khan M.H., Shen H., Qi M.** Silicon-on-insulator microring add-drop filters with free spectral ranges over 30 nm, *Journal of lightwave technology*, 2008, vol. 26, no. 2, pp. 228–236.

2. **Densmore A., Xu D., Waldron P., Janz S., Cheben P., Lapointe J., Delâge A., Lamontagne B., Schmid J.H., Post E.** A silicon-on-insulator photonic wire based evanescent field sensor, *Photonics technology letters*, IEEE, 2006, vol. 18, no. 23, pp. 2520–2522.

3. **Selvaraja S.K., Jaenen P., Bogaerts W., van Thourhout D., Dumon P., Baets R.** Fabrication of photonic wire and crystal circuits in silicon-on-insulator using 193-nm optical lithography, *Lightwave technology journal*, 2009, vol. 27, no. 18, pp. 4076–4083.

4. **Bogaerts W., Fiers M., Dumon P.** Design challenges in silicon photonics, *Selected topics in quantum electronics*, IEEE, 2014, vol. 20, no. 4, pp. 1–8.

5. **Mansoor R.D., Sasse H., Asadi M.Al, Ison S.J., Duffy A.P.** Over coupled ring resonator-based add/drop filters, *IEEE journal of quantum electronics*, 2014, vol. 50, no. 8, pp. 598–604.

6. **Mansoor R., Koziel S., Sasse H., Duffy A.** Crosstalk suppression bandwidth optimisation of a vertically coupled ring resonator add/drop filter, *IET optoelectronics*, 2015, vol. 9, no. 2, pp. 30–36.

7. **Mansoor R., Sasse H., Ison S., Duffy A.** Crosstalk bandwidth of grating-assisted ring resonator add/drop filter, *Optical and quantum electronics*, 2015, vol. 47, pp. 1127–1137.

8. **Koziel S., Ogurtsov S.** Simulation-driven optimization approach for fast design of integrated photonic components, In 30th annual review of progress in applied computational electromagnetic, Jacksonville, FL, 2014, pp. 679–684.

9. **Mansoor R., Duffy A.** Optical racetrack resonators for strain sensing applications, 2019.

10. **Koch T.L., Koren U.** Semiconductor photonic integrated circuits, *Quantum electronics*, IEEE journal, 1991, vol. 27, no. 3, pp. 641–653.

11. **Xu Q., Schmidt B., Pradhan S., Lipson M.** Micrometre-scale silicon electro-optic modulator, *Nature*, 2005, vol. 435, no. 7040, pp. 325–327.

12. **Kolchin P., Belthangady C., Du S., Yin G.Y., Harris S.E.** Electro-optic modulation of single photons, *Physical review letters*, 2008, vol. 101, no. 10, pp. 103601.

13. **Zhang X., Babar Z., Petropoulos P., Haas H., Hanzo L.** The evolution of optical OFDM, *IEEE communications surveys & tutorials*, 2021, vol. 23, no. 3, pp. 14300–1457.

14. CST, 3D electromagnetic simulation software, Available at: www.cst.com

15. **Huray P.G.** Maxwell's equations, John Wiley & Sons, 2011.

16. **Hon N.K., Soref R., Jalali B.** The third-order nonlinear optical coefficients of Si, Ge, and $Si_{1-x}Ge_x$ in the midwave and longwave infrared, *Journal of applied physics*, 2011, vol. 110, no. 1, pp. 9.

INFORMATION ABOUT AUTHOR / СВЕДЕНИЯ ОБ АВТОРЕ

Mansoor Riyadh
Мансур Р.
E-mail: riyadhdmu@mu.edu.iq
ORCID: https://orcid.org/0000-0002-6542-0087

Submitted: 24.08.2023; Approved: 04.10.2023; Accepted: 11.10.2023.
Поступила: 24.08.2023; Одобрена: 04.10.2023; Принята: 11.10.2023.

Computing, Telecommunication and Control, 2023, Vol. 16, No. 3, Pp. 29–38.
Информатика, телекоммуникации и управление. 2023. Том 16, № 3. С. 29–38.

Research article
DOI: https://doi.org/10.18721/JCSTCS.16303
UDC 621.3.049.774.2

MASH 2-2 DELTA-SIGMA MODULATOR WITH DYNAMIC ELEMENT MATCHING IN 0.18 μm CMOS TECHNOLOGY

M.M. Pilipko , *D.V. Morozov* ,
M.S. Yenuchenko ✉

Peter the Great St. Petersburg Polytechnic University,
St. Petersburg, Russian Federation

✉ mixeme@outlook.com

Abstract. Design details and results of post-layout simulation for multi-stage noise-shaping 2-2 delta-sigma modulator based on 0.18 μm CMOS from JSC Mikron are presented. The circuit consists of two similar 2^{nd} order stages connected sequentially and based on fully differential operational transconductance amplifiers and switched capacitors. The delta-sigma modulator processes a differential input signal and has a two-bit quantizer, which is a simple 2-bit analog-to-digital converter that contains three differential comparators. A special digital circuit is used, which provides dynamic element matching, also known as dynamic weighted averaging in digital-to-analog converter, which is connected to the switched capacitors. Supply voltage is 1.8V. Clock frequency is 1 MHz. Frequency band of the input signal is up to 8 kHz. Dynamic range is 62 dB. Power consumption is 1.9 mW.

Keywords: ADC, DSM, switched capacitors, DEM, OTA, differential comparator, 2^{nd} order

Acknowledgements: Production of the integrated circuit was carried out at the expense of the Ministry of Science and Higher Education of Russia within the framework of the federal project "Preparation of personnel and scientific foundation for the electronics industry" under the state assignment for the research work "Development of a methodology for prototyping of electronic component base at domestic microelectronic production facilities on the basis of MPW service" (FSMR-2023-0008).

Citation: Pilipko M.M., Morozov D.V., Yenuchenko M.S. MASH 2-2 Delta-Sigma Modulator with Dynamic Element Matching in 0.18 μm CMOS Technology. Computing, Telecommunications and Control, 2023, Vol. 16, No. 3, Pp. 29–38. DOI: 10.18721/JCSTCS.16303

Научная статья
DOI: https://doi.org/10.18721/JCSTCS.16303
УДК 621.3.049.774.2

ДЕЛЬТА-СИГМА-МОДУЛЯТОР СО СТРУКТУРОЙ MASH 2-2 И ДИНАМИЧЕСКИМ СОГЛАСОВАНИЕМ ЭЛЕМЕНТОВ ПО ТЕХНОЛОГИИ КМОП 0,18 МКМ

М.М. Пилипко , *Д.В. Морозов* ,
М.С. Енученко ✉

Санкт-Петербургский политехнический университет Петра Великого,
Санкт-Петербург, Российская Федерация

✉ mixeme@outlook.com

Аннотация. Представлены процесс разработки и результаты моделирования в том числе с паразитными параметрами для многокаскадного дельта-сигма модулятора со структурой MASH 2-2 на основе технологии АО "Микрон" КМОП 0,18 мкм. Схема состоит из двух похожих каскадов 2-го порядка, соединённых последовательно и использующих полностью дифференциальные операционные транскондуктивные усилители и переключаемые конденсаторы. Дельта-сигма модулятор обрабатывает входной дифференциальный сигнал и имеет двухразрядный квантователь, который представляет собой простой 2-разрядный аналого-цифровой преобразователь, содержащий три дифференциальных компаратора. Применяется специальная цифровая схема, которая обеспечивает динамическое согласование элементов, также известное как динамическое взвешенное усреднение в цифро-аналоговом преобразователе, подключенном к массиву переключаемых конденсаторов. Напряжение питания составляет 1,8 В. Тактовая частота составляет 1 МГц. Диапазон частот входного сигнала составляет до 8 кГц. Динамический диапазон составляет 62 дБ. Потребляемая мощность составляет 1,9 мВт.

Ключевые слова: ДСМ, АЦП, переключаемые конденсаторы, ДСЭ, ОТУ, дифференциальный компаратор, второй порядок

Благодарности: Производство интегральной микросхемы было выполнено за счет средств Минобрнауки России в рамках федерального проекта «Подготовка кадров и научного фундамента для электронной промышленности» по гос. заданию на выполнение научно-исследовательской работы «Разработка методики прототипирования электронной компонентной базы на отечественных микроэлектронных производствах на основе сервиса MPW» (FSMR-2023-0008).

Для цитирования: Pilipko M.M., Morozov D.V., Yenuchenko M.S. MASH 2-2 Delta-Sigma Modulator with Dynamic Element Matching in 0.18 μm CMOS Technology // Computing, Telecommunications and Control. 2023. Т. 16, № 3. С. 29–38. DOI: 10.18721/JCSTCS.16303

Introduction

Delta-sigma modulators achieve a high degree of insensitivity to analog circuit imperfections as they are based on a combination of oversampling and quantization error shaping techniques. This makes them the best choice in many cases for implementing on-chip analog-to-digital interfaces in today's integrated CMOS circuits. Increasing the analog-to-digital converter (ADC) resolution requires increasing the order of the delta-sigma modulator. Modulators up to the second order are stable circuits, to implement modulators of a higher order, Multi-stAge noise-SHaping (MASH) structures are used [1–6]. Another way to increase the ADC resolution is a multibit quantizer in the delta-sigma modulator which also demands a multibit digital-to-analog converter (DAC) in the feedback loop.

This paper presents realization of the MASH 2-2 delta-sigma modulator based on 0.18 μm CMOS from JSC Mikron. The paper is organized as follows. Section I gives a brief description of the delta-sigma modu-

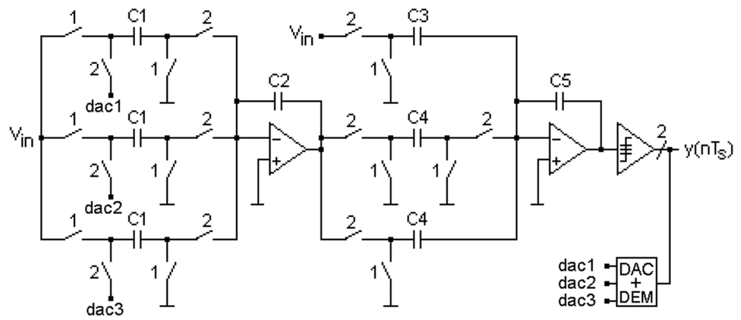

Fig. 1. Simplified structure of the unbalanced 2nd order delta-sigma modulator

lator structure based on switched capacitors. Section II presents the circuit for generating signals of phases to switch capacitors in the modulator. Section III describes the differential comparator for the ADC-DAC part, which is discussed in Section IV. Section V is devoted to the delta-sigma modulator layout and its simulation results. Finally, conclusions are given.

I. Delta-sigma modulator structure

The switched-capacitor delta-sigma modulator is designed in accordance with the recommendations of papers [7–10] as MASH 2-2. Its circuit consists of two similar 2nd order stages connected sequentially. A 2nd order stage is shown in Figure 1 as a simplified unbalanced circuit based on two operational transconductance amplifiers (OTAs). The quantizer is a simple 2-bit ADC that contains three differential comparators and generates the stage output code. The input signal of the delta-sigma modulator is supplied during the first phase to three switched capacitors in the first summing integrator, and during the second phase via direct connection to the second integrator. In the first integrator, during the second phase, the 2-bit signal of the digital-to-analog converter (DAC) is supplied to the switched capacitors. Here, DEM is dynamic element matching. The DAC output code is in unary form (digits are *dac*3, *dac*2, *dac*1). In the simplest case, the output signals of the comparators in thermometric code are supplied. In the second integrator, during the second phase, signals from one resistive element (based on a capacitor and four switches) and two capacitive elements are added. The capacitor ratios in Fig. 1 are given in the following proportions:
in both stages C1=0.5 pF and C2=3 pF, therefore, the attenuation coefficient in the first integrator is set to 3*C1/C2=1/2,
in the first stage C3=0.5 pF, C4=1 pF, and C5=2 pF, therefore, the attenuation coefficients in the second integrator of the first stage are set to C3/C4=1/2 and C4/C5=1/2,
in the second stage C3=0.5 pF, C4=1 pF, and C5=1 pF, therefore, the attenuation coefficients in the second integrator of the second stage are set to C3/C4=1/2 and C4/C5=1.

The integrators of the delta-sigma modulator are based on a fully differential OTA [10, 11]. The OTA core is the folded-cascode circuit, with the parallel connection of the p-type and n-type input differential pairs and has the differential rail-to-rail output. The OTA has 69.8 dB gain and unity gain bandwidth of 27.0 MHz and phase margin of 78.5 degrees at 5 pF load. The current consumption of OTA at the supply voltage of 1.8 V is about 200 μA. The amplifier noise referred to the input at 1 kHz is 383 nV/√Hz.

II. Circuit for generating signals of the first and second phases

The circuit for generating signals of the first and second phases is shown in Fig. 2, *a*. Based on the input clock signal *clk*, the circuit generates signals for the first and second phases, as well as the phase signals inverse to them. After passing through several inverters ‘inv’, the signal is fed to the delay line based on ‘inv’ and ‘inv_long’ (inverters with a large transistor length). Then, using NAND elements ‘nand’, the signals

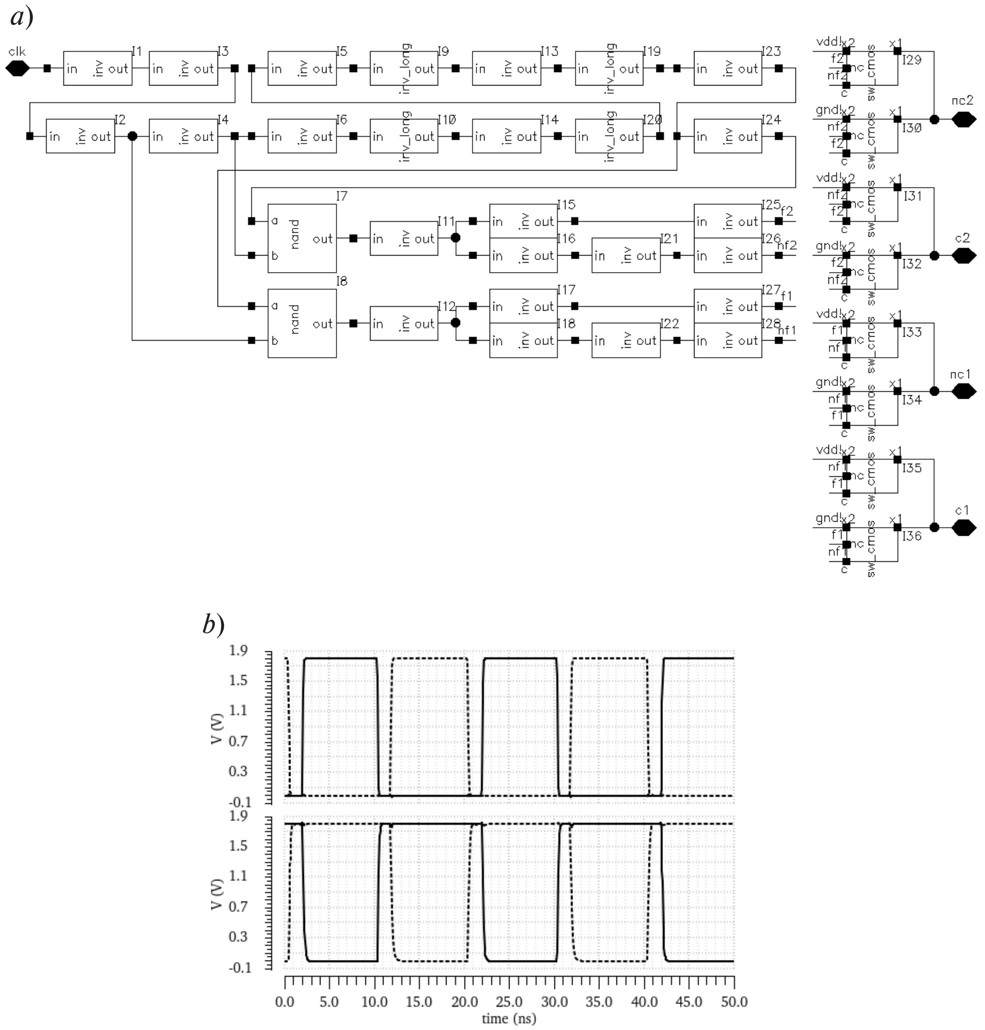

Fig. 2. Circuit for generating signals of the first and second phases (*a*); Simulation results (*b*)

before and after the delay line are multiplied, which makes it possible to create protective time intervals between the working phase intervals. In this way, signals *f*1, *nf*1, f2, *nf*2 are generated that control analog multiplexers based on CMOS switches ‘sw_cmos’. The simulation results of the output signals *c*1, *nc*1 of the first phase and *c*2, *nc*2 of the second phase are shown in Fig. 2, *b* (*c*1 and *c*2 are on the top graph, *nc*1 and *nc*2 are on the bottom, with *c*2 and *nc*2 shown with the dotted line).

III. Differential comparator

The circuit of the differential comparator is shown in Fig. 3, *a*. The differential comparator has four inputs, two for the analog signals of the integrator *vp*, *vm* and two for the reference levels *vp*2, *vm*2. When the clock signal *clk* is at ground level, the input signals of the inverters ‘inv’ are equal to the supply voltage. When the clock signal *clk* becomes equal to the supply voltage, transistors M3, M6 go to cutoff, and the transistors M2, M10 make a decision depending on the comparison of currents through transistors M1 and M4, M7 and M11. Inverters ‘inv’ provide decoupling between the circuit core and the latch using NOR elements ‘nor’. The latch stores the comparator decision while the core is in the reset phase, that is, when the clock signal *clk* is at ground. The simulation results of the differential comparator are shown in Fig. 3, *b*. The top graph shows the input signals. The analog signals of the integrator *vp*, *vm* are triangular, the reference levels *vp*2, *vm*2 are both equal to 900 mV, i.e. half the supply voltage.

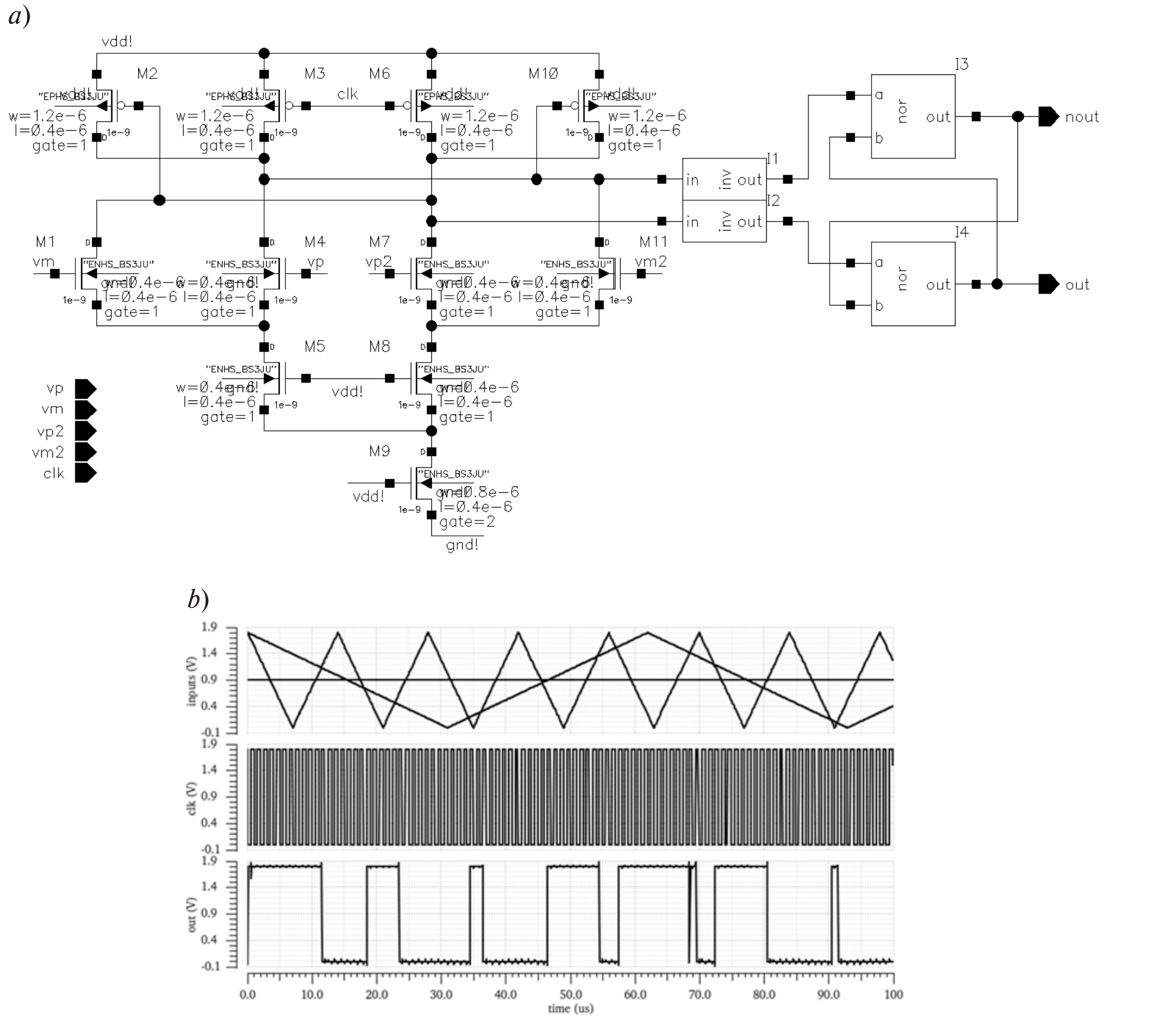

Fig. 3. Circuit of differential comparator (*a*); Simulation results (*b*)

IV. ADC-DAC part

The circuit of ADC-DAC part with DEM is shown in Fig. 4, *a*. The circuit contains a resistive divider, three comparators 'comparator' with output buffers on inverters 'inv', an adder 'adder' in accordance with paper [12, 13] as an encoder of the thermometric code *t*<1:3> into the binary code *b*<0:1> and analog multiplexers on CMOS switches 'sw_cmos' that generate DAC signals *th*<1:3> and *nth*<1:3>. In this circuit, the output signals of the DAC are not the same as the output signals of the comparators. A special digital circuit is used, consisting of D-flip-flops 'd_ff' and logic elements, which provides dynamic element matching (DEM), also known as dynamic weighted averaging [14, 15] in the DAC. The resistive divider is based on resistors with a nominal value of 11 kOhm. With the supply voltage of 1.8 V, the voltage levels in the *res*<1:3> nodes are 600 mV, 900 mV, 1200 mV, respectively.

Due to the variation in the values of the elements, the transfer curve of the DAC turns out to be nonlinear. The nonlinearity of the DAC leads to the appearance of unwanted harmonics in the operating frequency range of the modulator spectrum. In Fig. 1, a unary DAC is used consisting of three capacitors of the same value, let's denote them A, B, C. As can be seen from Table 1, depending on the 2-bit output code of the modulator, no element of the DAC is connected or 1, 2 or 3 elements are connected. Table 1 shows three options for connecting the elements. If only one of them is used, the effect of mismatch on *a*) *b*)

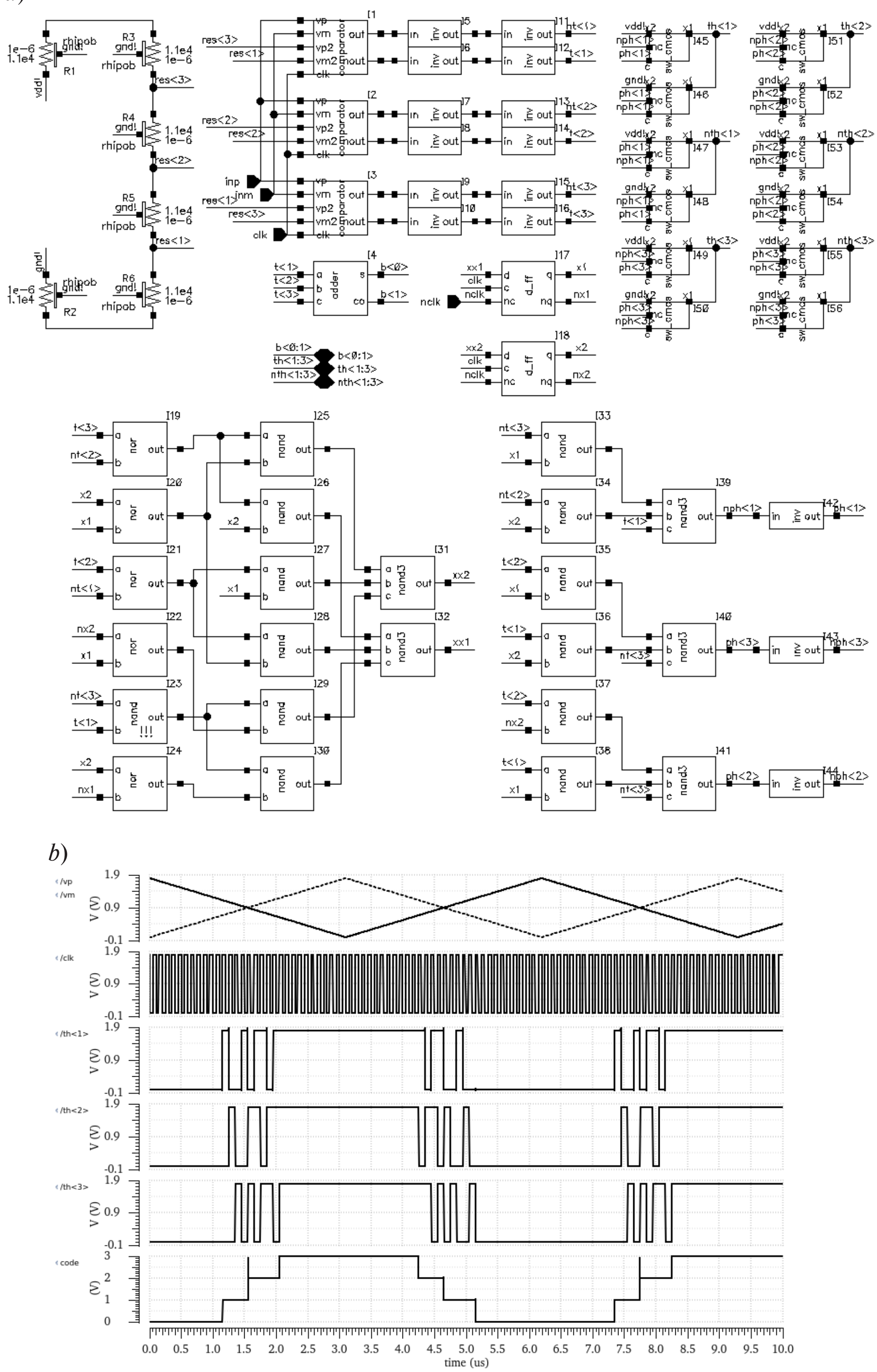

Fig. 4. Circuit of ADC-DAC part with DEM (*a*); Simulation results (*b*)

the nonlinearity of the DAC is maximally negative. If the connection options are used alternately, then the nonlinearity of the DAC is averaged and reduced by √3 times. If the cyclical appearance of options for connecting the elements is excluded, the nonlinearity will turn into noise.

Table 1

Operating principle DEM of the DAC control circuit

b<1:0>	t<3:1>	Options for connecting the elements		
		x2x1		
		00	01	10
00	000	–	–	–
01	001	A	B	C
10	011	A + B	B + C	C + A
11	111	A + B + C	B + C + A	C + A + B

The simplest way to use options for connecting the elements is one after another. However, the connection option is only important in two cases of the input code 01 and 10, when one or two elements are connected. Therefore, it is advisable to switch to the next option only in these two cases. In addition, it is possible to switch options clockwise when code 01 appears and counterclockwise when code 10 appears. Since these codes have an equal probability of occurrence, switching will occur at random times in a random direction. For this case, the logical expressions in the circuit (see bottom of Fig. 4 *a*) have the following form

$$xx2=\overline{\overline{\overline{t3+\overline{t2}}\cdot\overline{x2+x1}}\cdot\overline{\overline{t2+\overline{t1}}\cdot x1}\cdot\overline{\overline{\overline{t3}\cdot t1}\cdot\overline{\overline{x2}+x1}}};$$

$$xx1=\overline{\overline{\overline{t3+\overline{t2}}\cdot x2}\cdot\overline{\overline{t2+\overline{t1}}\cdot\overline{x2+x1}}\cdot\overline{\overline{\overline{t3}\cdot t1}\cdot\overline{x2+\overline{x1}}}};$$

$$ph3=\overline{\overline{t2\cdot x1}\cdot\overline{t1\cdot x2}\cdot\overline{t3}};$$

$$ph2=\overline{\overline{t2\cdot\overline{x2}}\cdot\overline{t1\cdot x1}\cdot\overline{t3}};$$

$$\overline{ph1}=\overline{\overline{\overline{t3}\cdot x1}\cdot\overline{\overline{t2}\cdot x2}\cdot t1}.$$

As depicted in Fig. 4, *a*, signals *xx*2 and *xx*1 act on the inputs of D flip-flops ‘d_ff’ and are stored for one clock cycle of *clk*, and signals *ph*<1:3> and *nph*<1:3> control multiplexers based on CMOS switches ‘sw_cmos’ that form DAC output signals *th*<1:3> and *nth*<1:3>.

The simulation results of ADC-DAC part with DEM is shown in Fig. 4, *b*. The input signals *vp*, *vm*, clock signal *clk*, DAC signals *th*<1:3> and the code signal *code*=2**b*<1>+*b*<0> formed from the output bits are presented. As seen, when *code* is equal to 1 or 2, the signals to control DAC *th*<1:3> are switched according to the described idea, which leads to error averaging and compensates for the nonlinearity of the DAC transfer curve.

V. Delta-sigma modulator layout and simulation results

The delta-sigma modulator layout is shown in Fig. 5. Sizes of the layout are 430 μm × 220 μm. The circuit consists of two similar stages connected sequentially. The attenuation coefficients in the second integrator of the first and second stages are different, so capacitor arrays look different. The last OTA in the second stage has half the load in comparison with other OTAs. Thus sizes of the last OTA layout are 32 μm × 35 μm, while sizes of other OTAs are 51 μm × 35 μm. The last OTA has 68.7 dB gain, and at 2.5 pF load it shows a unity gain bandwidth of 27.5 MHz and phase margin of 78.4 degrees. The current consumption of the last OTA at the supply voltage of 1.8 V is about 120 μA. The last amplifier noise referred to the input at 1 kHz is 450 nV/√Hz.

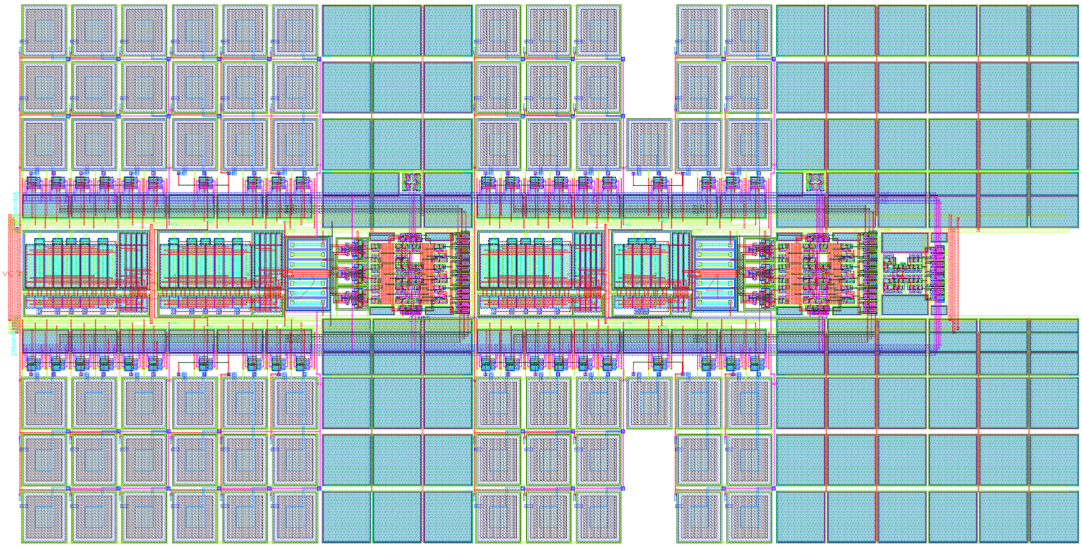

Fig. 5. Delta-sigma modulator layout

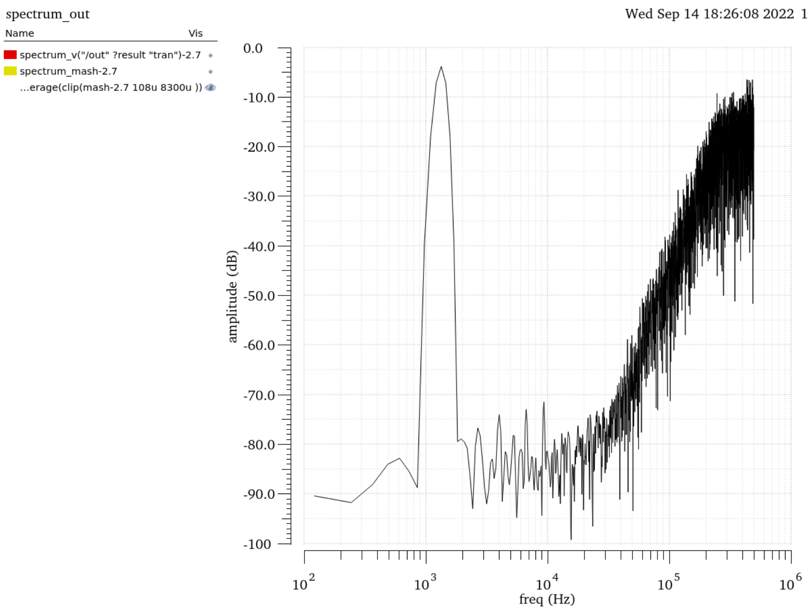

Fig. 6. Simulation results of delta-sigma modulator

Post-layout simulation results of the delta-sigma modulator are shown in Fig. 6. The output code was composed from two 2-bit outputs of the first and second stages. From the spectrum, the 4^{th} order noise shaping property can be seen. At the clock frequency of 1 MHz and the frequency band of the input signal up to 8 kHz, the dynamic range is 62 dB. Power consumption is 1.9 mW.

Conclusions

Realization of the MASH 2-2 delta-sigma modulator based on 0.18 µm CMOS technology from JSC Mikron is described. Supply voltage is 1.8 V. Clock frequency is 1 MHz. Frequency band of the input signal is up to 8 kHz. The delta-sigma modulator layout occupies an area of 430 µm × 220 µm. Post-layout simulation results of the delta-sigma modulator are given. Dynamic range is 62 dB. Power consumption is 1.9 mW.

REFERENCES

1. **de la Rosa J.M.** Sigma-Delta Modulators: Tutorial Overview, Design Guide, and State-of-the-Art Survey, in *IEEE Transactions on Circuits and Systems I: Regular Papers*, 2011, vol. 58, no. 1, pp. 1–21. DOI: 10.1109/TCSI.2010.2097652

2. **Morgado A., del Rio R., dela Rosa J.M.** High-Efficiency Cascade ΣΔ Modulators for the Next Generation Software-Defined-Radio Mobile Systems, in *IEEE Transactions on Instrumentation and Measurement*, 2012, vol. 61, no. 11, pp. 2860–2869. DOI: 10.1109/TIM.2012.2200394

3. **de la Rosa J.M., Schreier R., Pun K.-P., Pavan S.** Next-Generation Delta-Sigma Converters: Trends and Perspectives, in *IEEE Journal on Emerging and Selected Topics in Circuits and Systems*, 2015, vol. 5, no. 4, pp. 484–499. DOI: 10.1109/JETCAS.2015.2502164

4. **Payandehnia P., He T., Wang Y., Temes G.C.** Digital Correction of DAC Nonlinearity in Multi-Bit Feedback A/D Converters: Invited tutorial, 2020 *IEEE Custom Integrated Circuits Conference* (*CICC*), Boston, MA, USA, 2020, pp. 1–8. DOI: 10.1109/CICC48029.2020.9075916

5. **Jing C., Li T., Gao B., Gong M.** A MASH2-2 Sigma Delta Modulator with NTF Zero Optimization Technique, 2022 *5th International Conference on Communication Engineering and Technology* (*ICCET*), Shanghai, China, 2022, pp. 68–72. DOI: 10.1109/ICCET55794.2022.00021

6. **Xu J., Xu W., Tian Q.** The Design of a High-Accuracy Sigma-Delta Modulator with 2-2 Mash Structure, 2023 *6th International Conference on Electronics Technology* (*ICET*), Chengdu, China, 2023, pp. 1007–1011. DOI: 10.1109/ICET58434.2023.10211909

7. **Hao San et al.** Second-order ΔΣAD modulator with novel feedforward architecture, 2007 50th Midwest Symposium on Circuits and Systems, 2007, pp. 148–151. DOI: 10.1109/MWSCAS.2007.4488558

8. **Korotkov A.S., Pilipko M.M., Morozov D.V., Hauer J.** Delta-sigma modulator with a 50-MHz sampling rate implemented in 0.18-μm CMOS technology, *Russian Microelectronics*, 2010, vol. 39, no. 3, pp. 210–219. DOI: 10.1134/S106373971003008X

9. **Kozlov A.S., Pilipko M.M.** A Second-order Sigma-delta Modulator with a Hybrid Topology in 180nm CMOS, 2020 IEEE Conference of Russian Young Researchers in Electrical and Electronic Engineering (EIConRus), St. Petersburg and Moscow, Russia, 2020, pp. 144–146. DOI: 10.1109/EIConRus49466.2020.9039246

10. **Korotkov A.S., Morozov D.V., Pilipko M.M., Yenuchenko M.S.** Sigma-Delta ADC on SOI Technology for Working at High Temperatures, *Radioelectronics and Communications Systems*, 2020, vol. 63, no. 11, pp. 586–595. DOI: 10.3103/S0735272720110035

11. **Morozov D.V., Pilipko M.M., Korotkov A.S.** Delta-sigma modulator of the analog-to-digital converter with ternary data encoding, *Russian Microelectronics*, 2011, vol. 40, no. 1, pp. 59–69. DOI: 10.1134/S1063739710061034

12. **Morozov D.V., Pilipko M.M.** A circuit implementation of a single-bit CMOS adder, *Russian Microelectronics*, 2013, vol. 42, no. 2, pp. 113–118. DOI: 10.1134/S106373971302008X

13. **Pilipko M.M., Morozov D.V.** The XOR-MAJ Thermometer-to-Binary Encoder Structure Stable to Bubble Errors, *IEEE Transactions on Circuits and Systems II: Express Briefs*, 2021, vol. 68, no. 7, pp. 2613–2617. DOI: 10.1109/TCSII.2021.3052695

14. **Baird R.T., Fiez T.S.** Linearity enhancement of multibit ΔΣ A/D and D/A converters using data weighted averaging, in *IEEE Transactions on Circuits and Systems II: Analog and Digital Signal Processing*, 1995, vol. 42, no. 12, pp. 753–762. DOI: 10.1109/82.476173

15. **Sanyal A., Chen L., Sun N.** Dynamic Element Matching With Signal-Independent Element Transition Rates for Multibit ΔΣ Modulators, in *IEEE Transactions on Circuits and Systems I: Regular Papers*, 2015, vol. 62, no. 5, pp. 1325–1334. DOI: 10.1109/TCSI.2015.2407434

INFORMATION ABOUT AUTHORS / СВЕДЕНИЯ ОБ АВТОРАХ

Pilipko Mikhail M.
Пилипко Михаил Михайлович
E-mail: m_m_pilipko@rambler.ru
ORCID: https://orcid.org/0000-0003-3813-6846

Morozov Dmitry V.
Морозов Дмитрий Валерьевич
E-mail: dvmorozov@inbox.ru
ORCID: https://orcid.org/0000-0003-3403-0120

Yenuchenko Mikhail S.
Енученко Михаил Сергеевич
E-mail: mixeme@outlook.com
ORCID: https://orcid.org/0000-0002-5301-3871

Submitted: 17.07.2023; Approved: 25.09.2023; Accepted: 11.10.2023.
Поступила: 17.07.2023; Одобрена: 25.09.2023; Принята: 11.10.2023.

Computing, Telecommunication and Control, 2023, Vol. 16, No. 3, Pp. 39–53.
Информатика, телекоммуникации и управление. 2023. Том 16, № 3. С. 39–53.

Information, Control and Measurement Systems
Информационные, управляющие и измерительные системы

Research article
DOI: https://doi.org/10.18721/JCSTCS.16304
UDC 62.5

TESTING A HETEROGENEOUS GROUP OF AUTONOMOUS UNMANNED UNDERWATER VEHICLES FOR SEARCH OF OBJECTS ON THE BOTTOM

N.N. Semenov[1], *M.N. Chemodanov*[1], *I.V. Shestakov*[1], *D.B. Akhmetov*[2] ✉

[1] State Marine Technical University, St. Petersburg, Russian Federation;
[2] Peter the Great St. Petersburg Polytechnic University, St. Petersburg, Russian Federation

✉ akhmetov@spbstu.ru

Abstract. The results of model and in-situ tests of control algorithms providing coordinated movement of a group of heterogeneous underwater robots in an uncertain three-dimensional moving environment in order to search for sunken objects on the bottom are being considered in the paper. Autonomous optical navigation of each robot, simulating the use of SLAM algorithms based on side-scan sonar (SSSI), interaction of robots with each other by means of surface buoys or a hydroacoustic modem, transfer of the detected objects` coordinates between robots in the group, and building a digital bottom map in the memory of each robot are used. The proposed control algorithms can be used both in centralized and decentralized control. Simulation model and field experimental data, confirming the performance of the proposed algorithms and protocols, are presented. The developed algorithms can be used in the control systems of mobile robots for their group control in uncertain 3D environments.

Keywords: group control, robot, group of robots, control system, AUV, underwater mapping, optical navigation

Citation: Semenov N.N., Chemodanov M.N., Shestakov I.V., Akhmetov D.B. Testing a heterogeneous group of autonomous unmanned underwater vehicles for search of objects on the bottom. Computing, Telecommunications and Control, 2023, Vol. 16, No. 3, Pp. 39–53. DOI: 10.18721/JCSTCS.16304

Научная статья
DOI: https://doi.org/10.18721/JCSTCS.16304
УДК 62.5

ИСПОЛЬЗОВАНИЕ РАЗНОРОДНОЙ ГРУППЫ АВТОНОМНЫХ НЕОБИТАЕМЫХ ПОДВОДНЫХ АППАРАТОВ ДЛЯ ПОИСКА ОБЪЕКТОВ НА ДНЕ

Н.Н. Семенов[1], *М.Н. Чемоданов*[1],
И.В. Шестаков[1], *Д.Б. Ахметов*[2] ✉

[1] Санкт-Петербургский государственный морской технический университет, Санкт-Петербург, Российская Федерация;

[2] Санкт-Петербургский политехнический университет Петра Великого, Санкт-Петербург, Российская Федерация

✉ akhmetov@spbstu.ru

Аннотация. В статье рассматриваются результаты моделирования и натурных испытаний алгоритмов управления, обеспечивающих согласованное движение группы разнородных подводных роботов в неопределенной трехмерной подвижной среде с целью поиска затонувших объектов на дне. Автономная оптическая навигация каждого робота, имитирующая использование алгоритмов SLAM (одновременная локализация и построение карты) на основе гидролокатора бокового обзора (SSSI), взаимодействие роботов друг с другом посредством надводных буев или гидроакустического модема, передача координат обнаруженных объектов между роботами в группы и построения цифровой карты дна в памяти каждого робота. Предложенные алгоритмы управления могут использоваться как при централизованном, так и при децентрализованном управлении. Представлены имитационная модель и данные полевых экспериментов, подтверждающие работоспособность предложенных алгоритмов и протоколов. Разработанные алгоритмы могут быть использованы в системах управления мобильными роботами для их группового управления в неопределенных трехмерных средах.

Ключевые слова: групповое управление, робот, группа роботов, система управления, АНПА, подводная картография, оптическая навигация

Для цитирования: Semenov N.N., Chemodanov M.N., Shestakov I.V., Akhmetov D.B. Testing a heterogeneous group of autonomous unmanned underwater vehicles for search of objects on the bottom // Computing, Telecommunications and Control. 2023. Т. 16, № 3. С. 39–53. DOI: 10.18721/JCSTCS.16304

Introduction

Autonomous unmanned underwater vehicles (AUVs) are successfully used to perform search and monitoring tasks in various types of water areas, and the objectives can be different: searching for underwater objects in emergency situations, searching for sunken objects, demining the territory, searching for minerals or bioresources. When carrying out such works an important task is to increase their efficiency, reducing the time spent and, consequently, the cost [1]. At present, AUVs are traditionally used singly with cyclic repeated launches including surveying (photo, acoustic, electromagnetic, etc.), AUVs return to the "base", information readout, received information processing by specialists, planning subsequent launches in areas with refined coordinates [1].

It is necessary to use the AUV groups equipped with mutual positioning and communication systems simultaneously, so that AUVs do not interfere with each other during execution of the common task, to increase the efficiency of works. Transfer of information processing functions to the AUV and organization of decision-making system for changing group behavior, when detecting specified objects in the group, will make the group autonomous, not requiring constant control and management [1–12].

Taking into account that the AUVs can malfunction or be exposed to artificial obstacles during their tasks in deep waters, the group of AUVs should be stable to the change of number and inexpensive if possible. It is proposed to abandon universal AUVs in favor of specialized ones, each of which does their job well at minimal cost, to reduce costs. For example, some of the robots have greater autonomy, speed, and search facilities. The objects detected by these robots are surveyed by less numerous vehicles, but more expensive and better equipped for vision and classification, and in case of successful classification, specialized robots, capable of lifting to the surface the detected objects, are involved. An example of a group of such specialized AUVs is BLUEFIN [1].

Considering that AUVs are moved in mobile environment (the mobile in mobile), that there is no global positioning system as GPS under water, that local systems require time for deployment and have a lot of their limitations, the task of AUV independent positioning during any work under water is very actual, especially when working in a group. It is connected with both safety (so that AUVs do not interfere with work of other AUVs), and with efficiency of site survey by different AUVs. fdf

Thus, this paper examines the most functional AUVs and their capabilities for joint work at the same area, underwater robots developed at St Petersburg Marine Technical University (SMTU), describes a mathematical model of robots collaboration and positioning, proposes a model for studying the joint autonomous work by a group of AUVs developed by SMTU with positioning based on optical ArUco-tags [6] located on the bottom of the pool, the results of full-scale tests in the pool of such a system are presented.

The joint work of AUVs with the results of full-scale tests is a rare topic in scientific articles. Reviews of such articles have been discussed in detail at [10–12]. This work that describes the results of full-scale experiments on the absolute positioning of a group of heterogeneous AUVs is relevant and timely.

Overview of existing submarine group control projects

CoCoRo (Collective Cognitive Robotics).

This is the most famous of the research projects on the control of large groups of underwater robots [2], aimed at studying the algorithms and possibilities of the underwater robots interaction in a group. It is being funded by the European Union for more than 12 years, both the small robots themselves and the group control system for them have been developed. The core of the CoCoRo group consists of 20 relatively large Jeff robots with high maneuverability, autonomy up to several hours and capable of moving at a speed of 1 meter per second. The rest of the group's underwater robots belong to a different class, Lily, are smaller in size and speed and act as the “brain” of the collective intelligence “swarm” of robots. These robots provide communication and information transfer between Jeff robots, the base station and the rest of the surrounding world, and participate in making collective decisions. The third type of robot is a docking station for the first two types of robots.

Each robot in the CoCoRo group is able to act independently, performing its own task; to perform more complex tasks, robots are combined into small groups, but to perform global (for this group of robots) tasks the whole group is used, forming a “swarm” based on the available collective data. Using the “swarm” ideology, the group becomes versatile, adaptable to changing conditions, resistant to changes in the group composition.

One of the practical application scenarios for such “swarms” of underwater robots is underwater search operations. In this case, the Jeff robots will search directly, moving quickly in a variety of directions and constantly coordinating their actions. Once a target has been located, they will use the Lily robots to tell each other and relay that information to the surface.

The CoCoRo team has already been tested in natural bodies of water, lakes and rivers, showing its simplicity and effectiveness.

Bluefin Robotics. It is another popular project of underwater robots collective control [3]. The project has developed both the heterogeneous submersibles themselves and a group control system for them. To search for sunken objects it is proposed to use the most numerous group of BLUEFIN-9 vehicles, which

Fig. 1. Example of Lily group of robots

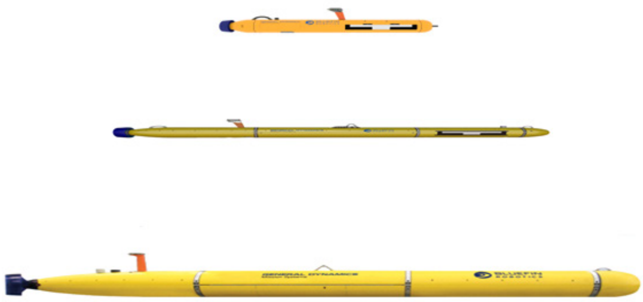

Fig. 2. Example of BLUEFIN-9, BLUEFIN-12 and BLUEFIN-21 AUVs

moves along the bottom, detects objects and transmits information to a less numerous group of BLUEFIN-12, which check and classify detected objects, determine their exact coordinates, then inform the smallest BLUEFIN-21 vehicles, which collect information, process and either decide on further actions themselves or send a message to a human by hydroacoustic or radio channel. Autonomy of such robots is 8–12 hours.

Kongsberg. It is actively advertised as very reliable and high quality multifunctional AUVs. It has good maneuverability, depth and speed according to open data. These are the "HUGIN" AUVs. [4]. They can be equipped with a wide range of additional equipment and can be used both autonomously and with remote control or under supervision. Autonomy is 24–74 hours, length is 5.2–6.4 m, external diameter – 0.75 m, weight – 1000–1500 kg, diving depth – up to 4500 m, speed – 2–6 knots.

The types of tasks solved by these AUVs both individually and as a group are not disclosed on the website, but the promotional videos include corrective search for sunken objects and monitoring the condition of pipelines.

ACOBAR (Acoustic Technology for Observing the interior of the Arctic Ocean). The task for the developers was to monitor the state of the marine environment in the Arctic Ocean. The complexity of the Arctic Ocean research is that the surface is almost always covered by ice, and the support vessel cannot constantly stay above the surface under study, so all submersibles are autonomous with great autonomy and accurate positioning system in ice conditions. Such vehicles include various underwater gliders, AUVs and autonomous surface boats.

Thus, the development and introduction of control systems for groups of submersibles is actively developing in the world. Such groups make it possible to perform search and monitoring work in large water areas much faster, more reliable and efficient than single robots, as well as to automatically take into account changes in operating conditions and changes in the group composition (failure or replenishment).

Fig. 3. Example of HUGIN AUV

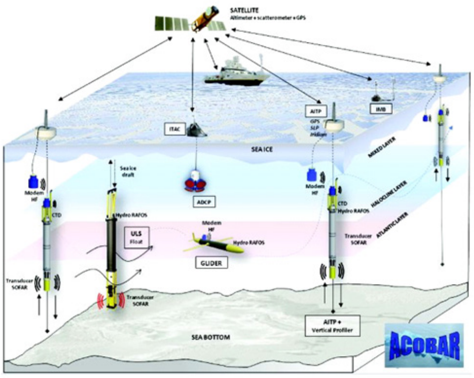

Fig. 4. Example of an ACOBAR monitoring system

But the CoCoRo project is devoted to the smallest AUVs with small autonomy and is intended for working out of interaction algorithms, while other considered projects are large deep-water AUVs with high autonomy and high price. It is necessary to develop and test a group of AUVs that can independently survey the bottom in the water area of several square kilometers, have onboard a video camera for search, communication and positioning system, as well as autonomy of not less than 4–6 hours.

Developed group of heterogeneous robots

The following AUVs were developed to solve the problem of bottom survey:

• "Akara" micro AUV. Working depth is up to 50 meters, hull diameter is 100 mm, length is about 1 m, maximum speed is 2.5 knots, weight is not more than 10 kg, which allows launching and receiving AUVs from hands, autonomy is not less than 2 hours and can be increased by additional compartments with batteries. Akara-M is an upgraded version developed as part of research work on the creation of a multi-agent sensor-communication network based on marine robotic platforms (MRP).

• "Goupi" micro AUV. This AUV is designed to teach schoolchildren the basics of underwater robotics. Hull diameter is smaller than that of Akara and is 70 mm, length is 750 mm, weight is 3 kg, autonomy is 2 hours, max speed is 2.5 knots, max depth is 50 m. Control system is built on Linux operating system, ROS, it contains 720HD high resolution video camera and inertial navigation system.

• "Trionix" ROV is a telecontrolled submersible vehicle of micro class with the overall dimensions of 450 × 340 × 140 mm, weight of 3.5 kg, cable length up to 20 m, 720HD video camera, roll, trim, temperature and depth sensors, LINUX operating system, ROS framework. The autonomy of such a robot is not limited, since power is supplied via control wires, but the range is limited by the cable length.

Collaborative robot operation

The task assigned to the group is to search for sunken objects in clear water. A radio channel is used for communication, a float with an antenna moves behind each robot for radio channel operation by an underwater robot. The robot group needs to be augmented with a positioning system to accomplish the task.

Fig. 5. “Akara” AUV

Fig. 6. “Akara-M” AUV

Since the robots have an inertial navigation system (INS) and a high resolution video camera, inertial navigation is used to tie the coordinates of the robots to ArUco tags located on the bottom, and inertial navigation is used between the tags [6].

Inertial navigation is based on processing signals from angular velocity sensors (gyroscopes) and acceleration sensors (accelerometers) along three spatial axes. The result of processing (time integration) of the gyroscope signal is the rotation angle of the robot. The accelerometers are only used to calculate the roll and trim angles, while the current speed and the distance traveled are determined by the control signals of the thrusters. In this case navigation errors occur [7–21].

For example, if we assume that the output of the gyro signal on each of the axes contains a useful signal and noise component (which is 1...2 low-order bits of ADC), then during integration we get the following angle:

$$\alpha(T) = \int_0^T \left(\omega(t) + n(t)\right) dt = \int_0^T \omega(t)\, dt + \int_0^T n(t)\, dt = A(T) = N(T) + C,$$

where $\alpha(T)$ is the rotation angle, $\omega(T)$ is the angular velocity, $n(T)$ is the noise, $A(T)$ is the true rotation angle, $N(T)$ is the noise integral and as a consequence the angle error, C is the initial angle setting.

Thus, the resulting angle is the sum of the time integral of angular velocity and the time integral of noise. When the angular velocity measurement has an asymmetric error with respect to zero and noise (and in practice, absolute symmetry is technically impossible), the noises begin to give an increasing error $N(T)$ with time at the current angle of rotation $\alpha(T)$.

Similarly, with the accelerometer error accumulation at double integration, the error starts to grow with time even if the gravity acceleration is cut out correctly:

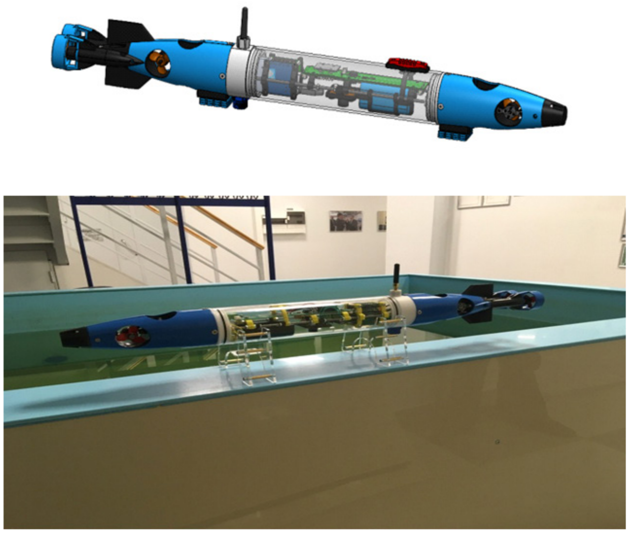

Fig. 7. “Goupi” AUV

$$x(T)=\int_0^T\int_0^T \big(a(t)+n(t)\big)\,dtdt=$$
$$=\int_0^T\int_0^T a(t)\,dtdt+\int_0^T\int_0^T n(t)\,dtdt = X(T)+N(T)+(V+Nv)*T+X_0,$$

where $x(T)$ is the current coordinate, $a(t)$ is acceleration from the accelerometer, $n(t)$ is accelerometer noise, $X(T)$ is the true coordinate, $N(T)$ is the double integral of accelerometer noise, V is the initial speed, Nv is the constant component of the first integral of time noise, X_0 is the initial displacement.

The typical inertial module (MPU-9250) consists of three independent uniaxial vibrational angular velocity sensors (gyroscope MEMS) that respond to rotation around the X-, Y-, Z-axes. Two suspended masses perform oscillations on opposite axes. With the appearance of angular velocity, the Coriolis effect causes a change in vibration direction $\overrightarrow{F_k}=-2m\cdot\left[\vec{\omega}\times\overrightarrow{v_r}\right]$, which is detected by a capacitive sensor [22–30]. The measured differential capacitive component is proportional to the displacement angle [26–30]. The resulting signal is amplified, demodulated, and filtered, yielding a voltage proportional to angular velocity. This signal is digitized with a 16-bit ADC built into the board. The samplerate can be programmed from 3.9 to 8000 samples per second (SPS) and user configurable LPFs (low-pass filters) provide a wide range of possible cutoff frequencies. The LPF reduces the variance of each measurement, but does not compensate for the static error.

Thus, with a 16-bit gyro the amount of error is one low bit. If the total angular velocity amplitude is 300 degrees per second, the error will be on the order of 0.0045 degrees per second, and when accumulated over 100 seconds, the angle error will be 0.45 degrees, increasing linearly with time. Using a larger ADC and reducing noise will reduce this error, but the error will still increase over time.

Additionally, the gyroscope readings are affected by the rotation of the Earth, which leads to a predictable error of the gyroscope readings for one minute as $\Delta\alpha = 360/24/60 \times \sin(\varphi)$, where φ is the latitude of the place. For example, at the latitude of the city of Sochi, this error would be 0.17 degrees per minute. Such an error can be predicted and compensated programmatically during tests.

Position error accumulates even faster: for example, at full 3G ADC amplitude and 16-bit resolution, the error can be $\pm$ $4.5e^{-4}$ м/s^2. This small amount of error results in an error of 4.5 meters in 100 seconds. The use of the counting method, i.e., predicting its own motion from the signals received by the marching and steering engines and thrusters, also contains an uncompensated cumulative error, which depends on

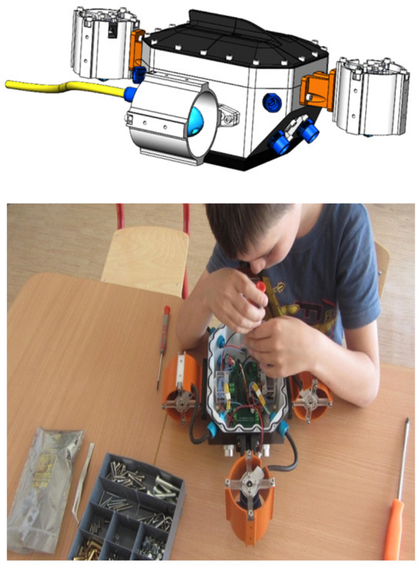

Fig. 8. “Trionix” ROV

the hydrodynamics of the submersible hull, but can be used as one of the methods for determining the distance traveled.

Errors in the inertial system and the counting method are cumulative, and can only be eliminated by referencing to absolute coordinates.

Autonomous non inertial referencing of AUV (by external environment parameters measuring means) can be carried out by absolute and relative coordinates. Relative coordinates are velocity readings relative to water that do not take into account currents and internal waves, so such coordinates contain uncompensated error and cannot be used for long-term navigation. Absolute coordinates are the binding of current AUV position to the position on the map relative to absolute reference points located on the bottom and marked on the map. Such coordinates do not contain error that accumulates over time and can be used for long-term navigation. If reference marks are unambiguously detectable and marked on the map, this problem has been solved long ago and is used by surveyors. But if both landmarks and map are missing, the SLAM (simultaneous localization and mapping) technology can be used for positioning. It is a technology (a set of algorithms) where each robot moves relative to the stationary bottom (for AUV), detects “special points” on the bottom, classifies them and records on the map. Thus, moving along the bottom, a map is constructed, which can be transferred to other AUVs, and can be used for own positioning during the next passage of the surveyed area [6].

Thus, absolute positioning without a predetermined map consists of the following stages:

1. Detecting “special points” on the bottom
2. Identifying “singularities” for further use
3. Classification for mapping
4. Re-detection and positioning

Only sonar gives maximum detection range in water, among sonars maximum resolution and coverage area is given by SSS (side scan sonar), so SSS signals are the most promising for SLAM task.

But it is inexpedient to use SSS when testing AUV in the pool – the walls in the pool are flat and smooth, the acoustic signal has nothing to be reflected from. That is why it is suggested to replace the picture, obtained by SSS when passing over the bottom section, with the image from the video camera, located under the ANPA bottom. The image structure is comparable and suitable for the task of interaction algorithms testing.

The usage of contrasting flat black and white marks lying on the bottom is proposed in order to simplify the task of detection, determination of "features" and classification. Such markers will be detected from any direction, the shape of the pattern on the marker is unique for each marker, so the "features" detection and classification of such markers is a solved problem. The most popular markers for computer vision systems are ArUco markers [6].

The use of ArUco markers allows to imitate inhomogeneities on the bottom and simplify their identification. Such codes are placed either at pre-known coordinates or randomly placed on the bottom, then detected by video cameras of robots and allow to determine and correct their own position relative to the codes. The detection accuracy depends on the resolution of the video camera matrix and the distance from the video camera to the code:

$$\delta x = \frac{r\Delta\varphi}{N},$$

where r is the distance to the bottom, $\Delta\varphi$ is the angular solution of the video camera, N is the number of points in the image for a given dimension.

This error is absolute and does not accumulate over time.

The number and location of such tags is chosen so that for the time of tracking from one tag to another, the robot, when using an inertial system, is brought down to a distance no greater than the width of the bottom inspection by the video camera.

The following options for using the tags:

• When there are many random heterogeneities on the bottom, the very shape of their location is an identifying feature, and then the whole space on the bottom under the AUV can be conditionally divided into a rectangular grid, each cell of which is a label on the map with its parameters and features. It is proposed to set ArUco marks in the nodes of orthogonal grid nodes to model the situation.

• Where the bottom itself is sufficiently uniform, and it is possible to detect individual sparsely located heterogeneities, which cannot be seen several at once in one frame, we have to detect, determine the “features” and classify each such heterogeneity separately. And then the map will have separate randomly located marks, which can be modeled by random arrangement of ArUco tags.

• Another variant of tag arrangement is the random arrangement of repeating or closely shaped heterogeneities that cannot be unambiguously classified individually. But if we analyze the sequence of passing tags, the probability of correct classification and positioning is significantly higher. It is proposed to use randomly arranged repetitive ArUco tags to simulate the situation.

Arrangement of the ArUco tags in the orthogonal grid nodes

An orthogonal grid is placed on the bottom of the reservoir, at the nodes of which the tags are located. The distance between the tags is chosen so that during the time of movement from one tag to another the error of position according to the inertial and counting method does not exceed half the distance between the tags, and the camera found the tag, having corrected its own position. An example of such a grid is shown in the Fig. 9.

Scenario of the robot group`s work:

• robots are assigned an area of work (part of the water area) in advance;

• robots are unleashed at a predetermined location, where they can find their own position and course using a marker on the bottom;

• after launching, the robots start moving towards the pre-set area and survey it if they find an object they are looking for on the bottom, they determine its coordinates, surface and report to the processing center.

An example of the trajectories of two robots obtained from the model is shown in the following Fig. 10.

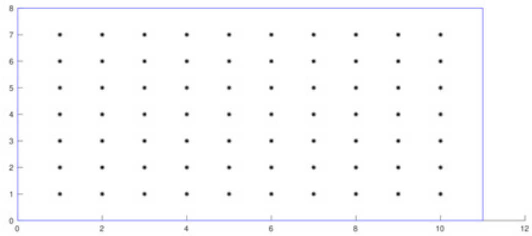

Fig. 9. Example of an orthogonal grid of ArUco tags

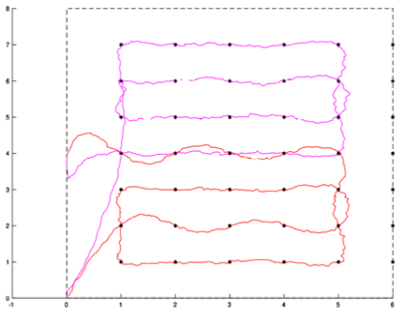

Fig. 10. Example trajectories of robots moving along the nodes of an orthogonal grid over ArUco tags

The figure shows that the robots correct their position according to the data from the tags, but the presence of inertia and errors of inertial navigation and counting leads to a curvilinear movement trajectory of movement. But with the current location of the tags, there is enough accuracy not to go off the set trajectory of the bottom survey. The number of points and the maximum distance between them is determined by the range of vision of the robot video cameras and the distance from the robot to the bottom so that the robot could not pass between the tags and not see a single one.

Random arrangement of the ArUco tags

With randomly positioned tags, only the position of the starting mark is set, by which the robots determine the initial position and course, and the remaining tags can only be used to refine their own position when redetected. For this purpose, SLAM (simultaneous localization and mapping) – the method used to build a map in an unknown space or to update the map in a known space with simultaneous control of the current location and traveled distance – is applied. Popular methods of approximate solution to this problem are particle filter and extended Kalman filter. Such particles will be ArUco tags. The SLAM problem is to compute an estimate of the agent's location x_t and the environmental map m_t from a series of observations ot over a discrete time with sampling step t. All the listed quantities are probabilistic. The goal of the problem is to compute the maximum posterior probability of being at point x_t on map m_t when observing a series ot $o_t : P\left(m_t, x_t \middle| o_{\{1:t\}}\right)$. Applying Bayes' rule is the basis for updating the posterior location sequentially:

$$P\left(x_t \middle| a_t, m_t\right) = \sum\nolimits_{m(t-1)} P\left(o_t \middle| x_t, m_t\right) \sum\nolimits_{x(t-1)} P\left(x_t \middle| x_{(t-1)}\right) P\left(x_{(t-1)} \middle| m_t, o_{(1:t-1)}\right) \Big/ Z .$$

Similarly, the map can be updated sequentially:

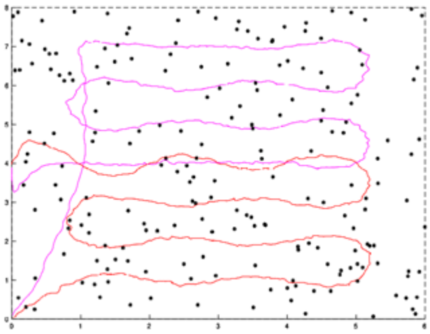

Fig. 11. An example of the trajectory of robots moving on randomly placed tags

$$P\left(m_t \middle| x_t, m_t\right) = \sum_{x_t} \sum_{m_t} P\left(m_t \middle| x_t, m_{(t-1)}, o_t\right) P\left(m_{(t-1)}, x_t \middle| o_{(1:t-1)}, m_{(t-1)}\right).$$

It is possible to arrive at a local optimal solution by applying the EM algorithm, while operating with two probabilistic variables, as is the case in many other problems of logical inference.

An example of robot trajectories positioned by randomly arranged Arcso-tags is shown in the Fig. 11.

Fig. 11 shows that when the tags are randomly placed, there are areas where it is impossible to determine the absolute position from the tags. The trajectory must be such that with each next tack a portion of the tags that were visible during the last pass is captured, but in places where there are not enough tags, there are failures. Therefore, in order to successfully navigate a group of robots with a random arrangement of tags, it is necessary to provide a significantly higher number of tags on the bottom than in the orthogonal arrangement in the grid nodes.

Using repeating or similar tags for positioning

When using heterogeneities as tags, there is an ambiguity in the classification of such heterogeneities due to the fact that, unlike uniquely structured ArUco tags, where each tag can be identified, heterogeneities are simply protrusions or pits on the bottom. Depending on the angle of observation, these inhomogeneities may have different shapes, create different shadows, and merge with other inhomogeneities. But if we solve the problem of classification of such heterogeneities or artificially simplify it (create heterogeneities of known classes, for example, by the number of vertices), then the positioning problem is reduced to the previous one – by a random set of tags. But such tags will not be unique, i.e. repetitive.

Therefore, it is desirable to limit the number of types of randomly placed tags for modeling. But then for unambiguous positioning of robots on their routes it is necessary to arrange tags so that the positioning is unambiguous, that is, on the next tack robots should see some of the tags that were on the previous tack from the next one. An example of this arrangement is shown in Fig. 12.

Thus, positioning by random heterogeneities has its own difficulties, but they can be solved for each specific case, including basin tests.

Conducting full-scale tests of the AUV group

A pool with transparent water was used for full-scale tests, ArUco tags were placed at the bottom of the pool, and the task of underwater robots was to search for a bright red object on the bottom using a video camera located on the AUV. The AUV positioning was based only on the information from those ArUco tags and the inertial navigation system.

An example of one AUV position during the search of a sunken object on the bottom is shown in Fig. 13.

According to the results of numerous experiments, it was shown that the AUV successfully detects the tags lying on the bottom, determines its position, corrects its trajectory, and not a single case of trajectory

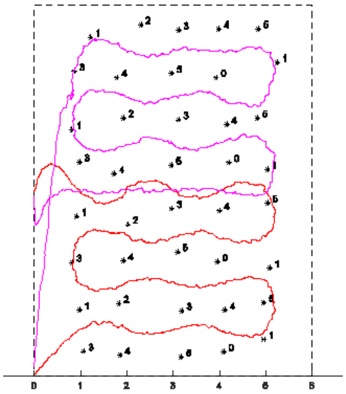

Fig. 12. Example location of heterogeneities for unambiguous positioning

Fig. 13. Example of AUV position when moving “in a loop” during a site survey

failure was detected. The sunken object was detected in 100% of experiments. The frequency of tag placement was determined by the pool depth, the width of the AUV camera view, and the trajectory shape - at least one tag should be visible in each corner of the trajectory. The size of the pool is 4×2 meters, depth is 0.5 meters. AUV movement speed is 0.2 m/s.

When several heterogeneous robots (AUVs and ROVs) were in the pool simultaneously, the navigation also showed its reliability – the robots did not interfere with each other, successfully positioned themselves and compensated for the turbulent flows that they created for each other in the limited volume of water. An example of the mutual positioning of the robots during the tests is shown in the Fig. 14.

Each AUV has a trajectory laid down to capture some of the tags that were visible during the last pass, but there are failures in places where there are not enough tags. Therefore, for successful navigation of a group of robots with random arrangement of tags, it is necessary to provide their significantly greater number on the bottom than with orthogonal arrangement in grid nodes, and trajectories of each AUV are formed so as to reduce the number of possible crossings and parallel tack.

According to the results of the conducted experiments, the whole group successfully inspected the bottom of the pool and detected the object of interest, which confirms the correctness of the implemented algorithms and mathematical models.

Conclusions

The main projects of controlling groups of underwater vehicles were considered, their advantages and disadvantages were analyzed, a group of heterogeneous underwater vehicles developed at SPbGMTU was described, an algorithm for search of sunken objects on the bottom with positioning by ArUco-tagging was

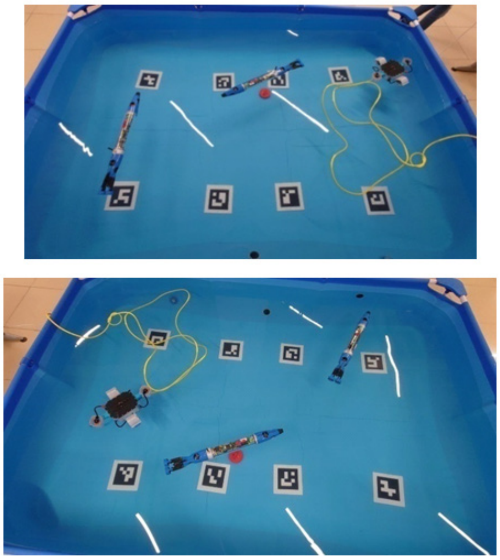

Fig. 14. Examples of simultaneous operation of several robots in a limited water area

proposed during the work. Optical navigation simulating absolute lag, inertial navigation system, communication between robots, transfer of coordinates of detected objects and construction of the bottom map are used.

Model and field tests of control algorithms providing coordinated movement of a group of robots in an uncertain three-dimensional moving environment with possible obstacles to search for sunken objects on the bottom were conducted.

The proposed algorithms can be used for both centralized and decentralized control, which allows using the group as a single telecontrolled object or as an autonomous group performing work without human control.

Model and experimental data confirming the performance of the proposed algorithms and protocols are presented. The developed algorithms can be used in the control systems of mobile robots for their group control in uncertain 3D environments.

REFERENCES

1. **Ahn J., Syed A., Krishnamachari B., Heidemann J.** Design and analysis of a propagation delay tolerant ALOHA protocol for underwater networks. Ad Hoc Networks, 2011, vol. 9, pp. 752–766. DOI: https://doi.org/10.1016/j.adhoc.2010.09.007

2. **Brekhovskikh L.M., Lysanov Yu.P.** Fundamentals of Ocean Acoustics. Third Edition. Springer, 2003.

3. **Bresciani M., Ruscio F., Tani S., Peralta G., Timperi A., Guerrero-Font E., Bonin-Font F., Caiti A., Costanzi R.** Path Planning for Underwater Information Gathering Based on Genetic Algorithms and Data Stochastic Models. J. Mar. Sci. Eng. 2021, vol. 9, p. 1183. DOI: https://doi.org/10.3390/jmse9111183

4. **Carreras M., Candela C., Ribas D., Palomeras N., Magií L., Mallios A., Vidal E., Pairet È., Ridao P.** (2018) Testing SPARUS II AUV, an Open Platform for Industrial, Scientific and Academic Applications. CoRR. 2018. URL: https://arxiv.org/abs/1811.03494 (accessed: Feb. 10, 2022).

5. **Crout R.L., Conlee D.T., and Bernard L.J.** National Data Buoy Center (NDBC) National Backbone Contributions to the Integrated Ocean Observation System (IOOS). In: OCEANS , 2006, pp. 1–3. DOI: https://doi.org/10.1109/OCEANS.2006.30.307073

6. **Dinc M., Hajiyev C.** Integration of navigation systems for autonomous underwater vehicles. Journal of Marine Engineering & Technology, 2015, vol. 14, no. 1, pp. 32–43. DOI: 10.1080/20464177.2015.1022382

7. **Encarnaçao P., Pascoal A.** Combined trajectory tracking and path following: An application to the coordinated control of autonomous marine craft. In Proceedings of the 40th IEEE Conference on Decision and Control, IEEE, Orlando, USA, 2001,vol. 1, pp. 964–969. DOI: 10.1109/CDC.2001.980234

8. **Furlong M.E., Paxton D., Stevenson P., Pebody M., McPhail S.D., Perrett J.** Autosub long range: A long range deep diving AUV for ocean monitoring. In Proceedings of the 2012 IEEE/OES Autonomous Underwater Vehicles (AUV), Southampton, UK, 24–27 September 2012, pp. 1–7. [Google Scholar]

9. **Kinsey J.C., Eustice R.M., Whitcomb L.L.** A survey of underwater vehicle navigation: Recent advances and new challenges. In Proceedings of IFAC Conference of Manoeuvring and Control of Marine Craft, IFAC, Lisbon, Portugal, 2006, vol. 88, pp. 1–12.

10. **Kozhemyakin I.V., Rozhdestvensky K.V., Ryzhov V.A., Semenov N.N., Chemodanov M.N.** (2016a). Educational Marine Robotics in SMTU. 79–88. DOI: 10.1007/978-3-319-43955-6_11

11. **Kozhemyakin I.V., Putintsev I.A., Semenov N.N., Chemodanov M.N.** Development of underwater robotic system, using open-source simulation model extended by hydroacoustic interaction. Izvestiya SFedU. Engineering sciences, 2016, vol. 1(174), pp. 88–102. (in Russ)

12. **Kozhemyakin I.V., Putintsev I.A., Semenov N.N., Chemodanov M.N.** The Model of Autonomous Unmanned Underwater Vehicles Interaction for Collaborative Missions: Third International Conference, ICR 2018, Leipzig, Germany, September 18–22, 2018, Proceedings. DOI: 10.1007/978-3-319-99582-3_15

13. **Lan H., Lv Y., Jin J., Li J., Sun D., Yang Z.** Acoustical Observation with Multiple Wave Gliders for Internet of Underwater Things. IEEE Internet of Things Journal, 2021, vol. 8, iss. 4, pp. 2814–2825. https://doi.org/10.1109/JIOT.2020.3020862

14. **Leonard J.J., Bahr A.** Autonomous underwater vehicle navigation. In Springer Handbook of Ocean Engineering, M.R. Dhanak, N.I. Xiros, Eds., Cham, Germany: Springer, 2016, pp. 341–358. DOI: 10.1007/978-3-319-16649-0_14

15. **Lin Y., Guo J., Li H., Zhu H., Huang H., Chen Y.** (2022) Study on the Motion Stability of the Autonomous Underwater Helicopter. J. Mar. Sci. Eng. 2022, 10, 60. DOI: https://doi.org/10.3390/jmse10010060

16. **Miao J., Deng K., Zhang W., Gong X., Lyu J., Ren L.** Robust Path-Following Control of Under actuated AUVs with Multiple Uncertainties in the Vertical Plane. J. Mar. Sci. Eng. 2022, vol. 10, p. 238. DOI: https://doi.org/10.3390/jmse10020238

17. **Oke P., Sakov P.** Assessing the footprint of a regional ocean observing system. Journal of Marine Systems, 2012, vol. 105, pp. 30–51. DOI: https://doi.org/10.1016/j.jmarsys.2012.05.009

18. **Ovchinnikov K.D., Ryzhov V.A., Sinishin A.A., Kozhemyakin I.V.** Experimental study of running characteristics of wave glider. Proceedings of XV All-Russian Scientific and Practical Conference "Advanced systems and control problems", Southern Federal University Press, 2020, pp. 91–97.

19. **Płaskonka J.** Different kinematic path following control-lers for a wheeled mobile robot of (2,0) Type. Journal of Intelligent and Robot Systems, 2015, vol. 77, no. 3–4, pp. 481–498. DOI: https://doi.org/10.1007/s10846-013-9879-6

20. **Popović M., Vidal-Calleja T., Chung J.J., Nieto J., Siegwart R.** Informative Path Planning for Active Field Mapping under Localization Uncertainty. In Proceedings of the 2020 IEEE International Conference on Robotics and Automation (ICRA), Xi'an, China, 31 October 2020, pp. 10751–10757. [Google Scholar]

21. **Ryabinin V, Barbière J, Haugan P, at al.** The UN Decade of Ocean Science for Sustainable Development. In Oceanobs'19: An Ocean of Opportunity, 2019. DOI: https://doi.org/10.3389/fmars.2019.00470

22. **Sahu B.K., Subudhi B., Gupta M.M.** Stability analysisof an underactuated autonomous underwater vehicle using extended – Routh's stability method. International Journal of Automation and Computing, 2018, vol. 15, no. 3, pp. 299–309. DOI: 10.1007/s11633-016-0992-4

23. **Sheehy M.T., Halley R.** Measurement of the Attenuation of Low-Frequency Sound. J. Acoust. Soc. Amer, 1957, vol. 29, no. 4, pp. 464–469. DOI: https://doi.org/10.1121/1.1908930

24. **Shivgan R., Dong Z.** Energy-Efficient Drone Coverage Path Planning using Genetic Algorithm. In Proceedings of the 2020 IEEE 21st International Conference on High Performance Switching and Routing (HPSR), Newark, NJ, USA, 11–14 May 2020, pp. 1–6. [Google Scholar]

25. **Soetanto D., Lapierre L., Pascoal A.** Adaptive, non-singular path-following control of dynamic wheeled robots. In Proceedings of the 42nd IEEE International Conference on Decision and Control, IEEE, Maui, USA, 2003, vol. 2, pp. 1765–1770. DOI: 10.1109/CDC.2003.1272868

26. **Su X., Ullah I., Liu X., Choi D.** A Review of Underwater Localization Techniques, Algorithms, and Challenges. Journal of Sensors, 2020, Article ID 6403161, 24 p. DOI: https://doi.org/10.1155/2020/6403161

27. **Su Y Zhang L., Li Y., Yao X.** A Glider-Assist Routing Protocol for Underwater Acoustic Networks with Trajectory Prediction Methods. IEEE Access, 2020, vol. 8, 154560–154572. DOI: https://doi.org/10.1109/ACCESS.2020.3015856

28. **Urik R.J.** Principles of underwater sound for engineers. N.Y.-London-Toronto-Sydney, 1967.

29. **Williams S.B., Pizarro O.R., Jakuba M.V., Johnson C.R., Barrett N.S., Babcock R.C., Kendrick G.A., Steinberg P.D., Heyward A.J., Doherty P.J., et al.** Monitoring of benthic reference sites: Using an autonomous underwater vehicle. IEEE Robot. Autom. Mag. 2012, vol. 19, pp. 73–84. [Google Scholar]

30. **Zhou R., Chen J., Tan W., Cai C.** Sensor Selection for Optimal Target localization with 3-D Angle of Arrival Estimation in Underwater Wireless Sensor Networks. J. Mar. Sci. Eng. 2022, vol. 10, p. 245. DOI: https://doi.org/10.3390/jmse10020245

INFORMATION ABOUT AUTHORS / СВЕДЕНИЯ ОБ АВТОРАХ

Semenov Nikolay N.
Семенов Николай Николаевич
E-mail: semenov@smtu.ru
ORCID: https://orcid.org/0000-0003-3112-4607

Chemodanov Mikhail M.
Чемоданов Михаил Николаевич
E-mail: mikhail.chemodanov@gmail.com

Shestakov Ivan V.
Шестаков Иван Владимирович
E-mail: vanyww2@gmail.com
ORCID: https://orcid.org/0009-0002-8919-3496

Akhmetov Denis B.
Ахметов Денис Булатович
E-mail: akhmetov@spbstu.ru

Submitted: 02.08.2023; Approved: 29.09.2023; Accepted: 11.10.2023.
Поступила: 02.08.2023; Одобрена: 29.09.2023; Принята: 11.10.2023.

Computing, Telecommunication and Control, 2023, Vol. 16, No. 3, Pp. 54–63.
Информатика, телекоммуникации и управление. 2023. Том 16, № 3. С. 54–63.

Intellectual Systems and Technologies
Интеллектуальные системы и технологии

Research article
DOI: https://doi.org/10.18721/JCSTCS.16305
UDC 004

ANALYSIS OF PERSONALITY TRAITS BASED ON THE DISC MODEL USING MACHINE LEARNING METHODS

L.P. Mbele Ossiyi ✉ , *P.D. Drobintsev*

Peter the Great St. Petersburg Polytechnic University,
St. Petersburg, Russian Federation

✉ lucprucell@gmail.com

Abstract. The analysis of a person's social media behavior with respect to privacy and human rights provides information about their personality traits and is seen as a topical task today. In areas such as marketing, training, education, human resource management and hiring policies in companies, knowledge about personality traits proves to be profitable and important in decision making and business orientation cases. The paper analyzes the performance of machine learning methods in a personality trait identification task based on the DISC psychological model and a small size dataset created from scratch. Although the dataset created was relatively small, the machine learning methods used showed encouraging and convincing results. Results for all personality trait classifiers were improved using hyperparameter optimization, increasing the performance of the XGBoost classifier to 70.45% on the accuracy metric in the test sets.

Keywords: DISC model, personality traits, data pre-processing, machine learning, TF-IDF, XGBoost

Citation: Mbele Ossiyi L.P., Drobintsev P.D. Analysis of personality traits based on the disc model using machine learning methods. Computing, Telecommunications and Control, 2023, Vol. 16, No. 3, Pp. 54–63. DOI: 10.18721/JCSTCS.16305

Научная статья
DOI: https://doi.org/10.18721/JCSTCS.16305
УДК 004

АНАЛИЗ ЛИЧНОСТНЫХ ЧЕРТ НА ОСНОВЕ МОДЕЛИ DISC С ИСПОЛЬЗОВАНИЕМ МЕТОДОВ МАШИННОГО ОБУЧЕНИЯ

Л.П. Мбеле Оссийи ✉ , *П.Д. Дробинцев*

Санкт-Петербургский политехнический университет Петра Великого,
Санкт-Петербург, Российская Федерация

✉ lucprucell@gmail.com

Аннотация. Анализ поведения человека в социальных сетях с соблюдением конфиденциальности и прав человека позволяет получить информацию о его личностных чертах и рассматривается на сегодняшний день как актуальная задача. В таких сферах как маркетинг, профессиональная подготовка, образование, управление человеческими ресурсами и политика найма в компаниях, знание о личностных чертах оказывается прибыльным и важным в случаях принятия решений и ориентации на бизнес. Статья посвящена анализу производительности методов машинного обучения в задаче идентификации личностных черт на основе психологической модели DISC и созданного с нуля набора данных небольшого размера. Хотя созданный набор данных был относительно небольшого размера, используемые методы машинного обучения показали обнадеживающие и убедительные результаты. Результаты, полученные всеми классификаторами по всем чертам личности, были улучшены с применением оптимизации гиперпараметров, что позволило увеличить производительность классификатора XGBoost до 70,45% по метрике accuracy в тестовых наборах.

Ключевые слова: модель DISC, личностные черты, предварительная обработка данных, машинное обучение, TF-IDF, XGBoost

Для цитирования: Mbele Ossiyi L.P., Drobintsev P.D. Analysis of personality traits based on the disc model using machine learning methods // Computing, Telecommunications and Control. 2023. Т. 16, № 3. С. 54–63. DOI: 10.18721/JCSTCS.16305

Introduction

The last two decades have witnessed massive use of digital platforms for sharing ideas, feelings, opinions and emotions, and X (former Twitter which is banned in Russia Federation) is one of the most widely used platforms in this context. Automatic identification of users' personality traits based on publicly available information from online social platforms is increasingly becoming a promising field these days and attracts widespread interest in various disciplines [1, 2]. As of today, automatic identification of personality traits is likely to become beneficial in many areas, such as recommendation systems, attribution of authorship, implementation of recruitment policies. Such applications are mainly built based on psychological models such as MBTI, Big Five, DISC and usually require large datasets, machine and deep learning algorithms. The size of a dataset is an important component in determining the performance of a machine-learning model. Large datasets generally lead to better performance on the classification problem. Nevertheless, it is stated that, large datasets in personality traits identification tasks are mostly created in English language and it is quite difficult to find a dataset for a specific language, which may lead to use of small dataset. In machine learning, a small dataset usually refers to a dataset containing less than 1000 instances while calculations and mathematical computations on it can be performed on a computer in a short time. Such a dataset is considered small because it may not be representative of the population. Some previous works have been devoted to the identification of personality traits based on the psychological models Big Five [3], DISC [4, 5] and MBTI [6]. However, the existing datasets used in these papers are mostly outdated, in English and unbalanced, making it difficult to make assumptions about different languages. An unbalanced dataset is one in which samples and their corresponding labels are not evenly distributed over the data space [7]. The unbalanced data distribution problem occurs when majority classes have a larger proportion of features than minority classes.

To address this problem, a balanced dataset of small size, in French, based on the DISC psychological model was created and the results and performance of machine learning algorithms on this dataset were analyzed.

In this paper, a dataset in French language was used, which is less difficult and different for instance from Russian language from a linguistic point of view (Cyrillic and Latin alphabet). Russian language, like other Slavic languages is a morphologically rich language with free order and inflection. These linguistic factors make it difficult to collect enough relevant features data to efficiently train machine-learning models, which could produce lower quality results compared to French ones.

The choice of the DISC model is explained by its ability to be a predictor of improved manageability in work teams (enterprises, organizations) [8]. Thus, the present paper aims to analyze machine-learning methods performance on a balanced small dataset in the task of personality traits identification based on the DISC psychological model.

Problem statement

To achieve our objective, this paper is organized as follows:

1. the dataset creation in French and data annotation;
2. data pre-processing;
3. application of different machine learning algorithms and analysis of their performance.

The social network Twitter (Twitter API) [9] was used to collect user-related data in this work. The data (tweets) were collected from January to May 2022 in French.

The psychological model used within the work is DISC. Personality traits were divided into four classes: *dominance, influence, steadiness, consciousness*.

As a result, data were collected on 660 users and more than 144,117 tweets. The corpus was divided into training and test samples in the 80/20 ratio.

The next steps after data collection were cleaning the dataset, its preprocessing and annotation, which was made possible largely by contacting an online service specializing in data annotation.

The following technology stack was used to implement the algorithms: Python 3.9 programming language; NumPy, Matplotlib, SciPy libraries; Google Colab development environment.

Stages of work

In this paper, our main concern was focused on user privacy in the process of collecting and analyzing data from Twitter accounts. The main challenge was to respect the boundary between public and private information. Anonymity of user data was protected by replacing usernames with some codes. Sensitive data, such as age, gender or civil identity of users were neither published nor used in the selection, classification, and other processes in this work.

a) Dataset creation

During the dataset creation process, the following were used: Twitter API, keywords. To obtain relevant data from users, keywords related to emotion, derived from Watson and Tellegen two-dimensional emotion map (1985) were selected. The Tellegen-Watson model (Fig. 1) is useful for linking spatial and discrete levels of emotions [10].

The dotted lines are the upper-level dimensions. The dimensions of positive effect and negative effect are shown as solid lines from the middle of the hierarchy and provide the heuristics needed to distinguish specific words with discrete emotions based on function. Discrete emotions near the axis correlate strongly with this dimension [10].

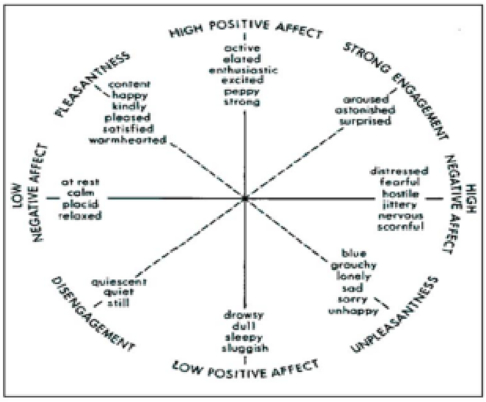

Fig. 1. Two-dimensional map of emotion by Wilson and Tellegen

To analyze the personality traits of individuals and build up a clean dataset consisting only of personal and real accounts, it was essential during the collection process for a better analysis to delete tweets containing languages other than French in their structure and to detect and remove bots and typical accounts such as: fanatical (sport, music), poetry and thoughts ones. During the filtering process several numerical characteristics were considered, such as the number of followed people, the number of friends, the frequency of posted tweets, the frequency of retweets, the frequency of comments and replies, and the age of the account (when the account was created). These characteristics were used by the Support Vector Machine algorithm during the training phase to proceed a binary classification to distinguish real accounts from others. The Support Vector Machine algorithm fitted well for this task due to its ability to handle high-dimensional data. A high value for metrics such as the precision and accuracy of an account indicated a high probability of a non-personal or fake account. For example, sports-related accounts have the particularity of having most of the tweets containing images, videos (taken from other sports-related accounts) with high frequency of replies and retweeting all sporting events with high frequency. As a result, **660** users and **144,117** tweets were obtained as material for work. To ensure work productivity, it was crucial to call on experts in the psychological field to annotate the dataset. The personality traits of the users were assessed by a panel of psychology experts on Fiverr.com. The Fiverr choice as a freelance platform for searching psychological experts is explained by its wide range of services and opportunities for finding services easily. To annotate the dataset, we opted for the choice of several psychological experts to compare the different results and judge their similarity. Psychological experts were chosen based on several criteria such as: their grades, their levels (diplomas and certificates, as Fiverr has a verification process during which sellers provide information about their training and background), and comments from other buyers. To determine user personality traits, each user was labelled with their most frequently used choice of words that fit the model.

Fig. 2 identifies the proportions of personality types: I (influence), D (dominance), C (conscientiousness) and S (steadiness). It is observed that personality types I and D are possessed by most users, and type S by a minority. The annotation work resulted in the following dataset (Fig. 3).

b) Data pre-processing

The obtained data is unstructured (Fig. 4), that is, it contains text, special characters, images, and videos. Hence, some pre-processing steps are required for further processing (Fig. 5) such as: converting all tweets to lowercase to create consistent text; removing stop words such as le, un; removing URLs, emoticons and special characters used in tweets; applying tokenization and lemmatization. Although users can use emoticons in a post to express their feelings and to provide relevant information, however in our case the analysis of users' posts in our dataset showed a low frequency of emoticon used per post, or even per user, consequently in our work we opted to remove them completely for consistency in our analysis.

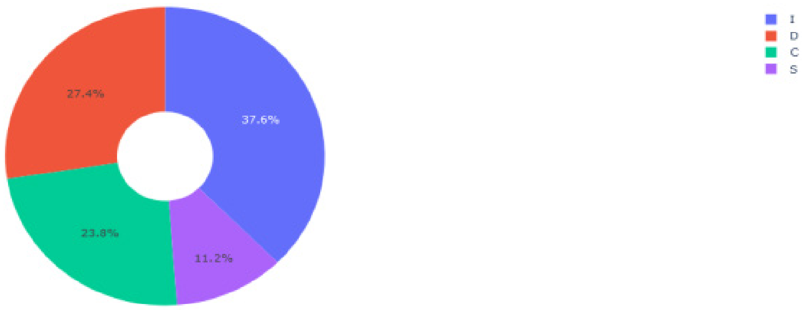

Fig. 2. Percentage of users by traits

Dataframe avec 660 fichiers et 7 colonnes

	namecode	tweets	D	I	S	C	trait
0	cc4de35c353ea3c42fd19afc559669e1	laksa chef heureux centre pailou rue dixon mei...	28.2	28.2	29.4	30.6	C
1	7e3695f6b6fc8252e27e346d78dd89e1	c l espoir soeur sophie mignon 100 x j aimerai...	35.8	27.6	30.8	30.2	D
2	5945481e31aff69d35425af457c1b54b	citation drôle salle d audience mettre face no...	29.6	34.0	25.6	39.0	C
3	6e182efe093be5ba12745c2d11a7592a	laissez savoir préface contact recommande voul...	32.6	24.8	18.2	38.4	C
4	ffd581ce516fe9e2422cb643d63c7e66	boisson gratuite téléchargé l application ipho...	17.6	20.8	23.0	34.4	C
...	...	...	...	...	...	...	...
655	98ba02025b3c0b014b81a63bdfbc61df	faite okayyyy youuu pouvoir ninang haha étrang...	16.6	17.2	23.2	12.6	S
656	459e67ccc3a7873bd23f450b564b4844	effectivement engagez 3 an pouvoir mettre nive...	11.8	10.2	13.8	6.8	S
657	187ad246408231b9b1f1c481f863f4c6	regarder miroir ouai gettin argent l emballage...	8.4	16.2	8.4	19.0	C
658	c9539bdfa985a4f069ee841435a2d424	jose vien hot dogs bière pouvoir détendre fill...	7.2	12.0	12.8	9.0	S
659	4a362c777db5398e0ebf52cc8b25d5c4	prochains jour congé oui j aime l ennemi incro...	9.8	14.2	17.8	8.6	S

660 rows × 7 columns

Fig. 3. Annotated dataset

c) Model training

Before starting the model training process, the key point is feature extraction [6], which is the vector representation of texts. In this work, the TF-IDF model [9] was chosen, TF-IDF score is useful to adjust the weight between common and less frequently used words. A data augmentation method by synthetic minority oversampling, SMOTE [2], was applied to balance the dataset. In our work we have trained our dataset with supervised machine learning algorithms corresponding to the classification problem. To have the best algorithm according to several metrics, we used a certain number of classes of algorithms such as logistic regression, decision trees and gradient boosting algorithms.

Research results and their discussion

To evaluate the performance of the machine learning models, we used several machine learning metrics such as: accuracy, precision, completeness, error matrix, ROC curve, F1-score. Also, to obtain a model that correctly generalizes the results, we were keen to separate all the training and validation data sets during a time interval T (using temporal separation method). To this end, during the training phase the validation set is unknown to the classifier so that the validation set cannot accidentally infiltrate the training set, and this creates independence between the two sets. To improve the performance of some algorithms, hyperparameter optimization (maximum tree depth, learning rate) was applied [14]. In this paper, the XGBoost algorithm performed the best (Table 1) compared to other machine-learning algorithms. The most important success factors of XGBoost are its scalability in all scenarios and the ability to solve a real-scale problem using a minimum number of resources [15].

	namecode	tweets
57	7ec07d3ae0c13e13dadd77e10d3e213d	J'ai toujours pas digéré ce qu'il s'est passé ...
14	929b3052c2e260b61b65c2bb46f32241	Hésitez pas à me donnez de la force 🙏 Je sais q...
161	06bd37010539f564bfcb29e2e1901e53	Comment tu peux avoir autant de poisse et de c...
163	0a471a2a6c5e970daebfb046ab008478	Nous sommes dans le centre 😷 https://t.co/9xEE...
54	12ae902545dcb1150f25ad91f6c20fd8	Ouvrez un vrai Doner Kebab à Rennes svp je vou...

Fig. 4. Dataset part state before preprocessing

	namecode	tweets
57	7ec07d3ae0c13e13dadd77e10d3e213d	j ai toujours pas digéré ce qu il s est passé ...
14	929b3052c2e260b61b65c2bb46f32241	hésitez pas à me donnez de la force je sais qu...
161	06bd37010539f564bfcb29e2e1901e53	comment tu peux avoir autant de poisse et de c...
163	0a471a2a6c5e970daebfb046ab008478	nous sommes dans le centre lien l autre jour c...
54	12ae902545dcb1150f25ad91f6c20fd8	ouvrez un vrai doner kebab à rennes svp je vou...

Fig. 5. Dataset part state after preprocessing

Table 1

Results of XGBoost application

	Precision	Recall	f1-score	Support
C	0.71	0.55	0.62	31
D	0.69	0.61	0.65	36
I	0.73	0.86	0.79	50
S	0.65	0.73	0.69	15

In Fig. 7, it is observed that each point on the ROC curve is obtained from the values in the error matrix (Fig. 6) associated with applying a certain constraint to the classifier predictions. The ROC curve represents sensitivity as a function of specificity for all possible threshold values of the classifier under study. Classifiers that give curves closer to the top-left corner indicate a better performance. As a baseline, a random classifier is expected to give points lying along the diagonal (FPR = TPR). The closer the curve comes to the 45-degree diagonal of the ROC space, the less accurate the test. An excellent model has AUC (Area under curve) near to the 1 which means it has a good measure of separability. A poor model has an AUC near 0 which means it has the worst measure of separability. The higher the area under the curve, the better the model can perform. For example, our Class C, which represents the lowest population in our dataset has a curve close to the top left and achieve a sensitivity of 80% only if the percentage of misclassified positive examples is about 40% (Fig. 7), which is a good result for a classifier that should have practical applications.

Fig. 8 indicates that the accuracy and completeness curve of Class D shows an acceptable result. An accuracy of about 80% is required to achieve60% completeness. The accuracy and completeness score (otherwise F1-score) for Class I is 0.69. The Class S curve shows a sensitivity to predicted positives values of 50% with a true positive rate of about 60%, which is average. Class C for 50% of predicted positive values shows a rate of almost 70% true positive values. When considering all the results of models based on the accuracy metric (Fig. 9), it is stated that, the model based on naive Bayesian classifier showed the lowest accuracy (**48.48%**), and the model based on XGBoost algorithm showed the best result (**70.45%**).

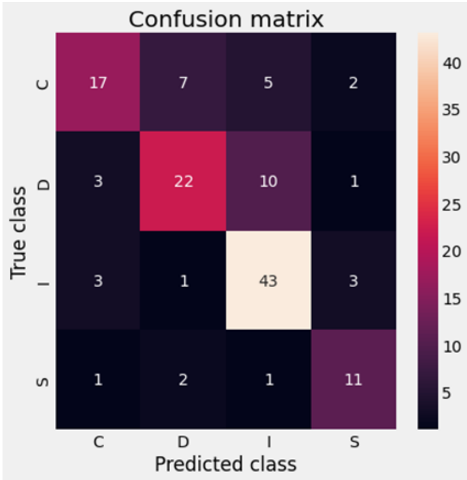

Fig. 6. XGBoost Error matrix

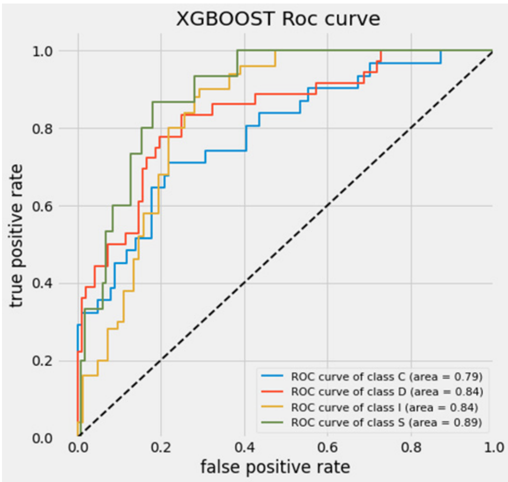

Fig. 7. XGBoost ROC curve

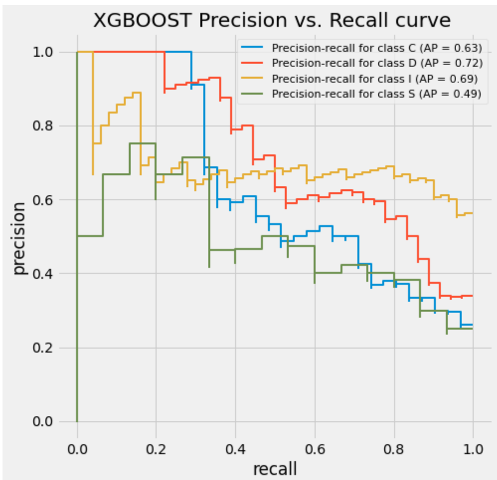

Fig. 8. XGBoost precision and completeness

	Models	Test accuracy
0	XGBoost	70.454545
1	Catboost	68.939394
2	Random Forest	63.636364
3	Logistic regression	63.636364
4	SVM	62.878788
5	SGD Classifier	62.121212
6	Decision Tree classifier	50.757576
7	Multinomial Naive Bayes	48.484848

Fig. 9. Algorithms accuracy

Conclusion

To sum it up, our work showed the feasibility of applying gradient boosting algorithms to the analyzing personality traits task using balanced small dataset. To improve the algorithms performance, hyperparameter tuning was applied to each classifier. Although the accuracy metric is not the only metric for evaluating the performance of a model, the developed model based on the XGBoost algorithm showed the best result according to the accuracy metric (**70.45%**). There is no universal threshold that we use to determine if a model has good accuracy or not. The judgement of good or bad accuracy is subjective and depends on the task in which it is measured. In our case, we obtained a score of 70.45% for a small dataset, so we can consider our model to be useful according to the accuracy metric. In addition, model accuracy between 70% and 90% is realistic and consistent with industry standards.

The following steps were taken to solve the problem:

- Dataset creation in French using the social network Twitter. The dataset was based on the DISC psychological model, which classifies personality traits into 4 categories: dominance, influence, steadiness, conscientiousness.
- Dataset annotation. The dataset was annotated by a team of psychologists on the Fiverr platform. As a result, 660 users and more than 144,000 tweets were selected. After annotating the dataset by a team of psychologists, the first resulting version of the dataset was unbalanced. Thus, the SMOTE data augmentation method was applied for the purpose of balancing the dataset.
- Data preprocessing and model training with several machine learning algorithms. In our paper, some applied pre-processing (semantic, syntactic) and features extraction methods are universal despite the chosen language. Most of the used methods in our work are designed programmatically (based on programming libraries) and support most of the spoken languages of the world.

For further research, there is a need to address the issue of using Russian language material despite the linguistic difficulties of collecting and processing. One of the possible solutions would be to add more data and use other features or extraction methods. The potential of analyzing personality traits using the XGBoost gradient boosting algorithm lies in the possibility of using it in the development of recommendation systems useful in companies, higher education institutions, for marketing, audience targeting, implementation of recruitment policies.

REFERENCES

1. **Xue D., Guo S., Gao L., Wu L.** Personality recognition on social media with label distribution learning. IEEE Access, 2017, Vol.5, pp. 13478–13488.

2. **Setiawan H., Wafi A.A.** Classification of Personality Type Based on Twitter Data Using Machine Learning Techniques. 2020 3rd International Conference on Information and Communications Technology (ICOIACT), 2020, pp. 94–98.

3. **Goldberg L.R.** An Alternative "Description of Personality": The Big-Five Factor Structure. Journal of Personality and Social Psychology, 1990, Vol. 59, no. 6, pp. 1216–1229. DOI: https://doi.org/10.1037/0022-3514.59.6.1216

4. **Hernández Y., Martínez A., Estrada H., Ortiz J., Acevedo C.** Machine Learning Approach for Personality Recognition in Spanish Texts. Applied Sciences. 2022, Vol. 12, no. 6, pp. 1–17. DOI: https://doi.org/10.3390/app12062985

5. **Dwi Hartanto A., Ema Utami, Sumarni Adi, Suwanto Raharjo.** Classifying User Personality Based on Media Social Posts Using Support Vector Machine Algorithm Based on DISC Approach. 2020 2nd International Conference on Cybernetics and Intelligent System (ICORIS), Manado, Indonesia, 2020, pp. 1–4.

6. **Bharadwaj S., Sridhar S., Choudhary R., Srinath R.** "Persona Traits Identification based on Myers-Briggs Type Indicator (MBTI) – A Text Classification Approach". International Conference on Advances in Computing, Communications and Informatics (ICACCI), Bangalore, India. 2018, pp. 1076–1082. DOI: 10.1109/ICACCI.2018.8554828

7. **Tarekegn A.N., Giacobini M., Michalak K.** A review of methods for imbalanced multi-label classification. Pattern Recognition. 2021. Vol. 118. DOI: https://doi.org/10.1016/j.patcog.2021.107965

8. **Chigova E.A., Plyushch I.V., Leskova I.V.** Organization of structured interaction on the base of psychographic characteristics within the model of personality traits DISC. IOP Conference Series Materials Science and Engineering, 2019, Vol. 483, no. 1, pp. 1–6.

9. **Karami A., Morgan Lundy, Frank Webb.** Twitter and Research: A Systematic Literature Review through Text Mining. IEEE Access, 2020, Vol. 8, pp. 67698–67717.

10. **Yang D., Lee W.S.** Disambiguating Music Emotion Using Software Agents. Proceedings of 5th International Conference on Music Information Retrieval, 2004, pp. 1–6.

11. **Goldberg Y.** Neural Network Methods for Natural Language Processing. Synthesis Lectures on Human Language Technologies, 2017, Vol. 37, no. 1, 287 p.

12. **Qaiser S., Ali R.** Text Mining: Use of TF-IDF to Examine the Relevance of Words to Documents. International Journal of Computer Applications, 2018, Vol. 181, no. 1, pp. 1–5. DOI : https://doi.org/10.5120/ijca2018917395

13. **Chawla Nitesh V., Kevin W. Bowyer, Lawrence O. Hall, Philip W.** Kegelmeyer. SMOTE: Synthetic minority over-sampling technique. Journal of Artificial Intelligence Research, 2002, Vol. 16. Pp. 321–357. DOI: https://doi.org/10.1613/jair.953

14. **Agrawal T.** Hyperparameter Optimization in Machine Learning. Apress Berkeley, 2021, 166 p. DOI: https://doi.org/10.1007/978-1-4842-6579-6

15. **Chen T., Guestrin C.** XGBoost: A scalable tree boosting system. In Proceedings of the 22nd ACM SIGKDD International Conference on Knowledge Discovery and Data Mining, 2016, pp. 785–794. DOI: https://doi.org/10.1145/2939672.2939785

16. **Kluemper D.H., Rosen P.A.** Future employment selection methods: Evaluating social networking web sites. Journal of Managerial Psychology, 2009, Vol. 24, no. 6, pp. 567–580.

INFORMATION ABOUT AUTHORS / СВЕДЕНИЯ ОБ АВТОРАХ

Mbele Ossiyi Luc Prucell
Мбеле Оссийи Люк Прюсель
E-mail: lucprucell@gmail.com

Drobintsev Pavel D.
Дробинцев Павел Дмитриевич
E-mail: drobintsev_pd@spbstu.ru

Submitted: 04.07.2023; Approved: 21.09.2023; Accepted: 11.10.2023.
Поступила: 04.07.2023; Одобрена: 21.09.2023; Принята: 11.10.2023.

Research article
DOI: https://doi.org/10.18721/JCSTCS.16306
UDC 621.311.6

DESIGN AND CONTROL OF A FAST CHARGING MODULE BASED ON THE USB-PD PROTOCOL

Yu.N. Kozhubaev[1] ✉ , *E.N. Ovchinnikova*[1], *M.A. Gorelik*[1], *Y. Yiming*[2]

[1] Saint-Petersburg Mining University, St. Petersburg, Russian Federation;
[2] Peter the Great St. Petersburg Polytechnic University, St. Petersburg, Russian Federation

✉ y.n.kozhubaev@gmail.com

Abstract. The main purpose of this article is to develop and design a USB_PD fast charging circuit based on the Type_C interface, to increase the battery life of electronic devices, provide an optimal power mode (minimum interface supply voltage of 5V while increasing the charging current). In this article, LDOs (Low Voltage Linear Regulator) are selected to implement an FPGA buck power supply, which is a fixed output regulator that provides low voltage output with current limiting, thermal shutdown, and battery reversal protection. To achieve this goal, the problems of high power consumption and low battery life caused by the rapid development of mobile devices such as mobile phones are analyzed, and it is indicated that the most effective solution at present is to increase the charging efficiency. The article briefly talks about the current state of fast charging research. The general structure of the USB PD fast charging protocol, the structure and functions of each part are analyzed. The physical layer simulation of the USB PD controller is completed using Verilog HDL, the function and implementation principle of each module is detailed, and the VCS is used for simulation to ensure that the design function is correct. The above-described board-level design is tested based on a programmable logic integrated circuit, and a logic analyzer and a protocol analyzer are used on the test results to achieve the expected design goals.

Keywords: fast charging module, USB-PD protocol, interface, Type_C, power transmission protocol

Citation: Kozhubaev Y.N., Ovchinnikova E.N., Gorelik M.A., Yiming Y. Design and control of a fast charging module based on the USB-PD protocol. Computing, Telecommunications and Control, 2023, Vol. 16, No. 3, Pp. 64–73. DOI: 10.18721/JCSTCS.16306

Научная статья
DOI: https://doi.org/10.18721/JCSTCS.16306
УДК 621.311.6

ПРОЕКТИРОВАНИЕ И УПРАВЛЕНИЕ МОДУЛЕМ БЫСТРОЙ ЗАРЯДКИ НА ОСНОВЕ ПРОТОКОЛА USB-PD

Ю.Н. Кожубаев[1] ✉ , *Е.Н. Овчинникова*[1], *М.А. Горелик*[1], *Я. Имин*[2]

[1] Санкт-Петербургский горный университет, Санкт-Петербург, Российская Федерация;

[2] Санкт-Петербургский политехнический университет Петра Великого, Санкт-Петербург, Российская Федерация

✉ y.n.kozhubaev@gmail.com

Аннотация. Основная цель в данной статье заключается в разработке и проектировании схемы быстрой зарядки USB_PD на основе интерфейса Type_C, для увеличения времени автономной работы электронных устройств, обеспечение оптимального режима питания (минимальном напряжении питания интерфейса 5 В при увеличении зарядного тока). В данной статье выбраны LDO (Low Voltage Linear Regulator) для реализации понижающего источника питания FPGA, который представляет собой стабилизатор с фиксированным выходом, который обеспечивает низкое напряжение, на выходе с ограничением по току, отключением при перегреве и защитой от переполюсовки батареи. Для реализации поставленной цели проанализированы проблемы высокого энергопотребления и низкого времени автономной работы, вызванные быстрым развитием мобильных устройств, таких как мобильные телефоны, и указано, что наиболее эффективным решением в настоящее время является повышение эффективности зарядки. В статье кратко рассказывается о текущем состоянии исследований быстрой зарядки. Проанализирована общая структура протокола быстрой зарядки USB PD, структура и функции каждой части. Моделирование физического уровня USB-контроллера PD завершено с использованием Verilog HDL, функция и принцип реализации каждого модуля подробно представлены, а VCS используется для моделирования, чтобы гарантировать правильность проектной функции. Выполняется проверка вышеописанной конструкции на уровне платы на основе программируемой логической интегральной схемы, а также используются логический анализатор и анализатор протоколов для анализа результатов проверки для достижения ожидаемых целей проектирования.

Ключевые слова: модуль быстрой зарядки, протокола USB-PD, интерфейс, Type_C, протокол передачи энергии

Для цитирования: Kozhubaev Y.N., Ovchinnikova E.N., Gorelik M.A., Yiming Y. Design and control of a fast charging module based on the USB-PD protocol // Computing, Telecommunications and Control. 2023. Т. 16, № 3. С. 64–73. DOI: 10.18721/JCSTCS.16306

Introduction

With the continuous digitization, the needs of applications in the field of data interaction and power transmission have further expanded. Whether it is stationary devices such as desktop computers, TVs, workstations, or portable devices such as mobile phones and tablet computers, the USB interface is undoubtedly the most direct link between data transmission and electricity [1–3]. Modern equipment not only imposes explicit requirements for increasing the data transfer rate, but also puts forward additional requirements for the throughput of the USB interface [4–6]. The ability to transfer 100W of power has become the goal that the USB 3.1 interface specification hopes to achieve, and only USB TYPE-C interface can support the transfer of this power. This requirement cannot be met according to the traditional USB

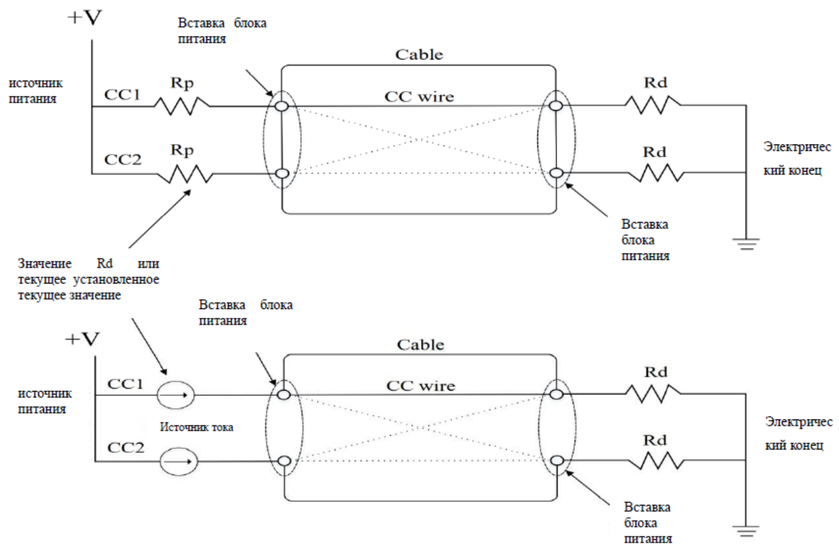

Fig. 1. Schematic diagram of intrusion detection

3.0 interface protocol specifications and below, and it is necessary to promote and apply the USB 3.1 protocol specification, which can support high power and high-speed data transmission [7–8].

With the popularization of smart devices, the performance of smartphones has become higher and higher, with more and more functions, and the hardware has improved greatly. At present, lithium batteries are mainly used in power supplies for portable electronic devices. The problem of poor device endurance is usually solved by increasing the capacity of lithium batteries. However, this method increases the weight of the device. Before lithium battery technology makes a major breakthrough, increasing its charging speed is another way to solve this problem. The fast-charging protocol is based on a certain battery capacity, reduces the charging time by increasing the charging power, and the way to increase the charging power is to start from the charging voltage and charging current. Usually there are three ways: increase the charging current while the charging voltage is unchanged, and the charging current is unchanged. At the same time, the charging voltage increases, and the charging voltage and current increase simultaneously [9–11].

Research status and development trends

The USB interface (Fig. 1) is divided into USB Type A, USB Type B, USB Type C, Mini USB, and Micro USB interfaces. The Type-C interface provides a smaller, thinner, and more durable interface instead of the traditional physical interface. Several significant advantages of the Type-C interface: The thickness of the Type-C interface is only 2.4mm, which can be used in ultra-high. In some thin devices, the Type-C interface is symmetrical, supporting the positive and negative insertion of the plug, at the same time, it also supports the positive and negative insertion of the cable direction [12–14].

The USB_PD protocol can provide a maximum power of 20V/5A for charging. Traditional USB Type_A and USB Type B interfaces cannot transmit such high power. USB_IF organization formulated USB Type_C. The interface specification stipulates that a standard data line equipped with Type_C interface can transmit a maximum current of 5A, in order to cooperate with the USB_PD fast charging protocol to achieve maximum power transfer; USB Type_C The interface is compatible with the functions of the previous generation interface, and its transfer rate can also reach 40Gbps. And there is a very convenient advantage that there is no need to distinguish the direction of the interface [15–17]. Now there are more and other devices equipped with USB Type_C interface, and interface unification is a trend, because the 100W USB_PD fast charging protocol transmission power can match the charging power of most electronic products. Requirements and characteristics do not need to distinguish between the direction of the interface, widely used in consumer electronics such as smart phones and thin and light laptops, and will be popularized in more portable electronic devices. In the future, USB PD may use the same charger and charging cable when charging different devices, which is useful to reduce resource wastage caused by different devices having to be equipped with different chargers [18–20].

Development of the USB_PD protocol based on the Type_C interface

When the charger is charging the electric appliance, only after the charger and the electric appliance are connected stably, safe and fast charging can be done, so the insertion detection work should be the first step. As mentioned above, setting up the power supply in this design is done by connecting the CC line between the two devices. Initially, the USB Type-C VBUS interface has no power, and the system needs to connect a cable between the two devices. The role of the device is determined at connection time. A device whose CC line on a socket is pulled high is defined as a power supply terminal, and a device that goes low is defined as a power terminal.

Figure 1 shows a method for determining the role of power supply and demand, cable orientation, and current supply capability. Source terminals CC1 and CC2 are driven high through resistor Rp, and detected CC1 or CC2 is always high when nothing is connected. After connecting the power terminal, the voltage of CC1 or CC2 is reduced by the resistor Rd. Since there is only one CC wire in the cable, the source can tell which CC is low. The voltage CC1 or CC2 of the consumer is also determined. Once the CC line is detected to be high voltage, its voltage level will allow the consumer to know the current capacity of the power supply. The pull-up resistor Rp in the circuit can also be replaced by a current source that is easily implemented in an integrated circuit and can be immune to V+ supply voltage error.

It can be seen from the principles above that the CC line at the source end will cause voltage variations before and after switching on. In this design, two op-amp comparators op1 and op2 are used to compare the voltage changes before and after CC1 and CC2, respectively, and then according to the output signals op1out and op2out of the two op-amps, it is determined whether CC1 and CC2 are inserted [21–23].

Simulation based on programmable logic integrated circuits (FPGA)

Test plan

To make sure that the USB PD controller can work properly, you need to check the design goals with the following aspects in mind. Check if the discovery plug-in works normally and can start communicating with the PD normally after detecting the connection of the device. Whether the hardware circuit performs data processing in transmitted data packets as intended. Whether the source side and the receiver side can normally send and receive data, can they correctly analyze the received data and give appropriate feedback. The test setup in this article is to use the Alter Cyclon IV EP4CE6E22CN Development Board and the USB PD Protocol Tester (POWER-Z) as the test platform. The emulator simulates a charging terminal, and the USB PD protocol tester simulates a power consumption terminal (set to monitor mode). After the system is powered on, when the emulator detects that a device is inserted, it starts sending its own capability power supply to the tester. To facilitate observation, a logic analyzer is used to capture the waveform on the CC line, a PD protocol analyzer is used to analyze the waveform, and an oscilloscope is used to observe the voltage on the CC line during the power matching process [24–26].

If, after the test, the source terminal and the sink terminal exchange information, it means that the function of the input detection module is correct and communication with the PD starts normally. Then, by analyzing the waveform captured by the logic analyzer, when the 4b5b encoding, BMC encoding, and crc32 calculation of the transmitted data are fully realized, it indicates that the hardware circuit is working correctly. Compare the communication results output by the protocol analyzer with the overall power matching process specified in the protocol. If they match, it means that the PD communication can complete the negotiation as expected. Finally, observe the voltage on the CC line through the oscilloscope When the voltage is 1V, indicates that the operating voltage of the CC line is normal.

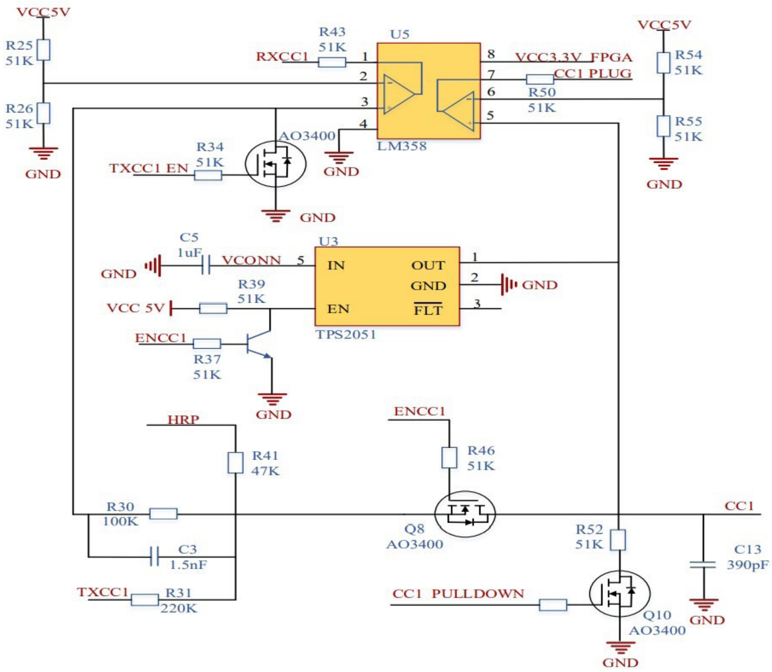

Fig. 2. CC1 Insert Detection Circuit

Construction of the test platform

The IC model chosen in this article, Alter Cyclon IV EP4CE6E22C8N, has the following features: low-cost, low-power FPGA architecture with 22320 logical cells, up to 6.3 MB of internal memory, with 80 configurable I/Os, has 4 PLLs. In this design, a stable power supply to the FPGA is achieved by choosing a model with a fixed output voltage of 3.3V [27–29].

Figure 2 shows the cable entry detection circuit in CC1. When the cable does not enter or exit, the voltage of CC1 is always at a high level. When the end of the power supply is connected, the voltage of CC1 will be pulled down, as shown in figure CC1 PULLDOWN. According to the above principle, it is only necessary to detect the voltage drop across CC1 to conclude that the cable is inserted and CC1 is valid.

The LM358 shown in the figure is a dual op-amp. Inside are two independent high-gain operational amplifiers with internal frequency compensation. [30–32]. It can effectively meet two different requirements of single power supply and dual power supply. When operating with this function, the power supply current is not affected by other factors. Voltage change detection on CC1 can be realized with LM358. When it is determined that the CC1 cable is inserted, the controller starts sending data packets to the consumer via CC1 to communicate with the PD. CC2 has the same insertion detection scheme as CC1 [33–35].

In this model, we use quartus II to write the RTL code to the FPGA. Fig. 3 shows that the RTL code was written successfully. Use the keil software to program the C code into a hex file and write it to the emulator to get an FPGA emulator that meets the test requirements, and connect the emulator to the USB PD protocol tester, logic analyzer and other equipment. construction of a verification platform. As shown in Fig. 4.

Simulation results

Using a PD protocol analyzer, the waveform represented by the logic analyzer can be analyzed fully automatically. Fig. 5 shows the entire power negotiation process resulting from the analysis of the PD protocol analyzer. After the Source is connected to the Sink, power matching occurs first via

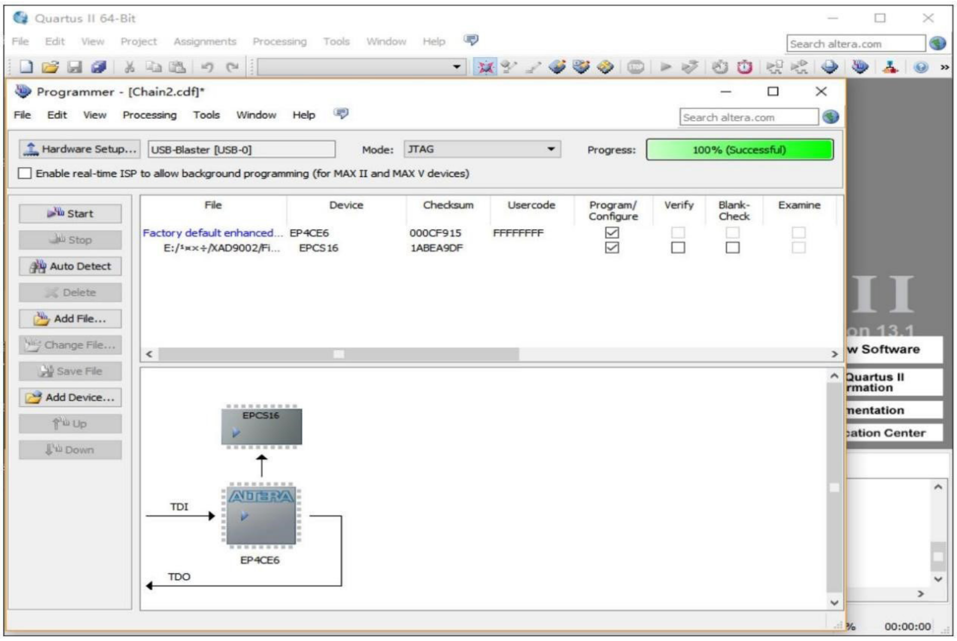

Fig. 3. Programming procedure for quartus II

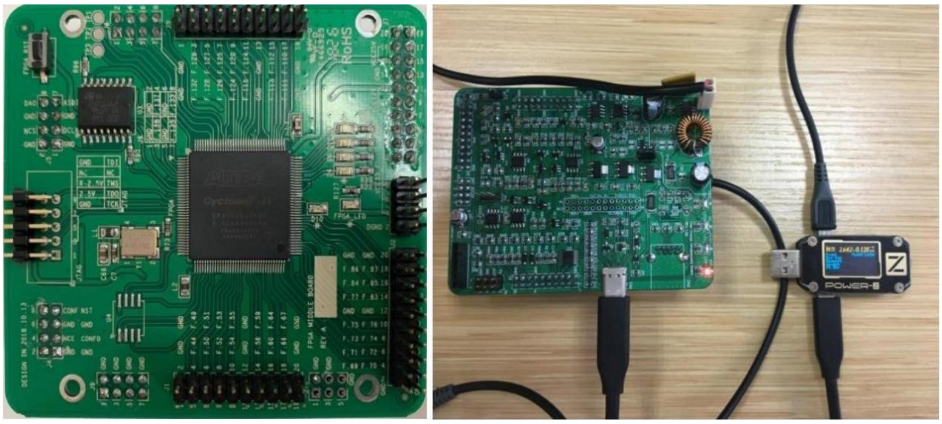

Fig. 4. FPGA Verification Platform

the CC line. Sou sends Source Cap data packets to Sink five times in a row. This data packet contains five power supply parameter specifications, namely: 5V/3.03A, 9V/2.39A, 12V/2.31A, 15V/1.91A, 20V/1.83A. After successfully receiving the Source limitation, the SINK side first returns GoodCRC data, and then parse the Source constraint and send the Reqest 5V/3.03A packet to the Source side, and then complete the whole process according to the communication steps of PD power negotiation. According to the above results, the PD controller can realize the expected power supply through power matching.

A fragment of the values and steps of the energy matching information is shown in Table 1.

Conclusion

The main work of this article is to simulate a charge controller that supports USB PD fast charging technology over the USB PD protocol to solve the battery life problem of electronic devices.

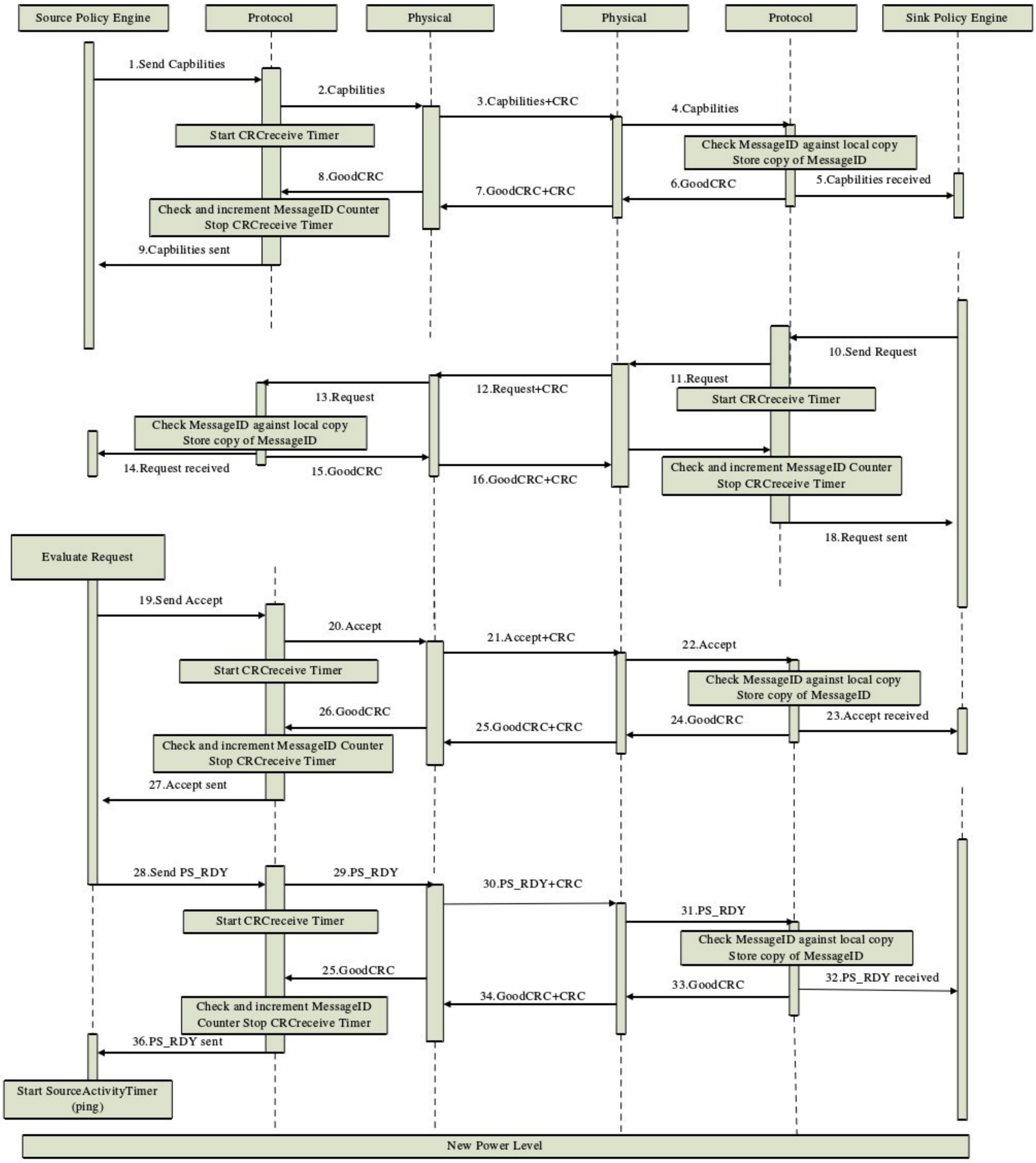

Fig. 5. Power Supply Matching Block Diagram

The general structure of the USB PD fast charging protocol is presented through the USB PD structure block diagram and the power negotiation process flow diagram, as well as the Device Policy Manager. The Verilog language is used to complete the protocol layer detection design, and to implement the functions of communication data packet configuration, data packet inspection, data packet analysis, and data packet information processing. The circuits on the FPGA development board and the design of the verification platform are examined, and the USB PD logic analyzer and USB PD protocol analyzer are used to analyze the test results to ensure that the design code follows the design and achieves the expected function. The test results show that the developed controller implements power matching during fast charging.

Table 1

Fragment of values and stages of energy matching information

Step	Source Port	Sink Port
1	The Policy Engine notifies the protocol layer to send Capabilities packets	
2	The protocol layer forwards Capability packets to the physical layer. CRCReceiverTimer start time	
3	The physical layer adds crc32 to Capbilities and sends	The physical layer receives the packet and completes the crc32 check.
4		Capabilities packets are passed from the physical layer to the protocol layer.
5		The Capability packet is passed from the physical layer to the protocol layer, which compares the ID in the received packet with the previous one and writes the new ID. The protocol layer notifies the Policy Engine that a packet has been received. The Policy Engine starts the PSTransitionTimer and reduces the current. Policy Engine Starts Power Supply Transformation.
6		The protocol layer passes the GoodCRC packet to the physical layer.
7	The physical layer receives the packet and completes the crc32 check.	The physical layer adds crc32 to the GoodCRC message and
8	The physical layer passes the verified GoodCRC packet to the protocol layer, and then the protocol layer checks and updates the MessageIDCounter.	
9	The protocol layer notifies the Policy Engine Capabilities message that the message was successfully sent.	

As a result of the simulation of the operation of the PD USB controller based on a field-programmable logic integrated circuit, the optimal power mode (5V/3.03A) is realized from the 5 provided (5V/3.03A, 9V/2.39A, 12V/2.31A, 15V/1.91A, 20V/1.83A) power parameters. According to the results in the article, the PD controller can realize the expected power delivery through power matching.

REFERENCES

1. **Zhang Song, Li Yun.** FPGA Modular Design Method [J]. Journal of Electronic Measurement and Instrumentation, 28 (05) (2014) 560–565. DOI: 10.13382/j.jemi.2014.05.015

2. **Shklyarskiy Y.E., Batueva D.E.** Operation mode selection algorithm development of a wind-diesel power plant supply complex. Journal of Mining Institute, 253 (2022). DOI: 10.31897/PMI.2022.7

3. **Abramovich B.N., Bogdanov I.A.** Improving the efficiency of autonomous electrical complexes of oil and gas enterprises, Journal of Mining Institute, 249 (2021). DOI: 10.31897/PMI.2021.3.10

4. **Zhang Shiwei, Yin Shiping, He Yuntao.** FPGA control and implementation of USB2.0 interface transmission [J]. Foreign Electronic Measurement Technology, 28 (11) (2009) 74–76+80. DOI: 10.19652/j.cnki.femt.2009.11.019

5. **Li Shenghui.** Design and implementation of USB_PD protocol based on Type_C interface [D]. Xidian University, 2017.

6. **Safiullin R.N., Afanasyev A.S., Reznichenko V.V.** The Concept of Development of Monitoring Systems and Management of Intelligent Technical Complexes, Journal of Mining Institute, 237 (2019). DOI: 10.31897/pmi.2019.3.322

7. **Senchilo N.D., Ustinov D.A.** Method for Determining the Optimal Capacity of Energy Storage Systems with a Long-Term Forecast of Power Consumption. Energies, 14 (2021) DOI: 10.3390/en14217098

8. **Nurgalieva K.S., Abdullah K.A., Seyed M.A., Slavko N., John William G.G.** Application of Neural Network and Time-Domain Feature Extraction Techniques for Determining Volumetric Percentages and the Type of Two Phase Flow Regimes Independent of Scale Layer Thickness Applied Sciences. 12 (2022) 1–13.

9. **Ruan Yi, Song Qingliang, Wang Jia, Zhang Bingbing.** Overview and application of USB Type-C and PD technology [J]. Integrated Circuit Applications, 34 (04) (2017) 31–36. DOI: 10.19339/j .issn.1674-2583.2017.04.007

10. **Yu Dejun.** Research on high-power intelligent power supply technology based on USB TYPE-C protocol [D]. University of Electronic Science and Technology, 2018.

11. **Beloglazov I., Krylov K.** An Interval-Simplex Approach to Determine Technological Parameters from Experimental Data. Mathematics, 10 (2022). DOI: 10.3390/math101

12. **Xu Chunying, Zhao Xiaoxin, Xia Lijiao, Zhang Hongli.** Analysis of fast charging protocol and construction of test platform [J]. Modern Telecommunications Technology, 47 (05) (2017) 41–49.

13. **Brilliant L.S., Zavialov A.S., Danko M.U., Andronov K.A., Shpurov I.V., Bratkova V.G., Davydov A.V.** Integration of machine learning methods and geological and hydrodynamic modeling in field development design.Neftyanoe Khozyaystvo – Oil Industry, 3 (2022) 48–53. DOI: 10.24887/0028-2448-2022-3-48-53

14. **Wei Yongxiang, Wang Yan.** USB_PD protocol fast charging mobile power design [J]. Journal of South China University (Natural Science Edition), 33 (06) (2019) 84–90. DOI: 10.19431/j.cnki.1673-0062.2019 .06.015

15. **Safiullin R.N., Afanasyev A.S., Reznichenko V.V.** The Concept of Development of Monitoring Systems and Management of Intelligent Technical Complexes, Journal of Mining Institute, 237 (2019). DOI: 10.31897/pmi.2019.3.322

16. **Li Yong.** Emerging applications of USB PD in fast charging of mobile devices [J]. Electronic Products World, 25 (09) (2018) 27–30.

17. **Zhang Yi.** Research and design of fast charging controller based on USB PD protocol [D]. Xidian University, 2019. DOI: 10.27389/d.cnki.gxadu.2019.002455

18. **Brigadnov I., Lutonin A., Bogdanova K.** Error State Extended Kalman Filter Localization for Underground Mining Environments.Symmetry, 15 (2023). DOI: 10.3390/sym15020344

19. **Fang Kanfei.** Design and verification of fast charging control system based on USB PD protocol [D]. Anhui University, 2020. DOI: 10.26917/d.cnki.ganhu.2020.000621

20. **Sychev Y.A., Zimin R.Y.** Improving the quality of electricity in the power supply systems of the mineral resource complex with hybrid filter-compensating devices. Journal of Mining Institute, 247 (2021). DOI: 10.31897/PMI.2021.1.14

21. **Liu Zhongkun, Li Yeli, Lu Likun.** Design and Implementation of 4B/5B Coding Based on Oversampling CDR [J]. Computer Applications and Software, 32(10) (2015) 227–230.

22. **Shklyarskiy Y.E., Batueva D.E.** Operation mode selection algorithm development of a wind-diesel power plant supply complex. Journal of Mining Institute, 253 (2022). DOI: 10.31897/PMI.2022.7

23. **Fang Kanfei, Lin Zhiting, Zhao Jianzhong, Li Zhi, Bi Liqiang.** Design of new BMC decoding circuit for USB PD3.0 protocol [J]. Computer Engineering and Applications, 57 (01) (2021) 77–83.

24. **Guo Xiugen.** Talking about the evolution and future development trend of mobile phone chargers [J]. Electronics World, 19 (2018) 110–113. DOI: 10.19353/j.cnki.dzsj.2018.19.063

25. **Sultanbekov R.R., Beloglazov I.I., Islamov S.R., Ong M.C.** Exploring of the Incompatibility of Marine Residual Fuel: A Case Study Using Machine Learning Methods, Energies, 14 (8422) (2021) 1–16.

26. **Niu Yumeng, Jiao Jiye, Li Chen.** Design and implementation of FPGA-based USB PD controller [J]. Computer and Digital Engineering, 48 (05) (2020) 1238–1242.

27. **Zhang Wanrong, Wang Feihu.** Design and verification of new PD protocol chip BMC decoding circuit [J]. Electronic Technology Application, 47 (11) (2021) 29–32+38. DOI: 10.16157/j.issn.0258-7998.211493

28. **Abramovich B.N., Bogdanov I.A.** Improving the efficiency of autonomous electrical complexes of oil and gas enterprises, Journal of Mining Institute, 249 (2021). DOI: 10.31897/PMI.2021.3.10

29. **Zhu Chaocheng.** USB_PD protocol physical layer design based on TYPE_C [D]. Southeast University, 2021. DOI: 10.27014/d.cnki.gdnau.2021.003221

30. **Xue Shaojun, Wu Songlin.** PLC-based design of lifting and traversing three-dimensional garage, Electronic Production. Ser.1, 6 (2016) 13–14.

31. **Gao Jing.** Research on the hardware design of PLC-based electrical control system for threedimensional garage, Invention and Innovation (Vocational Education). 2 (2020) 146–147.

32. **Yang Shao Yang.** Application of PLC in electrical automation control, Science and technology innovation. Ser. 2, 1 (2021) 175–176.

33. **Wang Huayi.** Design of intelligent control system for three-dimensional parking garage, North China University of Technology, 8 (2019) 15.

34. **Wang Xiaonong.** Research on optimization of three-stage parking space allocation strategy for planar mobile stereo garage, Lanzhou Jiaotong University, 5 (2019) 98–100.

35. **Wu P., Pan X.L., Xu G.Y.** Research on the testing technology of relay control circuits based on digital circuit model, Ship Electric Technology. Ser.30, 4 (2010) 20–23+33.

INFORMATION ABOUT AUTHORS / СВЕДЕНИЯ ОБ АВТОРАХ

Yuriy N. Kozhubaev
Кожубаев Юрий Нургалиевич
E-mail: y.n.kozhubaev@gmail.com

Elena N. Ovchinnikova
Овчинникова Елена Николаевна

Maria A. Gorelik
Горелик Мария Александровна

Yiming Yao
Имин Яо

Submitted: 15.06.2023; Approved: 31.07.2023; Accepted: 11.10.2023.
Поступила: 15.06.2023; Одобрена: 31.07.2023; Принята: 11.10.2023.